ASSEMBLY OF MICROGEL BUILDING BLOCKS INTO CELL-INSTRUCTIVE MICROPOROUS ANNEALED PARTICLE HYDROGELS FOR TISSUE ENGINEERING

A Dissertation

by

SHANGJING XIN

Submitted to the Office of Graduate and Professional Studies of
Texas A&M University
in partial fulfillment of the requirements for the degree of

DOCTOR OF PHILOSOPHY

Chair of Committee,	Daniel Alge
Committee Members,	Carl Gregory
	Melissa Grunlan
	Roland Kaunas
Head of Department,	Mike McShane

December 2019

Major Subject: Biomedical Engineering

ABSTRACT

Therapeutic cell delivery is a major strategy to stimulate the repair in tissue engineering and regenerative medicine. Efficacious cell therapies require a biomaterial carrier to retain injected cells in degenerated sites and guide cell function. Hydrogels, consisting of water-swollen polymeric network, are particularly of interest as cell delivery vehicles due to their structural similarity to native extracellular matrix. The common approach is to inject hydrogel precursor solutions with cells and cured *in situ* for encapsulation, which myriad evidences have suggested to improve the cell retention and viability. However, the resulting polymeric network are nanoporous, which form physical constrains for cell behaviors. Microporous annealed particle (MAP) hydrogels are an emerging class of biomaterials to overcome this challenge by providing permissive environment to cells. The overall goal of this work was to develop cell-instructive MAP hydrogels as a therapeutic cell delivery platform to improve regeneration outcomes.

Norbornene-bearing poly(ethylene glycol) microgels were assembled into MAP hydrogels via thiol-ene click chemistry with the addition of bis-thiol linker and human mesenchymal stem cells were incorporated during microgel assembly. Since cells interact with microgel surface within MAP hydrogels, we demonstrated the possibility of leveraging the rich body of knowledge regarding cell behavior in 2D environments to direct cellular behavior within these 3D scaffolds. We revealed cells responded to stiffness by activating mechanosensing pathways. In addition, long-term cell spreading, proliferation, and microenvironmental remodeling were dependent critically on the susceptibility of the MAP hydrogels to degradation. The paracrine secretion of cells was influenced by both signaling from specific integrin-binding peptides and degradability of the MAP hydrogels. The healing outcomes of an optimized formulation was evaluated in a mouse femoral defect model, and significant new bone formation was seen using these MAP hydrogels. We further developed a novel microfluidic method to create physicochemical gradients in MAP hydrogels for screening cell-material interactions. Last, we showed the use of microgels as biomaterial inks to construct MAP hydrogels with anatomically relevant structures in 3D printing.

DEDICATION

I would like to dedicate this dissertation work to my Mom and Dad, and my fiancée, Lingli.

ACKNOWLEDGEMENTS

First, I would like to thank my family for their love and support. Mom and Dad, I owe you forever. I have been away from home for ten years to pursue my education, including six years in another country with a 12-hour time difference. You support me on achieving my dream, regardless of the fact that I cannot accompany you very often during the time. Indeed, throughout my life, you have done everything you can to enable my success. Lingli, I am fortunate to meet you in the middle of the Ph.D. journey. I cannot imagine how to come through those tough times without you. Thank you for supporting me to continue to pursue my ambitions. I want to let you know that you are the reason why this long distance can work out for us. I look forward to our future together.

Next, I would like to thank my advisor, Dr. Daniel Alge, who has helped me to build up my research projects and taught me so much about how to do science. Danny, thank you for letting me work on an area that I am really interested in. The knowledge and skills I learned from you would be the most valuable things in my future career. I also want to thank my committee members, Dr. Carl Gregory, Dr. Melissa Grunlan, and Dr. Roland Kaunas, for their guidance and support throughout the course of this research. In addition, it will also be impossible for me to accomplish this work without my master's and undergraduate research experience. I would like to thank my master advisor, Dr. Christine Schmidt of the Department of Biomedical Engineering at the University of Florida, and my two great postdoc mentors in Schmidt Lab, Dr. Zin

Khaing and Dr. Rebecca Wachs. I am particularly grateful for the great opportunity to work in the lab and their guidance during the time. I also want to acknowledge my undergraduate mentor, Dr. Hongbing Deng of Wuhan University in China, who brought me into the world of biomaterials and inspired my interest in this area.

I would also like to acknowledge the collaborators and undergraduate students that contributed to this dissertation work. The undergraduate student I mentored, Jay Garza of the Department of Biomedical Engineering, partially contributed to the production and characterization of microgels. Professor Arum Han and Dr. Jing Dai of the Department of Electrical and Computer Engineering prepared the microgel gradient arrays from microfluidics. Professor Akhilesh Gaharwar and David Chimene of the Department of Biomedical Engineering contributed to the 3D printing work. Professor Carl Gregory of the Department of Molecular and Cellular Medicine provided and trained on the mouse femoral defect model. I also thank the funding source from the National Institutes of Health and Texas A&M Engineering Experiment Station to make this research possible.

Finally, I would like to give a special thanks to my high school sweetheart, Yang Cao. CY, you really motivated me to work harder and finish this dissertation work quicker in summer 2017, which was definitely a turning point in my Ph.D. journey. Almost all the data presented in this dissertation were collected after it. I know you are the most important reason why I can accomplish Ph.D. degree now.

CONTRIBUTORS AND FUNDING SOURCES

Contributors

This work was supervised by a dissertation committee consisting of Professors Daniel Alge (advisor), Melissa Grunlan, and Roland Kaunas of the Department of Biomedical Engineering and Professor Carl Gregory of the Department of Molecular and Cellular Medicine.

The electrospraying apparatus for Chapter II was established by Omar Wyman of the Department of Biomedical Engineering. The characterization of electrosprayed microgels in Chapters III and V was partially conducted by Jay Garza of the Department of Biomedical Engineering. The microgel arrays from microfluidics in Chapter IV were produced by Dr. Jing Dai of the Department of Electrical and Computer Engineering under the supervision of Professor Arum Han. The 3D printing work in Chapter V was conducted by David Chimene of the Department of Biomedical Engineering under the supervision of Professor Akhilesh Gaharwar. The *in vivo* mouse femoral defect model was provided by Professor Carl Gregory of the Department of Molecular and Cellular Medicine.

All other work conducted for the dissertation was completed by the student independently.

Funding Sources

Graduate study was supported by Graduate Teaching Fellowship and Graduate Research Assistantship from Texas A&M University.

This work was also made possible in part by the National Institute of Arthritis and Musculoskeletal and Skin Diseases of the National Institutes of Health under Grant Number R21 AR071625 and Texas A&M Engineering Experiment Station start-up funds. Its contents are solely the responsibility of the authors and do not necessarily represent the official views of the National Institutes of Health.

NOMENCLATURE

2D	two dimension
3D	three dimension
BMP-2	bone morphogenetic protein 2
c(RRETAWA)	cyclized arginine-arginine-glutamic acid-tyrosine-alanine-tryptophan-alanine
DAPI	4',6-diamidino-2-phenylindole
ESEM	environmental scanning electron microscope
FITC	fluorescein isothiocyanate
hMSC	human mesenchymal stem cell
LAP	lithium phenyl-2,4,6-trimethylbenzoylphosphinate
MAP	microporous annealed particle
MMP	matrix metalloproteinases
Micro-CT	micro computed tomography
NMR	nuclear magnetic resonance
OPG	osteoprotegerin
PEG	poly(ethylene glycol)
PEG-DT	PEG-dithiol
PEG-Nb	PEG-norbornene
RGD	arginine–glycine–aspartic acid
VEGF	vascular endothelial growth factor
YAP	yes-associated protein

TABLE OF CONTENTS

LIST OF FIGURES

LIST OF TABLES

Page

CHAPTER I

INTRODUCTION

Literature Review

Hydrogels for Therapeutic Cell Delivery

Hydrogels are a class of biomaterials that have wide uses in biomedical field because of their structural similarity with native tissues.[1] These materials consist of water-swollen polymeric networks, which often absorb many times their dry weight in water depending on their hydrophilicity. The polymeric networks have sufficient crosslinks to prevent dissolving in the short term and are able to permeate nutrients and metabolites. The mechanical properties of hydrogels can also be engineered to fit within the ranges of many soft tissues. Wichterle *et al.* reported the first hydrogel in 1960 by crosslinking poly(hydroxyethyl methacrylate) with ethylene glycol dimethyl acrylate and emphasized the biocompatibility of hydrogels as they mimic salient elements of native tissues.[2] In 1980, Lim *et al.* demonstrated the first example of cell encapsulation in hydrogels. Islets were encapsulated in alginate hydrogel microcapsules, which provided physical protections to islets for improved viability and prevented immune rejection.[3] After that, a variety of hydrogels have been developed to incorporate therapeutic cells for tissue engineering and regenerative medicine.

Delivery of therapeutic cells is a promising strategy to enhance the repair capacity in damaged tissue.[4] The therapeutic cells can be stem cells that potentially differentiate into tissue-specific cell type or stromal cells that play supportive roles in regeneration by secreting paracrine factors and recruiting endogenous cells.[5] Although the outcomes of therapeutic cell delivery for treating human injuries have been studied for several decades, the results from preclinical and clinical trials have been varied due to poor cell retention and donor-to-donor variability.[6] Biomaterial carriers that can enhance cell retention and guide cell function have been used to improve the efficacy of cell delivery.[7] Hydrogels are particularly of interest due to their similarity with nature ECM and minimally invasive procedure of cell transplantation.[4] During cell encapsulation, hydrogel precursor solutions are mixed with cell suspensions and injected into the tissue defects. These solutions were allowed to fit any irregularly shaped tissue cavities and are then cured *in situ* to construct 3D milieu for encapsulated cells. To achieve a uniform distribution of cells throughout the hydrogels, the precursor solutions can be viscous but still permit to flow during injection, or the crosslinking step occurs rapidly after injection.[8, 9] In this way, hydrogels act as a physical barrier to retain transplanted cells in the sites of interest.

Common crosslinking mechanisms of hydrogels for cell encapsulation include physical (e.g. temperature, pH, ionic interactions) or chemical crosslinking (e.g. photopolymerization). Efforts have been made to improve the cytocompatibility of these crosslinking processes by searching reactions that occurred under mild conditions. For example, physically crosslinked hydrogels have been advanced to cure upon the mixture of gel components to avoid cytotoxic conditions, such as low pH, high temperature, or high ion concentrations.[10] For covalent hydrogels, Lin *et al.* reported the cytocompatibility of step-growth thiol-ene photopolymerization was much higher compared to acrylate chain photopolymerization during cell encapsulation due to high gelatin efficiency.[11] In addition, bio-orthogonal chemistries are especially suitable for *in situ* hydrogel crosslinking, as they do not interfere with native biochemical processes. DeForest *et al.* demonstrated the use of strain-promoted azide-alkyne reaction between di-fluorinated cyclooctyne and azide groups for cell encapsulation and showed improved cell viability by avoiding the use of copper catalyze.[12] Alge *et al.* developed hydrogels from the reactions between tetrazine and norbornene groups for cell culture, which is another cytocompatible choice.[13]

Hydrogels are also designed to instruct cell behaviors and function through biochemical and biophysical cues, including adhesion, matrix rigidity, topography, and the presentation of growth factors, for better regeneration outcomes.[14, 15] The ability to permit cell attachment needs to be considered first, as most therapeutic cells, including the most often used bone marrow derived human mesenchymal stem cells, are anchorage-dependent and rely on adhesion to survive. Cells bind to native ECM through transmembrane protein integrin and integrin-binding proteins, such as fibronectin, laminin, and collagen. Hydrogels made from some natural materials, such as collagen and fibrin, possess native adhesive binding ligands for cells to attach.[16, 17] Modifications on hydrogels made from other materials with cell-adhesive motifs are essential for cell attachment. The most common cell-adhesive ligand is RGD peptide, derived from natural ECM proteins.[18] Previous studies have shown the presence and concentration of RGD peptide on 2D hydrogels allowed fibroblasts to attach and spread.[19] However, evidence suggests that cell behavior in 3D cell cultures are significantly varied.[20] Burdick *et al.* studied the effects of RGD modification of cell behavior in both 2D and 3D cultures using PEG-diacrylate hydrogels.[21] Although similar results of osteoblast adhesion and spreading were shown on 2D RGD-presenting hydrogel surface, no significant difference in cell viability and spreading was shown between control and RGD-presenting groups when cells were encapsulated in 3D hydrogels. Several other studies also verified the limited cell spreading in 3D cell cultures, which could be a huge concern as cell spreading is critical for the survival and function of anchorage-dependent cells. [22, 23] In recent years, evidence indicates that the function of cells encapsulated with 3D hydrogels, such as mechanotransduction signaling, can be altered as a result of rounded spreading.[24] It is clear that incorporating cell adhesive ligands alone is not enough to support cell settlement within 3D hydrogels.

These hydrogels are mostly cured with stable, covalent bonds. When cells are encapsulated within these water-swollen polymeric networks in hydrogels, they are trapped within the porous space between the network chains, which is referred to as mesh size. The mesh size is determined mainly by the molecular weight, concentration, and hydrophilicity of the hydrogel macromer and often in the nanometer scale, which can be calculated by the Peppas-Merrill equation.[25] Since the size of a cell is micron-scale and significantly larger than the mesh size, cells are constrained to rounded shape with restrained motion. The polymeric network constructs a restrictive physical barrier to cells in 3D cultures, which becomes the predominant factor in controlling cell behavior. Previous work has shown that cells can spread and differentiate better in a more loosely crosslinked network, which can be achieved by increasing molecular weight or lowering the concentration of hydrogel macromer. However, these loose networks still do not provide enough space for cell spreading, migration, and morphogenesis, and often do not have enough mechanical support to the cells. Therefore, it is important to create micrometer-scale space in hydrogels during 3D cell culture to overcome the physical constrains for better guiding cell function and improve therapeutic results.

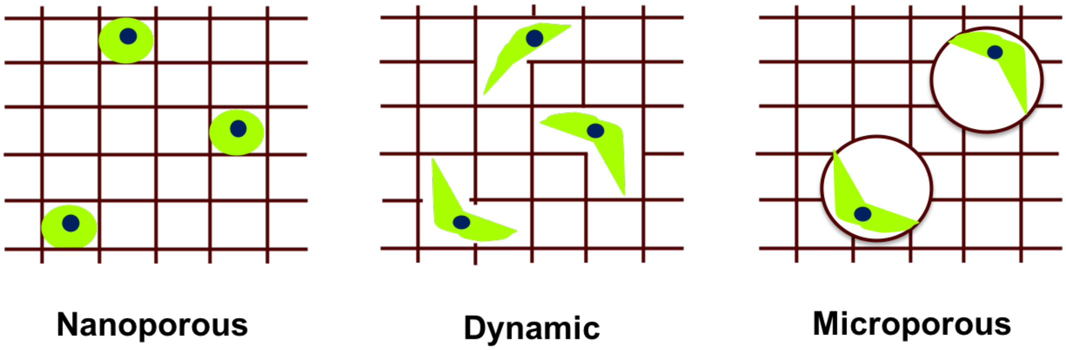

Figure I-1. Schematic showing 3D cell encapsulation within nanoporous, dynamic, and microporous hydrogels.

Overcoming the Physical Confinement of Cells in Hydrogels

Dynamic Hydrogels

Native ECM constantly undergoes remodeling, as cells degrade and reassembly the ECM during signaling.[26] For example, cells secrete ECM-modified proteins, such as MMPs, to degrade surrounding ECM for their migration. Recapitulating this dynamic remodeling feature in hydrogel designs is a major strategy to overcome the physical confinement of cells. There are two types of dynamic hydrogels that can permit cell motion, which are physically crosslinked hydrogels and covalent hydrogels with degradable linkages.

Physically crosslinked hydrogels are cured by molecular entanglements or secondary interactions. Since these polymeric networks often exhibit viscoelastic properties, cells are able to deform the surrounding substrate for their spreading.[27, 28] During the chain deformation, cells can also detect substrate rigidity by traction and, thus, their fate can be directed through biophysical cues. Huebsch *et al.* investigated MSC fate in ionically crosslinked alginate hydrogels and found MSC responded to rigidity of 3D microenvironments predominantly determined by traction forces.[29] In addition, cell tractions can cause the clustering of adhesive ligands in these hydrogels, which constitutes another factor in controlling cell fate and activity.[30] Self-assembled peptide hydrogels, another type of physically crosslinked hydrogels, undergo sol-gel phase transition upon mixing and also permit cell activities due to viscoelasticity.[10] However, the physical crosslinks in these hydrogels are reversible and often dissociated very quickly after implantation, which is not ideal for many tissue engineering applications. To solve this issue, researchers have developed double network hydrogels, in which one network possesses viscoelastic properties to promote cell activities, and the other one is covalently bonded to prevent the fast dissociation.[31-33] The physicochemical properties of the second covalent network can also be engineered, such as stiffness and ligand density, independently from viscoelasticity to instruct cell behaviors.[34]

The physical confinement of cells can also be removed by the cleavage of surrounding materials. While hydrolytic or photodegradable hydrogels have shown to improve cell spreading and proliferation,[35-37] the degradation rate is usually difficult to control in order to match the cell activities. The important work from Lutolf *et al.* introduced MMP-degradable peptide crosslinkers into PEG hydrogels, which were cleaved by proteases cells secreted during ECM remodeling.[38] They found that fibroblasts can invade into the gels and promote bone regeneration in rat cranium by combining cell-adhesive and cell-degradable motifs. Benton *et al.* further revealed that valvular interstitial cells could spread, migrate, and differentiate within PEG MMP-degradable hydrogels.[39] As cells break the bonds in the surrounding materials, they can continue to contract the matrices and determine their fate. The significant work from Khetan *et al.* demonstrated hMSCs exhibited high traction forces when cultured within protease-degradable hydrogels, and they chose their fate depending on the traction forces, instead of morphology.[40] Later, Caliari *et al.* found that the permissive environments after cell-mediated degradation in these 3D hydrogels were critical for cell spreading as they can activate YAP mechanotransduction, which was similar to the results in 2D cultures.[24] But these degradable hydrogels become weak in mechanics quickly and ultimately lose their mechanical support to the encapsulated cells.

An alternative strategy is to use covalent adaptable hydrogel network, which can reversibly form the bond after cleavage and, thus, maintain the mechanical integrity.[41, 42] For example, the reversible hydrazone bonds, formed from between aldehyde and hydrazine, can break due to cell stress and rapidly reform under cytocompatible conditions. Evidences have indicated that the highly adaptable hydrazone network can improve cellularity and ECM deposition.[43, 44] Boronates are another kind of reversible bond that possesses much faster association and dissociation kinetics, which have also shown to enhance cell spreading compared to static hydrogels.[45]

Microporous Hydrogels

Another way to overcome the physical constrains in hydrogels is to fabricate microporous hydrogels.[46] The pore size is normally greater than several tens of microns, which provides cells enough space to grow. The microporosity allows decoupling cell spreading and migration from the degradation of the surrounding material. When designing microporous hydrogels, it is important to avoid cytotoxic manufacturing procedures, which are often involved in methods of preparing other microporous polymer scaffolds, such as freeze-drying, salt leaching, gas foaming, and phase separation.[47] Three different strategies of microporous hydrogel fabrication are reviewed here, including biocompatible porogen, electrospinning, and annealing of hydrogel microspheres (i.e. microgels).

To prepare porogen-based microporous hydrogels, biocompatible porogen is embedded into hydrogel precursor solutions and, after crosslinking, they are dissolved to create the pores. The size and concentration of porogen can determine the microporous structure. Commonly used porogen includes gelatin microspheres, alginate beads, and microbubbles. Gong *et al.* and Hwang *et al.* utilizing gelatin beads with 150-200 µm size as a porogen to prepare microporous alginate hydrogels.[48, 49] In both works, cells showed enhanced proliferation and grew from the gel bulk to the cavities after porogen dissolution. Huebsch *et al.* introduced hydrolytically labile alginate beads into bulk alginate that degraded slowly and demonstrated this method of creating porogen-based microporous hydrogels could be injected into bone defects to evaluate cell delivery outcomes *in vivo*.[50] They showed that porous hydrogels resulted in improved hMSC proliferation and differentiation *in vitro*. After 12 weeks of transplantation, the remaining materials from porous hydrogels were significantly smaller compared to nonporous hydrogels, but the volume of new bone in porous hydrogel group was not significantly different from that in cell-only control, which could attribute to the low modulus of porous hydrogel group. Lima *et al.* reported the use of microbubbles as porogen to create porous agarose hydrogels and showed an increase in cartilage properties due to the enhanced permeability to nutrients.[51] In addition, porogen-based microporous hydrogels can be a useful platform to study cell-material interactions in a 3D environment. Haugh *et al.* investigated the interplay between stiffness and ligand chemistry on MSC differentiation within elastin-like protein microporous hydrogels and showed various types of cell behavior in response to stiffness from previously studied 2D and 3D cultures.[52] However, most porogen-based microporous hydrogels for cell delivery still encapsulate cells in the bulk part, and these cells need to escape from polymeric mesh to grow in pores. The migration process from bulk gel to pore can take several weeks and, thus, the extent of improvement in cell proliferation is limited. Recently, Ehsanipour *et al.* found that while these hydrogels possess a large volume of pore space, their hydraulic conductivity was not significantly different from conventional nanoporous hydrogels, suggesting these pore structures are not interconnected.[53] These limitations can potentially hamper the formation of the cellular network and prevent the infiltration of endogenous cells after implantation.

Electrospinning is a simple and popular method to produce nanofibers, but the use of electrospinning to fabricate fibrous hydrogels begins only in recent years.[54] The fibers are typically ranged from several tens to hundreds of nanometers in diameter. When the fibers are electrospun and collected on a ground or rotating mandrel, they are often in dry state because of solvent evaporation, and they can assemble into nanofibrous mats during the collection with interconnected micrometer pore structure. These electrospun hydrogel fibers are particularly of interest as they mimic the fibrous structure of natural ECM. However, the crosslinking step of these fibers limits the selection of materials, as precursor polymers need to be crosslinked before contacting aqueous solution to avoid dissolution and some toxic crosslinking agents, such as glutaraldehyde, may decrease the bioactivity of nature proteins including collagen.[55] The most common method to crosslink hydrogel fibers is photopolymerization. Several works demonstrated the use of photopolymerized gelatin methacryloyl nanofibrous mats to accelerate wound healing and spinal cord regeneration.[56-58] These studies showed significant cellular infiltration into these microporous mats after implantation, and one of these work achieved the formation of a vascular network *in vivo*. These hydrogel nanofibrous mats can be further engineered to improve *in vivo* regeneration outcomes potentially. The orientation of these fibers can be aligned to mimic anisotropic structure in natural ECM, which provides topographical cues for cell behaviors,[59] but the porosity of densely packed fibers may be sacrificed. Wade *et al.* explored the possibility of incorporating protease-sensitive hydrogel fibers by simultaneously electrospinning non-degradable and MMP-degradable precursor solutions onto a rotating mandrel, which could increase the porosity upon the dissolution of degradable hydrogel fibers to enhance cell infiltration.[60] Sundararaghavan *et al.* demonstrated a method to generate mechanical and adhesive ligand concentration gradients in hyaluronic acid hydrogel nanofibrous mats.[61] They showed improved cell infiltration with certain gradient orientation, suggesting these physicochemical gradients facilitated cell migration within these nanofibrous scaffolds. Despite these advances, electrospun hydrogel nanofibrous mats are mostly used as patches during transplantation due to the lack of injectability, which limits their use for therapeutic cell delivery.

The pioneering work from Scott *et al.* raised the concept of assembly hydrogel microspheres to fabricate microporous hydrogels.[62] They had to use some degradable microspheres as porogen in their system to create micrometer pores for cell culture since the size of their microspheres was only around 10 μm and the resulted pore size after assembly was too small. In 2015, the influential work from Griffin *et al.* assembled PEG microgels via transglutaminase-mediated reaction between peptide substrates K (Ac-FKGGERCG-NH_2) and Q (Ac-NQEQVSPLGGERCG-NH_2) presented on the surface of microgels. The diameter of microgels was from 30 to 150 μm, which resulted in the interconnected micrometer pore structure after assembly.[63] The authors also demonstrated the injectability of these microgels and *in situ* crosslinking in a mouse wound model. Due to the microporosity, these scaffolds showed significantly better cell culture outcomes *in vitro* and accelerated wound healing *in vivo* compared to conventional nanoporous hydrogels. Since this work, microgel assembled scaffolds have emerged as a new class of biomaterials for tissue engineering, and they are given the name "microporous annealed particle hydrogels" or "MAP hydrogels".

A wide range of materials and existing chemistries can be used to fabricate MAP hydrogels, as long as the method involves two-step crosslinking that produces microgels and assembles them together into scaffolds. The aforementioned work from Griffin *et al.* utilized Micheal addition reaction to synthesize PEG microgels and decorated the surface with other functional peptide ligands for assembly.[63] Later, Elias *et al.* from the same group compared three different microgel assembly chemistries for hyaluronic acid MAP hydrogel fabrication, including transglutaminase-mediated crosslinking, light-based radical polymerization, and amine/carboxylic acid-based crosslinking.[64] They found all three chemistries resulted in interconnected pore structures within MAP hydrogels and contributed to excellent cell spreading. Caldwell *et al.* prepared two kinds of off-stoichiometric PEG microgels with excessive azide or dibenzocyclooctyne groups that could be assembled upon mixing via strain-promoted azide-alkyne cycloaddition.[65] They compared cell behaviors in MAP hydrogels with different pore sizes (resulting from different sizes of microgels) and found large pore size was important for robust cell spreading and formation of cellular network when using microgels that over 100 μm size. Recently, Sheikhi *et al.* expanded this platform to natural proteins by using gelatin methacryloyl, where they physically crosslinked microgels first and photopolymerize to assemble them into MAP hydrogels.[66] In addition, the assembly process can also be achieved by introducing a multi-functional linker. For example, Mealy et al. fabricated thiol-ene hyaluronic acid microgels with adamantane groups on the surface and added cyclodextrin-functionalized hyaluronic acid for assembly via guest-host interaction.[67] They also demonstrated the injectability of these granular hydrogels due to shear-thinning properties and leveraged the modularity to combine two distinct microgels with varying degradability into a single hydrogel for multiplexing of small molecule release. Overall, MAP hydrogels offer cells microporous environments that do not restrict cell behavior and possess great injectability for *in vivo* implantation. Therefore, they can be potentially leveraged as a therapeutic cell delivery platform for tissue engineering applications.

Innovation and Approaches

Our goal is to develop a cell-instructive hydrogel platform that can direct hMSC behavior and deliver them *in vivo* for bone tissue engineering. We utilized the emerging MAP hydrogel platform to encapsulate hMSCs. Unlike conventional nanoporous hydrogels, MAP hydrogels are inherently microporous after assembly and, thus, cells are no longer trapped within a physical confinement. Instead, they interact with the microgel surface within the hydrogels, which imparts MAP hydrogels some 2D features in the 3D scaffolds. It is important as it provides us opportunities to leverage the knowledge of cell-material interactions in myriad 2D studies to instruct cell behaviors in 3D MAP hydrogels. In addition, microgel building blocks are injectable, making the cell delivery procedure minimally invasive.

It should be appreciated that we used thiol-ene click chemistry to prepare MAP hydrogels. Due to the step-growth nature, off-stoichiometric PEG thiol-ene microgels were synthesized with excessive norbornene groups and then assembled by a secondary thiol-ene photopolymerization with the addition of bis-thiol linker. This sequential reaction simplifies the system by utilizing the same functional groups. Thiol-ene reaction also offers facile tuning of the physicochemical properties of resulting microgels, which can be leveraged to study the cell-material interactions in MAP hydrogels and optimize the material compositions for therapeutic cell delivery. We investigated the effects of linker concentration, stiffness, degradability, and integrin signaling on hMSC behaviors in MAP hydrogels. The optimized formulation was implanted into a mouse femoral defect model to evaluate the outcomes of bone healing. The work is presented in Chapters II and III. In addition, thiol-ene photopolymerization has fast kinetics and good cytocompatibility, making the system suitable for cell encapsulation.

Another advantage of MAP hydrogels is the high modularity so that multiple formulations of microgels can be combined in a pattern. The spatiotemporal patterning of microgels with varying physicochemical gradients can be useful for many tissue engineering applications. We invented a method to pack microgels with varying formulations layer-by-layer to generate physicochemical gradients. This method was to, for the first time, introduce a mixer module into droplet microfluidics and program the flow rates over time. The generated microgel gradients were maintained after injection and annealed into MAP hydrogels via thiol-ene click reaction. This work is presented in Chapter IV.

The microgels were also used as biomaterial inks for 3D printing to construct MAP hydrogels with anatomically relevant shapes. The microgels possess excellent printability, as their small scale permits extrusion, and the crosslinked network does not require any solidification after extrusion. Importantly, these microgels exhibited inherent cohesive force after extrusion for the stability of printed structures. A secondary thiol-ene crosslinking can assemble printed constructs into MAP hydrogels. This work is presented in Chapter V.

CHAPTER II

ASSEMBLY OF PEG MICROGELS INTO 3D CELL-INSTRUCTIVE MICROPOROUS ANNEALED PARTICLE SCAFFOLDS VIA THIOL-ENE CLICK CHEMISTRY*

Overview

The assembly of microgel building blocks into 3D MAP hydrogels is an emerging strategy for tissue engineering. A key advantage is that the inherent microporosity of these scaffolds provides cells with a more permissive environment than conventional nanoporous hydrogels. Here, norbornene-bearing PEG based microgels were assembled into 3D cell-instructive scaffolds using a PEG-DT linker and thiol-ene click photopolymerization. The bulk modulus of these materials depended primarily on the crosslink density of the microgel building blocks. However, the linker and initiator concentrations used during assembly had significant effects on cell spreading and proliferation when hMSCs were incorporated in the scaffolds. The cell response was also affected by the properties of the modular microgel building blocks, as hMSCs growing in scaffolds assembled from stiff but not soft microgels activated YAP signaling. These results indicate that PEG MAP scaffolds assembled via thiol-ene click chemistry can be engineered to provide a cell-instructive 3D milieu, making them a promising 3D platform for tissue engineering.

---

*Reprinted with permission from “Assembly of PEG Microgels into Porous Cell-Instructive 3D Scaffolds via Thiol-Ene Click Chemistry” by Xin *et al.*, 2018, *Advanced Healthcare Materials*, 7 (11), 1800160, Copyright 2018 by John Wiley and Sons.

Introduction

Hydrogels are of broad interest for tissue engineering as their polymer networks can be engineered to mimic the native tissue environment.[13, 68] Synthetic hydrogels presenting tissue microenvironmental cues, such as bioactive molecules, topography, and substrate stiffness, have been proposed as scaffolds that recapitulate cell-instructive features of the natural ECM for tissue engineering.[69-71] However, an important and often overlooked challenge in developing 3D cell-instructive hydrogels is that conventional hydrogels are porous on the nanoscale and, therefore, constitute a restrictive barrier that must be degraded to permit cell spreading, migration, and deposition of new ECM. Strategies using porogens, foaming agents, and freeze-drying have been developed to impart microscale porosity in hydrogels for tissue engineering,[50, 72-74] but these methods generally require additives and post-processing steps that may not be cytocompatible and can preclude cell incorporation during assembly.

An emerging paradigm in the development of porous hydrogels for tissue engineering is the assembly of 3D scaffolds from hydrogel microspheres or microgels.[62-65, 75] This approach involves synthesizing microgel building blocks in a preliminary step, packing them together, and then crosslinking them into a 3D MAP structure. Due to the void spaces between the microspheres, this approach results in materials with a highly interconnected microporous structure without the need for any porogens or foaming agents. Griffin *et al.* reported that the interconnected microporosity of PEG microgel-based scaffolds translates to accelerated healing compared to conventional hydrogels in a murine dermal wound healing model.[63] Similarly, Nih *et al.* recently demonstrated that hyaluronic acid MAP scaffolds resulted in accelerated brain healing compared to conventional hydrogels when the materials were injected into stroke cavities in mice.[76] In both studies, the superior results were attributed to the inherent microporosity of the MAP scaffolds permitting faster migration of endogenous cells into the scaffold. Other attractive features that make MAP scaffolds promising for tissue engineering are the ability to tune the physicochemical properties of the microgel building blocks to direct cell-material interactions and the potential for cell incorporation during microgel assembly, as recently demonstrated by Caldwell *et al.*.[65]

While a number of chemical strategies are suitable for assembling microgels into 3D scaffolds, we have chosen to focus on thiol-ene chemistry because it offers several notable advantages. The first is that synthesizing suitable microgels is straightforward; microgels synthesized via an off-stoichiometric thiol-ene polymerization will be readily amenable to crosslinking with a bis-thiol or bis-norbornene linker, as appropriate. Thiol-ene synthesis of microgels also offers facile tuning of physicochemical properties by incorporating ECM mimetic peptides and modulating crosslink density.[77] Specifically regarding assembly of microgels into 3D scaffolds, an important advantage of thiol-ene chemistry is its potential for spatiotemporal control via photoinitiation. In contrast, previously reported strategies such as transglutaminase mediated crosslinking, thiol-Michael additions, and strain-promoted azide-alkyne crosslinking result in assembly upon mixing and do not afford spatiotemporal control.[63-65] Finally, thiol-ene chemistry offers fast reaction kinetics for assembly and superior cytocompatibility compared to chain-growth photopolymerization of vinyl groups,[11, 78] the latter of which is attractive for incorporating therapeutic cells like hMSCs during assembly.

Here, we report the assembly of PEG MAP scaffolds using photoinitiated thiol-norbornene click chemistry as a potential platform for hMSC delivery. The effects of varying concentrations of linker and initiator applied during assembly on mechanical properties and porosity of MAP scaffolds as well as hMSC cellularity were studied. The cell spreading trends with scaffold stiffness were also compared between hMSCs seeded in conventional bulk hydrogels and MAP scaffolds. Finally, YAP nuclear localization in hMSCs cultured in MAP scaffolds was studied to evaluate cell mechanosensing in scaffolds prepared from microgels with different moduli.

Materials and Methods

Materials

Tetrafunctional PEG-Nb macromers (5 and 20 kDa) were synthesized from PEG-OH precursors via esterification with 5-norbornene-2-carboxylic acid (Alfa Aesar) using diisopropyl carbodiimide activation, as described by Jivan *et al.*.[79] The polymers were dialyzed against deionized water prior to use, and percent functionalization was determined to be greater than 95% via ^{1}H NMR spectroscopy analysis. The cell adhesive peptide CGRGDS was prepared via microwave-assisted solid phase peptide synthesis and standard Fmoc methods. The coupling times and temperatures were 6 mins at 50 °C for cysteine and 5 mins at 75 °C for other amino acids. Amino acids were activated with N,N,N',N'-tetramethyl-O-(1H-benzotriazol-1-yl)uronium hexafluorophosphate (Chemimpex), and Fmoc deprotection was performed with 5% piperazine (Alfa Aesar) and 0.1M hydroxybenzotriazole (Advanced Chemtech) for 3 mins at 75 °C. Peptides were cleaved from the resin with a cocktail of trifluoroacetic acid (Sigma)–triisopropyl silane (Sigma)–water–phenol (Sigma) (94: 2.5: 2.5: 1), precipitated in ice cold diethyl ether, and then purified by reverse-phase HPLC in water/acetonitrile with 0.1% TFA. Peptide composition was verified by MALDI-TOF MS analysis. LAP was synthesized following the methods of Fairbanks et al. without modification and verified by ^{1}H NMR spectroscopy and electrospray ionization mass spectrometry prior to use.[77]

Preparation of Electrosprayed Microgels

Tetra-arm PEG-Nb and PEG-DT (M_w = 3,400 Da, Laysan Bio.) were mixed off-stoichiometrically with cell-adhesive peptide ligand CGRGDS (1 m*M*) and LAP (2 m*M*). The final working concentration of PEG-Nb was 10 wt% and the [SH]:[ene] ratio for PEG-DT and PEG-Nb was 0.75:1 so that unreacted norbornene groups would be available for microgel assembly. Two PEG-Nb molecular weights (5 and 20 kDa) were used to prepare microgels with varying crosslink density and mechanical properties (termed PEG5 and PEG20, respectively). The precursor solutions were then electrosprayed into light mineral oil with Span 80 (0.5 wt%), similar to the approach of Qayyum *et al.*.[80]

The submerged electrospraying setup consisted of DC voltage source (ES30N-5W, Gamma High Voltage Research), syringe pump (KDS 100, KD Scientific), syringe with blunt needle, grounded ring, UV light source and light mineral oil for microgel collection (Figure II-6). The voltage was adjusted to accommodate for the slightly different viscosities of the microgel precursor solutions with different molecular weight PEB-Nb. Here, 4 and 6 kV were applied for PEG5 and PEG20 microgel synthesis, respectively. Other parameters included 12 mL/hr flow rate, 16 mm needle-to-ring distance and 22 gauge needle size. The mineral oil was irradiated with 365 nm UV light (60 mW/cm^2, Lumen Dynamics Omnicure S2000 Series) during electrospraying to photopolymerize the microgels. The resulting microgels were centrifuged, washed 1X with 30% ethanol, and then washed 5X with phosphate buffered saline to remove mineral oil and surfactant. The microgels were swollen at 4 °C overnight to reach equilibrium before use.

Preparation of 3D Scaffolds

To prepare thiol-ene PEG MAP scaffolds, microgels were filled in a 6 mm diameter, 50 µL silicone circular mold. Subsequently, varying volumes of 20 wt% PEG-DT (2, 4, or 8 µL) and 100 m*M* LAP (1, 2, or 4 µL) were added to achieve the desired concentrations and mixed by pipetting. The microgels were then assembled into scaffolds by UV irradiation (365 nm, 10 mW/cm^2, 3 min). This assembly process was also monitored by *in situ* photopolymerization on a rheometer (Physica MCR 301, Anton Paar) under a time sweep at 1% strain and 1 rad s^{-1}.

For comparison in cell studies, bulk hydrogels were prepared using tetra-arm PEG-Nb (5 and 20 kDa, 10 wt%) and enzymatically-degradable peptide crosslinker KCGPQGIWGQCK (purchased from GL Biochem) with cell-adhesive peptide ligand

CGRGDS (1 m*M*) and LAP (2 m*M*). The [SH]:[ene] ratio on bulk hydrogels was also maintained at 0.75:1. 50 µL of precursor solution was added into an 8 mm silicone circular mold and photo-crosslinked by UV irradiation (365 nm, 10 mW/cm^2, 3 min).

Characterization

The macroscopic morphology of MAP scaffolds was observed using a stereomicroscope (Stemi 508, Zeiss) with 1X objective. The inner structure of MAP scaffolds was imaged by confocal microscopy (FV1000, Olympus). For visualization, Alexa Fluor 488-succinimidyl ester (Invitrogen) was conjugated to the N-terminus of the CGRGDS peptide in the microgels. Forty z-slices were taken in each z-stack, spanning a total of 200 µm depth. To visualize the interconnected pore structure, high molecular weight tetramethylrhodamine isothiocyanate-dextran (155 kDa, Sigma) was diffused into MAP scaffolds and imaged by confocal microscopy.

In addition, the macroscopic mechanical properties of MAP scaffolds with varying linker and initiator concentrations were measured by oscillatory shear rheology (Physica MCR 301, Anton Paar) at 1% strain and 1 rad s^{-1} with a gap size of 600 µm. Microgels were also sectioned into 25 µm slices on a cryostat, and the localized Young's modulus of individual microgels and bulk hydrogels were measured by Atomic Force Microscopy (Dimension Icon, Bruker) with an SiO_2 colloidal probe (5 µm diameter, spring constants 0.6 N/m, Novascan).[81]

Cell Culture

hMSCs were obtained from the Institute of Regenerative Medicine at Texas A&M University and cultured in low-glucose Dulbecco's Modified Eagle's Medium (Corning) with 10% (v/v) fetal bovine serum, penicillin (50 U/mL), streptomycin (50 μg/mL), and basic fibroblast growth factor (1 ng/mL) at 5% CO_2 and 37 °C. hMSCs were used up to passage 5. Single-cell suspensions of hMSCs (10 μL) were mixed with microgels in the silicone mold during assembly process for cell seeding at a density of 20,000 cells per scaffold. To seed hMSCs into bulk hydrogels, cell suspensions were mixed with precursor solutions and encapsulated via UV crosslinking (365 nm, 10 mW/cm^2, 3 min).

Immunostaining and Imaging

The viability of hMSCs encapsulated in MAP scaffolds was tested using Live/Dead viability kit (L3224, Invitrogen). For immunostaining, samples were fixed after the desired culture time using 4% formaldehyde for 15 min at room temperature. Cytoskeletal staining was performed using rhodamine phalloidin (1:40, Invitrogen), and cell nuclei were stained with DAPI (1:1000, Biolegend). hMSC proliferation after 24 h was evaluated using the Click-iT EdU Alexa Fluor 647 kit (C10340, Invitrogen). Evaluation of cell mechanotransduction was performed by immunohistochemistry utilizing antibodies against YAP (1:200, Santa Cruz). Goat anti-mouse IgG-FITC (1:100, Jackson ImmunoResearch) was used as a fluorescent secondary antibody. MAP scaffolds were then counter stained with DAPI (1:1000, Biolegend). All the samples were imaged in a glass bottom petri dish (MarTek) by confocal microscopy (FV1000, Olympus).

Image Analysis

All image analysis was performed using ImageJ software (NIH). For porosity measurements, each z-stack of fluorescent-labeled MAP scaffolds was thresholded to differentiate between the scaffold and pores. The black voxels were then measured using Image J's Voxel Counter plugin to obtain the thresholded volume and volume of stack. The porosity of scaffolds was then calculated as shown in the formula below:

$$\text{Porosity (\%)} = \frac{\text{Thresholded volume}}{\text{Volume of stack}} * 100\%$$

For cell volume quantification, each cellular domain was determined by intensity-based thresholding method from actin staining in z-stack images. The volume of each cell was measured by Image J's 3D Objects Counter plugin. YAP nuclear/cytosolic ratio was calculated by the ratio of average intensity in nucleus and cytosol. Volume and intensity were also determined by Image J's 3D Objects Counter plugin and the formula shown below:

$$\text{YAP nuclear/cytosolic ratio} = \frac{\frac{\text{Nuclear YAP intensity}}{\text{Volume of nucleus}}}{\frac{\text{Cytosolic YAP intensity}}{\text{Volume of cytosol}}}$$

Statistical Analysis

All experiments were conducted with at least three independent scaffolds, and four different regions per scaffold were imaged. Cellular quantification was measured with at least 50 cells per group. Results are reported as the mean ± standard deviation. Student's t-test was used to determine significant differences between two groups. Significance is indicated by * corresponding to $p < 0.001$, respectively.

Results

Assembly of PEG Microgels into Porous Scaffolds with Thiol-ene Chemistry

In order to assemble scaffolds, the PEG microgels were packed in a 6 mm diameter silicone circular mold with the addition of PEG-DT linker and LAP photoinitiator and then the samples were exposed to UV light for polymerization (365 nm, 10 mW/cm^2, 3 min, Figure II-1a). The microgels generated from previously mentioned electrospraying parameters were approximately 200 µm in diameter, as characterized by microscopy (Figure II-7). Figure II-1b shows a macroscopic image of a thiol-ene PEG5 scaffold, and the particulate morphology of the surface is clearly visible. Confocal microscopy imaging of Alexa Fluor 488-labeled scaffolds revealed interconnected pores that were several hundred microns in size (Figure II-1c). To further characterize the assembly process, the storage moduli of PEG5 and PEG20 scaffolds were monitored during *in situ* photopolymerization of microgels on a rheometer (Figure II-1d). Upon irradiation, a 1.5-2 fold increase in storage modulus was observed within 10 seconds and the final modulus of the PEG5 scaffolds was higher than that of the PEG20 scaffolds. Fluorophore-labeled dextran was also diffused into the MAP scaffolds and demonstrated the interconnectivity of the micropore structure (Figure II-1e). In addition, photomasks with simple shapes were applied during UV irradiation to emphasize the spatiotemporal control of thiol-ene microgel assembly (Figure II-8).

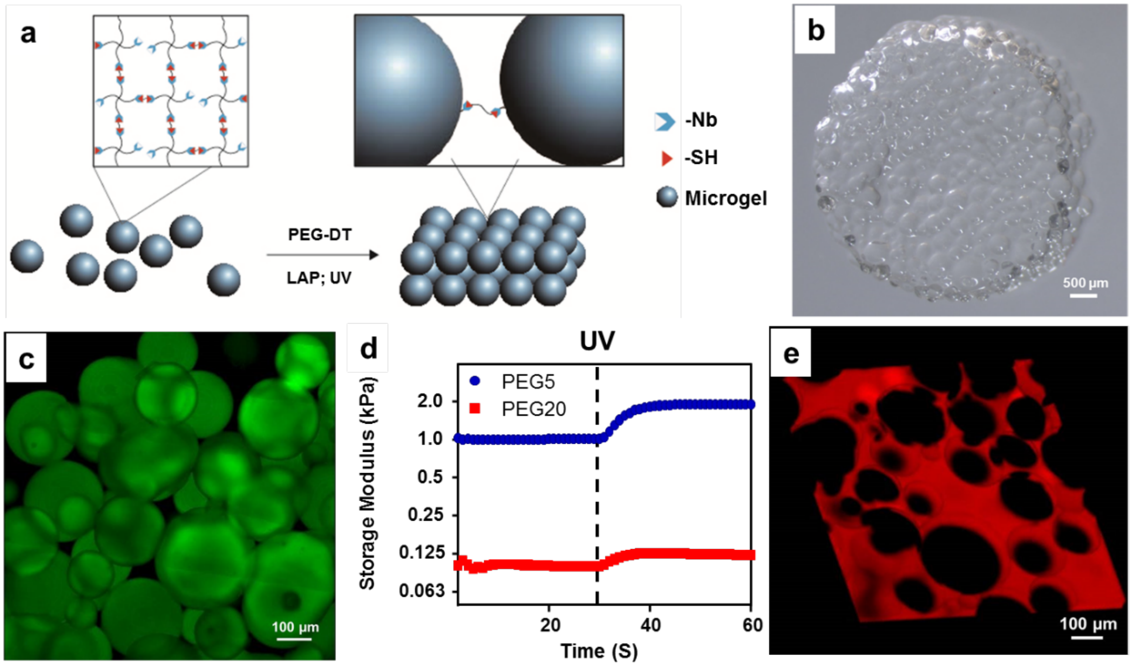

Figure II-1. PEG MAP scaffolds with interconnected micropores are successfully assembled through thiol-ene photopolymerization. a) Schematic illustrating thiol-ene assembly of microgels into scaffolds. b) Stereomicroscope image of a PEG5 MAP scaffold. c) Z-stack image of a PEG5 MAP scaffold labeled with Alexa Fluor 488-succinimidyl ester (top-down view of a 3D reconstruction). d) Storage modulus evolution of PEG5 and PEG20 during *in situ* photopolymerization into scaffolds. e) Representative 3D image of a MAP scaffold immersed in solution of fluorescently labeled high molecular weight dextran, demonstrating pore interconnectivity. Reprinted with permission from Xin *et al.*, 2018, *Advanced Healthcare Materials*, 7 (11), 1800160, John Wiley and Sons.

Characterization of Scaffold Properties

During the assembly process, varying amounts of linker and initiator were applied and their effects on bulk mechanical properties and porosity were studied

(Figure II-2). As the [SH]:[ene] ratio of PEG5 microgels was 0.75:1, the theoretical concentration of available norbornene groups was 18 m*M* for PEG5. While this translates to an upper boundary of 9 m*M* for PEG-DT to react with all available norbornene groups, we found that only 2 m*M* PEG-DT was required to assemble PEG5 microgels into bulk scaffolds, as shown in Figure 2a. Interestingly, adding more PEG-DT only slightly enhanced the storage modulus of MAP scaffolds for both PEG5 and PEG20. Similarly, varying the amount of LAP did not influence the storage modulus significantly (Figure II-2b). However, increasing the amount of PEG-DT linker did increase the scaffold porosity from 17% to 36% as (Figure II-2c), presumably due to the different volumes of PEG-DT solution added. As shown in fluorescent z-stack images (Figure II-9), microgels were distributed evenly throughout the scaffolds in low linker concentration group, while large voids and clusters of microgels were observed in the high linker concentration group.

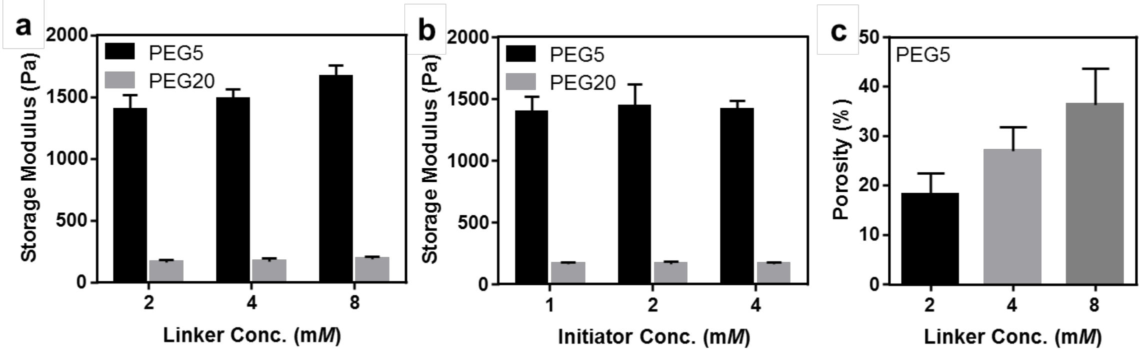

Figure II-2. Effect of varying linker and initiator concentrations on scaffold properties. Storage modulus of PEG5 scaffolds assembled using varying a) linker and 1 mM initiator and b) 2 mM linker and varying initiator concentrations. c) Porosity of PEG5 scaffolds prepared with the varying linker concentrations and 1 mM initiator. Data are for n = 3 scaffolds for each group. Reprinted with permission from Xin *et al.*, 2018, *Advanced Healthcare Materials*, 7 (11), 1800160, John Wiley and Sons.

Characterization of hMSC Viability, Spreading, and Proliferation

Following characterization of MAP scaffolds, hMSCs were encapsulated within PEG5 scaffolds with varying amounts of linker and initiator. hMSCs spread to surround the microgels and grew within the micropores after 24 h of culture to form a 3D cellular network within the MAP scaffolds. However, drastic differences in cell numbers and spreading were observed for the varying concentrations of crosslinker and initiator (Figure II-3a). Despite the lower scaffold porosity, cellularity was enhanced in the low concentration groups, and the cell volume was 2-3 fold higher compared to the high concentration groups (Figure II-3b). These results were not due to viability differences, as Live/Dead staining indicated high viability (> 80%) in all groups (Figure II-3c and II-10). Further analysis showed that 36% of hMSCs encapsulated within MAP scaffolds in the low concentration group were proliferating, compared to only 7% with a high PEG-DT concentration and 2% with a high LAP concentration (Figure II-3d and II-11).

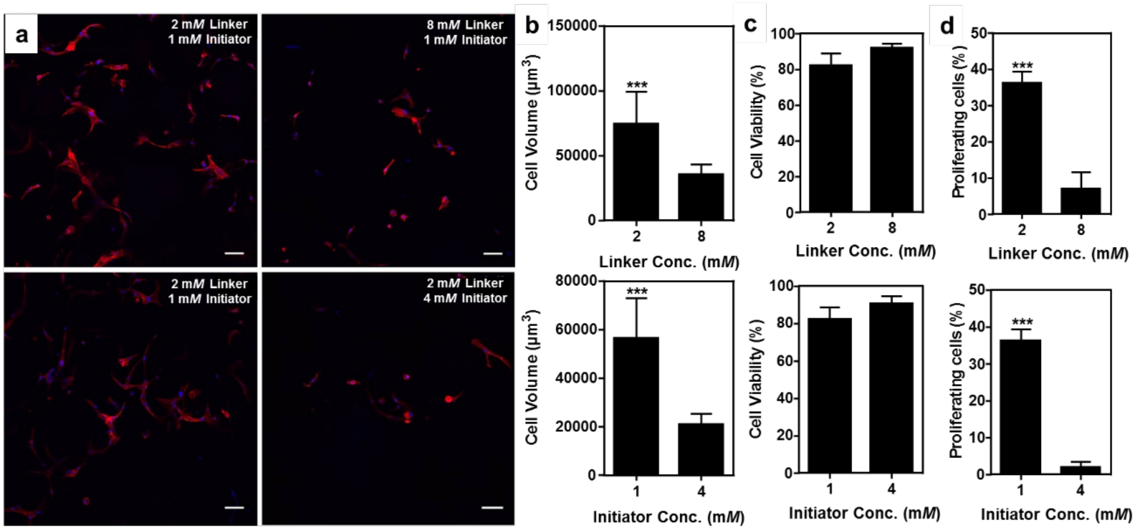

Figure II-3. hMSC spreading and proliferation in MAP scaffolds was influenced by the linker and initiator concentrations used during scaffold assembly. a) Maximum intensity Z-projection of cytoskeleton staining of hMSCs cultured in PEG5 scaffolds after 1d. Red represents F-actin and blue represents nuclei. Scale bars are 100 µm. b) Cell volume, c) cell viability, and d) percent proliferating cells plotted versus linker and initiator concentrations after 1d. Data are for n > 50 cells. *: $p < 0.001$. Reprinted with permission from Xin *et al.*, 2018, *Advanced Healthcare Materials*, 7 (11), 1800160, John Wiley and Sons.

Effect of Microporosity on hMSC Spreading Trends with Increasing Stiffness

hMSC spreading trends in conventional bulk hydrogels and MAP scaffolds were also compared (Figure II-4). Prior to incorporating hMSCs, we compared the moduli of the microgels and conventional hydrogels. Nanoindentation testing by atomic force microscopy on individual microgels revealed localized Young's moduli of 35.8 and 7.6 kPa for PEG5 and PEG20 microgels, respectively (Figure II-4a). Bulk hydrogels from same molecular weight PEG-Nb exhibited equivalent localized moduli. In bulk hydrogels, hMSCs spread better in PEG20 than PEG5 at Day 1 (Figure II-4b), as expected due to the lower crosslinking density. However, the degree of cell spreading was inferior to the MAP scaffolds. When cultured in MAP scaffolds, hMSCs spread well along the surface of the PEG5 spheres and exhibited large cell volume after 24h, whereas they stayed rounded within PEG20 scaffolds (Figure II-4c). As the culture extended, hMSCs continued to proliferate and spread in both groups at Day 7.

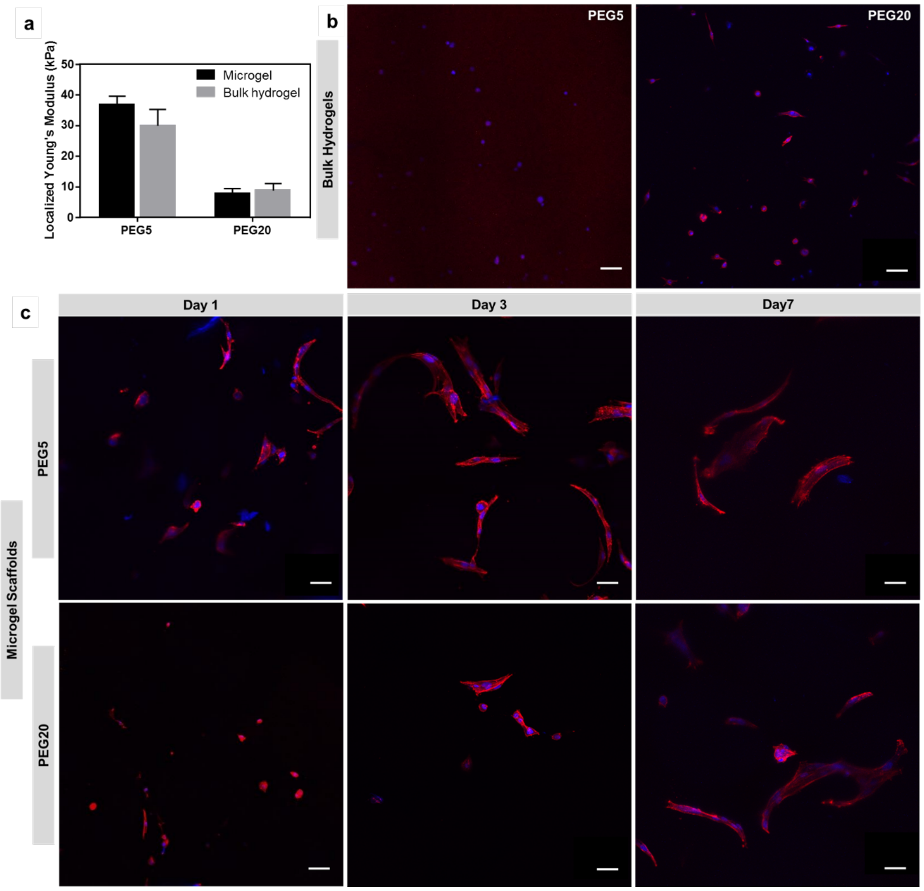

Figure II-4. hMSCs in MAP scaffolds of varying stiffness exhibit opposite trends in spreading compared to conventional hydrogels. a) Localized Young's modulus of individual microgels and bulk hydrogels made from PEG5 and PEG20 measured by AFM. b) Maximum intensity Z-projection of cytoskeleton staining of hMSCs cultured in PEG5 and PEG20 bulk hydrogels after 1d. c) Maximum intensity Z-projection of cytoskeleton staining of hMSCs cultured in PEG5 and PEG20 MAP scaffolds after 1, 3, and 7d. Red represents F-actin and blue represents nuclei. Scale bars are 50 µm. Reprinted with permission from Xin *et al.*, 2018, *Advanced Healthcare Materials*, 7 (11), 1800160, John Wiley and Sons.

Effect of Microgel Mechanical Properties on YAP Nuclear Localization

In order to study the effects of microgel stiffness on the cell response, we immunostained for YAP after 72h culture to evaluate hMSC mechanosensing in the MAP scaffolds.[82] Fluorescence images from confocal microscopy indicated enhanced YAP nuclear localization in MAP scaffolds with increasing stiffness. Quantification of the YAP nuclear/cytosolic ratio revealed that the YAP relative nuclear intensity was approximately 2-fold higher for hMSCs cultured in PEG5 scaffolds than in PEG20 scaffolds (Figure II-5a). The averaged cell volume in PEG5 scaffolds was also 8-fold higher (Figure II-5b). Some cells in PEG20 scaffolds appeared to aggregate with other cells as shown in representative images (Figure II-5c).

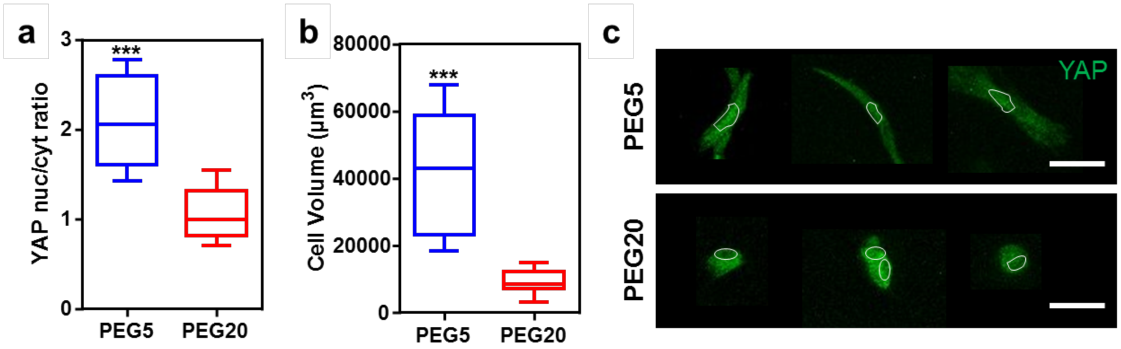

Figure II-5. YAP nuclear activation in hMSCs is up-regulated by increasing matrix stiffness in MAP scaffolds. a) YAP nuclear localization for hMSCs encapsulated within PEG5 and PEG20 MAP scaffolds. b) Average cell volume of hMSCs cultured in MAP scaffolds of varying stiffness. c) Representative images of hMSC YAP nuclear localization. White circles represent the position of nucleus (Note: two cells are shown clustered together in the middle image for the PEG 20 group). Scale bars are 50 μm. *: $p < 0.001$. Reprinted with permission from Xin *et al.*, 2018, *Advanced Healthcare Materials*, 7 (11), 1800160, John Wiley and Sons.

Discussion

The assembly of microgels into 3D microporous hydrogels is an emerging paradigm in biomaterials. Because of their interconnected microporosity, MAP scaffolds may be more effective for certain tissue engineering applications than conventional hydrogels, which are only nanoporous.[63, 65] These scaffolds are more permissive to cell spreading and migration, and tuning the physicochemical properties of the microgels should provide a means for directing the cellular response. However, cell-material interactions are different in these materials compared to conventional hydrogels, and the effects of variables in the MAP scaffold design and assembly processes on cells have not been studied. The objective of this work was to address this knowledge gap.

Here, we used thiol-ene click chemistry to electrospray PEG microgel and assemble them into scaffolds. This approach has some important advantages, including facile incorporation of bioactive peptide precursors and rapid kinetics.[77, 83, 84] We used norbornenes to conjugate thiolated RGD cell adhesive peptides and assemble the microgels via a PEG-DT linker, although any bis-thiol linker could be used. Importantly, we were also able to tune the crosslinking density and modulus of the microgel building blocks by adjusting the molecular weight of the PEG-Nb macromer. These microgel building blocks were rapidly assembled into 3D scaffolds upon UV irradiation, which is helpful to shorten cell encapsulation time (Figure II-1d). In addition, we observed interconnected micropores within the scaffolds, which indicates the success of synthesizing microporous scaffolds using this method (Figure II-1e).

We also seeded hMSCs into the scaffolds during microgel assembly. Our results complement the recent work of Caldwell et al. who showed that hMSC spreading differs depending on microgel size,[65] but did not study how the extent of crosslinking between the microgels affects the cells. To understand this latter variable, we studied hMSC spreading when using varying amounts of linker and initiator for microgel assembly. While increasing the amount of linker resulted in increased porosity and looser packing of the microgels, likely due to the larger volume of solution being added, this was not beneficial to the cell response. Rather, our results show that low concentrations of linker and initiator are critical for cell spreading and growth in our system (Figure II-3). As shown in Figure II-9, microgels tended to fuse together in high linker concentration group, which appeared to limit the ability of cells to spread. It is also possible that the use of a PEG-based linker may have reduced the availability of RGD peptides, which would also inhibit cell spreading. Regardless, in our present system, using low concentrations of linker and initiator for microgel assembly appears to be critical.

Within MAP scaffolds, cells interact with the microgel surfaces as if they are a 2D material. This feature is significant because recent studies have noted differences in cell-material interactions between 2D and 3D environments.[85-87] Because of the restrictive environment in conventional bulk hydrogels, cells spread less in more densely crosslinked networks and degradation is required to allow more spreading.[40, 88] Indeed, we observed this trend in hMSC spreading in conventional PEG thiol-ene hydrogels even with a peptide degradable crosslinker (Figure II-4b). In contrast, when culturing in non-degradable MAP scaffolds prepared with the same PEG molecular weight and [SH]:[ene] ratio, and thus the same crosslink density, the spreading trend of hMSCs with stiffness in the 3D environment was similar to what is observed in 2D cultures (Figure II-4c). This observation confirmed that the microporosity of MAP scaffolds provides cells with a 3D environment that is more permissive to cell spreading.

Inspired by the fact that our cell spreading trends were similar to 2D cultures, we subsequently investigated hMSC mechanosensing in our MAP scaffolds to see if this would also be similar. We specifically characterized YAP/TAZ nuclear staining in scaffolds assembled from microgels of varying moduli, since modulus is well known to influence hMSC fate and function,[89, 90] and YAP/TAZ is a well-established marker of mechanosensing.[82, 91] Importantly, Caliari et al. recently reported that hMSC mechanosensing in conventional hydrogels is distinctly different from 2D cultures, with higher modulus hydrogels resulting in decreased rather than increased YAP nuclear staining.[24] In contrast, we observed the opposite trend in our MAP scaffolds, as hMSCs exhibited a higher YAP nuclear/cytosolic localization and larger cell volume in scaffolds assembled from higher modulus microgels (35.8 kPa vs. 7.6 kPa; Figure II-5). Based on this result, hMSC mechanosensing in MAP scaffolds appears to be similar to what has been observed in 2D culture,[92] which could be promising for the future development of 3D cell-instructive scaffolds for tissue engineering.

Conclusion

We demonstrate here thiol-ene chemistry based assembly of porous PEG MAP scaffolds. In addition, we show the suitability of these materials as a platform for hMSC encapsulation. Key findings are that low concentrations of crosslinker and initiator applied during the assembly process are critical for maintaining a permissive environment within these scaffolds, and that the PEG microgel properties can be tuned to influence the behavior of cells incorporated during assembly. The 3D permissive environment due to microporosity provides a means to regulate cell spreading and mechanosensing by material properties, with trends in cell behavior being similar to what has been observed in 2D cultures. Based on these results, these materials appear to be a promising platform that could have broad utility for tissue engineering and regenerative medicine. Future studies should investigate whether microgels containing specific biophysical and biochemical cues can be used to enhance *in vivo* tissue engineering efficacy.

Supporting Information

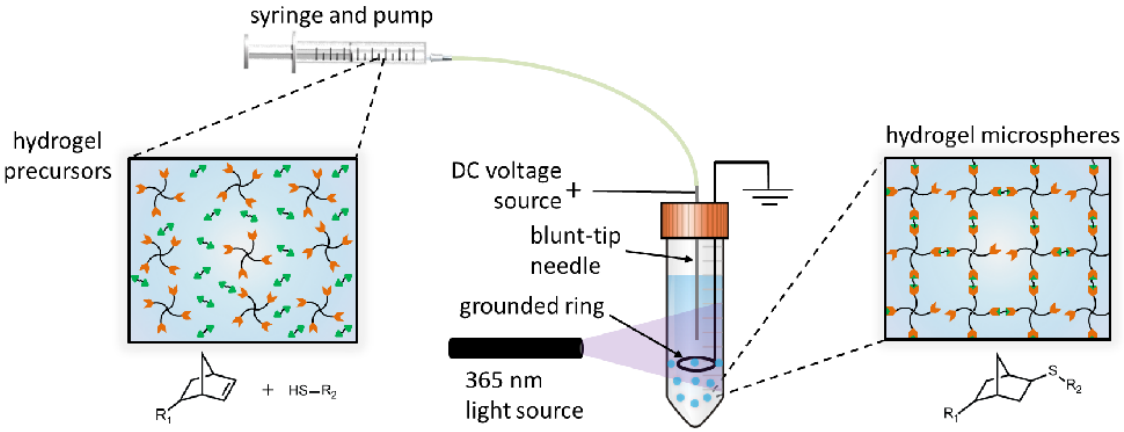

Figure II-6. Schematic of the submerged electrospraying setup for PEG thiol-ene microgel synthesis. Reprinted with permission from Xin *et al.*, 2018, *Advanced Healthcare Materials*, 7 (11), 1800160, John Wiley and Sons.

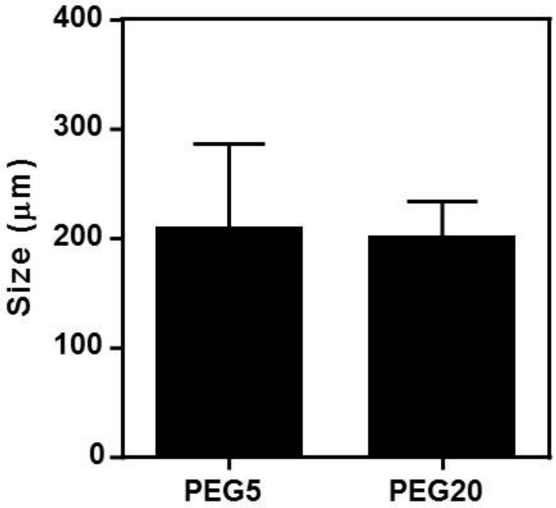

Figure II-7. Average size of PEG5 and PEG20 electrosprayed microgels evaluated by light microscopy. N = 30 microgels where analyzed for each group. Reprinted with permission from Xin *et al.*, 2018, *Advanced Healthcare Materials*, 7 (11), 1800160, John Wiley and Sons.

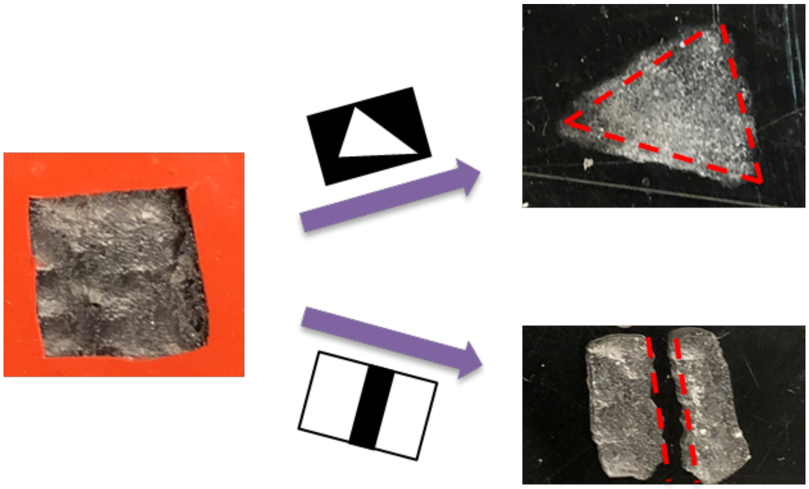

Figure II-8. Simple shaped photomask patterning of microgel assembly showing the spatiotemporal control of thiol-ene chemistry. Microgels were placed in a 1 cm × 1 cm mold and the photomasks were placed on top of the mold before UV irradiation. The dimension of the triangle was 0.9 cm × 0.6 cm and the diameter of the channel was 0.2 cm. Reprinted with permission from Xin *et al.*, 2018, *Advanced Healthcare Materials*, 7 (11), 1800160, John Wiley and Sons.

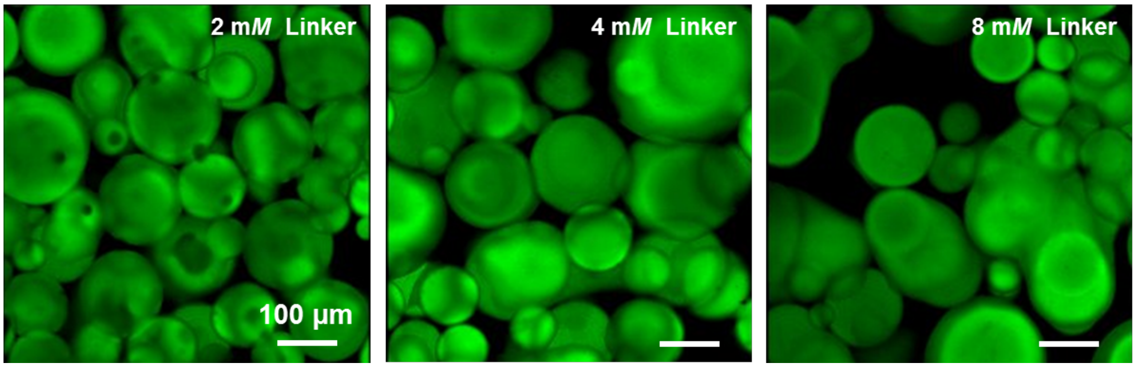

Figure II-9. Fluorescent Z-stack images of PEG5 scaffolds assembled using varying linker concentrations. Reprinted with permission from Xin *et al.*, 2018, *Advanced Healthcare Materials*, 7 (11), 1800160, John Wiley and Sons.

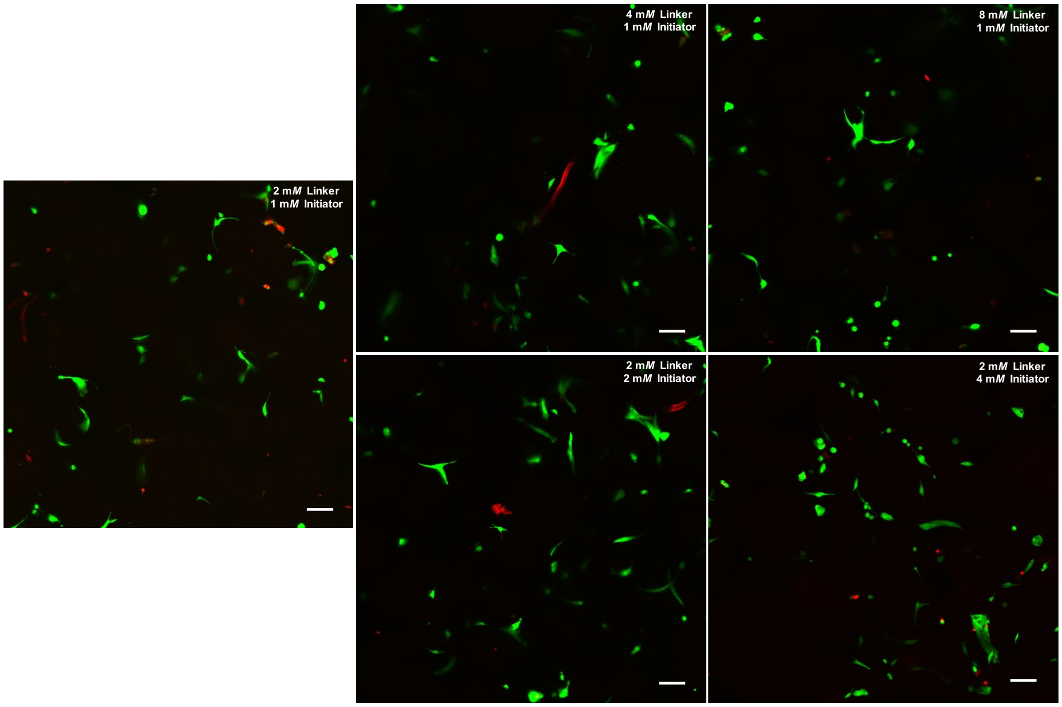

Figure II-10. Maximum intensity Z-projection of Live/Dead staining of hMSCs cultured within PEG5 scaffolds after 24h with varying PEG-DT linker and LAP photoinitiator concentrations. Scale bars are 100 µm. Reprinted with permission from Xin *et al.*, 2018, *Advanced Healthcare Materials*, 7 (11), 1800160, John Wiley and Sons.

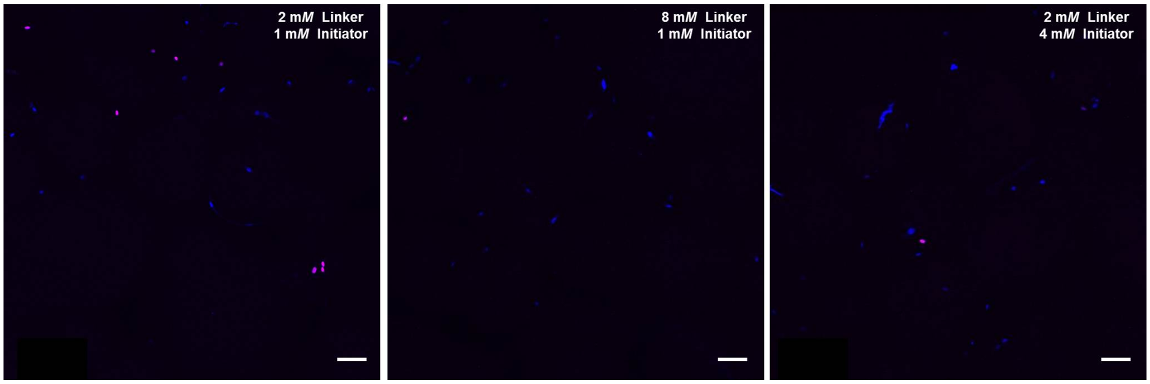

Figure II-11. Maximum intensity Z-projection of representative images of EdU staining of hMSCs within PEG5 scaffolds for 24h with varying PEG-DT linker and LAP photoinitiator concentrations. Reprinted with permission from Xin *et al.*, 2018, *Advanced Healthcare Materials*, 7 (11), 1800160, John Wiley and Sons.

CHAPTER III

INTERPLAY BETWEEN DEGRADABILITY AND INTEGRIN SIGNALING WITHIN PEG MICROPOROUS ANNEALED PARTICLE HYDROGELS ON HMSC FUNCTION AND BONE HEALING OUTCOMES*

Overview

MAP hydrogels are promising materials for delivering therapeutic cells. It has previously been shown that spreading and mechanosensing activation of hMSCs incorporated in these materials can be modulated by tuning the modulus of the microgel particle building blocks. However, the effects of degradability and functionalization with different integrin-binding peptides on cellular responses has not been explored. In this work, RGDS functionalized and enzymatically degradable PEG microgels were annealed into MAP hydrogels via thiol-ene click chemistry and photopolymerization. During cell-mediated degradation, the microgel surfaces were remodeled to wrinkles or ridges, but the scaffold integrity was maintained. Moreover, cell spreading, proliferation, and secretion of extracellular proteins were significantly enhanced in faster MMP degrading (KCGPQGIWGQCK) MAP hydrogels compared to non-degradable controls after 8 days of culture. We subsequently evaluated paracrine activity by hMSCs seeded in the MAP hydrogels functionalized with either RGDS or c(RRETAWA), which is

---

*Part of this chapter is reprinted with permission from “Interplay Between Degradability and Integrin Signaling on Mesenchymal Stem Cell Function within Poly(ethylene glycol) Based Microporous Annealed Particle Hydrogels” by Xin *et al.*, 2019, *Acta Biomaterialia*, DOI: https://doi.org/10.1016/j.actbio.2019.11.009, Copyright 2019 by Elsevier.

specific for α5β1 integrins, and evaluated the interplay between degradability and integrin-mediated signaling. Importantly, c(RRETAWA) functionalization upregulated secretion of BMP-2 overall and on a per cell basis, but this effect was critically dependent on microgel degradability. In contrast, RGDS functionalization led to higher overall VEGF secretion in degradable scaffolds due to the high cell number. These results demonstrate that integrin-binding peptides can modulate hMSC behavior in PEG-based MAP hydrogels, but the results strongly depend on the susceptibility of the microgel building blocks to cell-mediated matrix remodeling. This relationship should be considered in future studies aiming to further develop these materials for stem cell delivery and tissue engineering applications.

Introduction

Efficacious stem cell therapies for tissue engineering and regenerative medicine require a biomaterial carrier to improve stem cell retention in degenerated sites and orchestrate tissue repair.[7, 41, 93] Understanding cell-material interactions is critical for designing effective stem cell delivery systems that promote specific cell behaviors, such as differentiation and paracrine secretion.[4, 14] In general, it is appreciated that the biochemical and biophysical cues presented by biomaterials (*i.e.*, bioactive molecules, topography, and substrate stiffness) can affect cell spreading, proliferation, differentiation, and cytokine secretion and, thus, should be considered in designing stem cell delivery systems.[30, 69, 94-96] However, the interplay between these cues can be complex and must also be considered.

Hydrogels have been a focal point in the field due to their ability to encapsulate stem cells and provide them with an ECM like microenvironment.[7, 97] Myriad hydrogel platforms spanning natural and synthetic polymers and using a number of crosslinking strategies have been developed and reported. However, most work on hydrogels for stem cell delivery has focused on methods involving cell encapsulation within a nanoporous mesh, and recent research suggests that the isolated and restrictive nature of this microenvironment significantly alters cellular behavior.[24, 40, 88] For example, Caliari *et al.* reported that human mesenchymal stem cells (hMSCs) encapsulated within 3D nanoporous hydrogels exhibit decreased spreading and decreased YAP nuclear localization as stiffness increases, which is opposite to the trends seen in 2D cultures.[24] These effects have been attributed to the nanoporous nature of the hydrogels, since stiffer hydrogels constitute more restrictive microenvironments to encapsulated cells. However, the effects are not limited to cell spreading and mechanosensing, as Qazi *et al.* found that when rat MSCs were encapsulated in nanoporous hydrogels the lack of cell-cell interactions resulted in decreased paracrine secretion, which could influence tissue regeneration outcomes.[98]

Scaffolds assembled from hydrogel microspheres, or microgels, have recently emerged as promising alternative platform to nanoporous hydrogels for stem cell delivery. In general, these materials are constructed by covalently linking microgels together (referred to as annealing) either via complementary functional groups or through the addition of bi-functional linker.[99] They can be injected into tissue defects non-invasively and *in situ* linked to form scaffolds that are inherently microporous with excellent pore interconnectivity. The average size of microgels typically ranges from 50-250 µm, which creates pores with a few tens of microns in size. Thus, these materials have been termed microporous annealed particle or MAP hydrogels. Importantly, cells can be incorporated during microgel annealing into MAP hydrogels and, in contrast to conventional hydrogels, cells are incorporated in the micropores between the spherical microgels rather than embedded in a nanoporous polymer mesh. Several recent studies have shown that cell spreading is superior in these microgel-based scaffolds compared to cells encapsulated in conventional nanoporous hydrogels.[63-66, 100-102] In addition, because cells in MAP hydrogels interact with microgel surfaces and are not encapsulated, these materials provide a unique opportunity to leverage the rich body of knowledge regarding cell behavior in 2D environments to direct cellular behavior within these 3D scaffolds. Our previous work on PEG based MAP hydrogels annealed via thiol-ene click chemistry was the first to demonstrate this possibility, as we showed that hMSCs exhibit increased nuclear localization of YAP in MAP hydrogels made from stiffer microgels, similar to what has been observed in 2D cultures.[101]

To build on our prior work and develop materials that could be useful for hMSC delivery and bone tissue engineering, we are interested in understanding how the presentation of different integrin-binding peptides to hMSCs affects their behavior in PEG based MAP hydrogels.[103, 104] We are specifically interested in comparing the effects of a c(RRETAWA) peptide, which targets α5β1 integrins, to the widely used RGDS motif that binds to many different integrins. c(RRETAWA) was originally identified from a heptapeptide phage display library for α5β1 specific targeting, and it was subsequently found to be effective in inducing hMSC osteogenic differentiation when added solubly.[105-107] The osteoinductive mechanism has been attributed to the upregulated PI3K/Wnt/β-catenin signaling by c(RRETAWA)-induced α5β1 integrin priming.[108] Importantly, Gandavarapu *et al.* reported that 2D PEG hydrogels functionalized with c(RRETAWA) induced hMSC osteogenic differentiation without the addition of soluble osteoinductive factors,[109] providing further motivation for us to study c(RRETAWA) in MAP hydrogels. However, because the porosity of MAP hydrogels is relatively low (reported values range from 10-35 %),[64, 65, 101] we expected that the potential for cells to remodel their microenvironment might also be critical.

The objective of this study was to characterize hMSC growth in PEG-based MAP hydrogels and investigate the interplay between integrin-binding peptides and microgel degradability on hMSC behavior. To render the materials degradable, we synthesized enzymatically degradable PEG-peptide microgels using well established matrix metalloproteinase cleavable peptides. We then studied the effects of cell-mediated degradation on hMSC spreading, proliferation, and secretion of ECM in RGDS functionalized MAP hydrogels. The effects of cell-mediated degradation were also studied by characterizing the bulk integrity of the MAP hydrogel scaffolds as well as the surface morphology of the microgels. Similar experiments were performed for scaffolds functionalized with c(RRETAWA) rather than RGDS. Finally, we evaluated the interplay between degradability and integrin-binding via RGDS or c(RRETAWA) for modulating hMSC paracrine activity in MAP hydrogel scaffolds.

Materials and Methods

Materials

Tetrafunctional PEG-Nb macromers (5 kDa) were synthesized from PEG-hydroxyl precursors (JenKem Technology) via esterification with 5-norbornene-2-carboxylic acid (Alfa Aesar) and diisopropyl carbodiimide (Alfa Aesar) activation, as previously described by Jivan *et al.*.[79] The polymers were dialyzed against deionized water prior to use, and the percent functionalization was higher than 95% via ^{1}H NMR spectroscopy analysis. PEG-DT (3,400 Da) crosslinker was purchased from Laysan Bio.. The cell adhesive peptide CGRGDS, enzymatically degradable peptide crosslinker KCGPQGIWGQCK, and CGPQGPAGQGCR were prepared via microwave-assisted standard Fmoc solid phase peptide synthesis methods. Peptide identity was verified by matrix-assisted laser desorption/ionization time of flight mass spectrometry analysis. The α5β1 integrin targeting peptide c(RRETAWA) was purchased from AAPPtec through an on-resin cyclization reaction of Ac-CAhxK(Alloc)RRETAWAE(ODmab), as previously described by Gandavarapu *et al*..[109] LAP photoiniator was synthesized following the methods of Fairbanks *et al.* without modification and was verified by ^{1}H NMR spectroscopy and electrospray ionization mass spectrometry prior to use.[77]

Fabrication of MAP Hydrogels

PEG microgels were fabricated by submerged electrospraying and thiol-ene click chemistry, as described previously.[110] Briefly, PEG-Nb, dithiol crosslinker, LAP, and cell adhesive peptide were mixed off-stoichiometrically to achieve a [SH]:[ene] ratio of

0.75:1. The working concentrations of PEG-Nb, di-thiol crosslinker, LAP, and cell adhesive peptide were 10 wt% (resulting in 73 m*M* norbornene groups), 26.87 m*M*, 1 m*M*, and 2 m*M*, respectively. PEG-DT, CGPQGPAGQGCR, and KCGPQGIWGQCK were used to prepare microgels with varying degradability (termed non-deg, slow-deg, and fast-deg, respectively).[111, 112] These precursor solutions were electrosprayed under voltage of 4 kV, flow rate of 12 mL/h, and needle-to-grounded ring distance of 16 mm. The electrosprayed droplets were then collected in a light mineral oil bath with Span 80 (0.5 wt%) and photopolymerized using UV light (365 nm, 60 mW/cm^2, 7 min, Lumen Dynamics Omnicure S2000 Series). The resulting microgels were centrifuged, washed one time with 30% ethanol, and then washed five times with phosphate buffered saline to remove mineral oil and surfactant. The microgels were swollen in 1X phosphate buffered saline at 4 °C overnight to reach equilibrium before use. After swelling, the microgels were imaged using light microscopy (Eclipse, TE2000-S, Nikon), and the size of microgels was measured from the images using Image-J software ($n \geqslant 150$).

Next, these microgels were packed in a 6 mm diameter, 50 μL rubbery circular mold. Then, 8 μL of a solution containing PEG-DT and LAP in PBS was added to reach final concentration 2 m*M* and 1 m*M*, respectively, and the microgels were assembled into scaffolds by forming linkages between norbornene groups on the microgel surfaces via a secondary thiol-ene UV polymerization (Figure III-1a, 365 nm, 10 mW/cm^2, 3 min).

Characterization of MAP Hydrogels

The electrosprayed microgels were labeled with Alexa Fluor 488 N-hydroxysuccinimide ester dye (Invitrogen) and imaged using confocal microscopy (FV1000, Olympus). The size of microgels was measured from the confocal images using Image-J software ($n \geq 50$). To characterize the degradability of MAP scaffolds, slow-deg and fast-deg scaffolds were soaked in 0.2 mg/mL collagenase B (Sigma) solution at 37 °C. The remaining scaffolds were weighed every 5 minutes for the first 50 minutes and every 20 minutes thereafter. In addition, the storage moduli of the MAP scaffolds after 33% and 67% mass loss were measured by oscillatory shear rheology (Physica MCR 301, Anton Paar) at 1% strain and 1 rad/s and compared to non-degraded scaffolds.

hMSC Culture and Seeding

Bone marrow derived hMSCs were acquired from the Institute of Regenerative Medicine at Texas A&M University. The hMSC identity was confirmed by immunophenotypic analysis on positive expression of CD29, CD44, CD146, CD166, HLA ABC, and negative expression of CD11b, CD79a.[113] hMSC culture media was α-Minimal essential medium (Gibco) supplemented with 20% v/v fetal bovine serum (FBS, Atlanta Biologicals), 2 m*M* GlutaMAX (Gibco), 50 U/mL penicillin (Gibco), and 50 µg/mL streptomycin (Gibco) at 5% CO2 and 37 °C in a humidified environment. Passage 3 cells, where 1 passage is equivalent to 8-9 population doublings, were used in this work. For hMSC encapsulation in MAP scaffolds, single-cell suspensions of hMSCs

(5 µL) were mixed with microgels in the mold at a density of 250,000 cells per 50 µL scaffold along with the additional PEG-DT and LAP, and microgel assembly was performed by UV polymerization (365 nm, 10 mW/cm^2, 3 min).

Cell Spreading and Proliferation

Samples were fixed after the desired culture time using 4% formaldehyde for 15 min at room temperature. Cytoskeletal staining was performed to determine the impact of scaffold degradability on cell spreading using rhodamine phalloidin (1:40, Invitrogen), and cell nuclei were stained with DAPI (1:1000, Jackson ImmunoResearch). All the samples were imaged in a glass-bottomed petri dish (MarTek) by confocal microscopy (FV1000, Olympus).

At least three z-stack images were taken in different regions of each scaffold and each z-stack had a depth of 200 µm depth and 45 slices. The images were analyzed using ImageJ software (NIH). For cell proliferation quantification, the 3D Objects Counter plugin was used to count the number of nuclei based on DAPI staining. The Voxel Counter plugin was used to measure the total cell volume in a z-stack based on phalloidin staining after thresholding. The average cell volume was then calculated by dividing the total cell volume by cell number.

Integrin Blocking Assay

hMSCs were incubated with antibodies against α5 (Santa Cruz Biotechnology), αVβ3 (Santa Cruz Biotechnology) integrins or Isotype control (IgG, 5 µg/mL, Sigma) in serum-free media for 30 min. Then they were seeded within RGDS and c(RRETAWA)-functionalized MAP hydrogels in culture media without serum and allowed to attach to the microgels for 12 h. The hydrogels were washed with PBS four times to remove unattached hMSCs and fixed using 4% formaldehyde for 15 min at room temperature. Cytoskeletal staining was performed using rhodamine phalloidin (1:40, Invitrogen), and cell nuclei were stained with DAPI (1:1000, Jackson ImmunoResearch). Samples were imaged using confocal microscopy (FV1000, Olympus), and the number of attached cells was counted based on DAPI staining by 3D Objects Counter plugin in ImageJ software.

Characterization after Cell-mediation Degradation

The diameter of MAP scaffolds before and after cell culture was measured by a caliper. To quantify the porosity of these scaffolds, high molecular weight tetramethylrhodamine isothiocyanate-labelled dextran (155 kDa, Sigma) was diffused into the MAP scaffolds and imaged by confocal microscopy (FV1000, Olympus). The overall porosity was calculated using ImageJ software (NIH) and the Voxel Counter plugin after thresholding. The storage moduli of fast-deg MAP scaffolds before and after cell culture were measured by oscillatory shear rheology (Physica MCR 301, Anton Paar) at 1% strain and 1 rad/s. To visualize the surface morphology after cell-mediated matrix remodeling, samples were collected after cell culture and decellularized by rinsing in 1X RIPA buffer (Thermo Scientific) overnight. The surface morphology was then imaged using ESEM (Tescan Vega 3) in wet mode with a backscattering detector at 1 °C and 600 Pa.

Extracellular Protein Deposition

Proteins produced by cells were labelled based on fluorescent tagging of azidohomoalanine, as previously reported.[114] hMSC-laden MAP scaffolds were cultured in L-methionine, L-cystine and L-glutamine free high-glucose Dulbecco's Modified Eagle's Medium (Sigma) supplemented with 0.1 m*M* azidohomoalanine (Invitrogen), 20% FBS, 0.2 m*M* cystine (Sigma), 100 µg/mL sodium pyruvate (Invitrogen), 50 µg/mL ascorbate 2-phosphate, 2 m*M* GlutaMAX, 50 U/mL penicillin, and 50 µg/mL streptomycin. After the desired culture time, newly synthesized proteins were labeled with 25 µ*M* dibenzocyclooctyne-PEG4-fluor 545 (Sigma) for 30 minutes and cell membranes were stained with the CellMask green plasma membrane stain (1:1000, Invitrogen). The samples were then fixed with 4% formaldehyde for 15 min at room temperature. Confocal microscopy (FV1000, Olympus) was used to image these samples at 20X and at least three z-stack images (100 µm depth with 45 slices) were taken in different regions of each scaffold. The protein channel was subtracted from cell membrane channel using image calculator in ImageJ to obtain only the extracellular proteins. The total extracellular protein volume was then calculated using the Voxel Counter plugin in ImageJ.

For immunostaining with collagen type I and fibronectin, the samples were then fixed with 4% formaldehyde for 15 min at room temperature after 8 days of culture and incubated in blocking buffer containing 3% normal goat serum (Gibco) and 0.3% Triton-X 100 (Thermo Scientific) for 2 h at room temperature. Evaluation of collagen type I and fibronectin was performed by immunohistochemistry utilizing antibodies against collagen type I (1:500, Abcam) and fibronectin (1:100, Santa Cruz Biotechnology). Fluorescent secondary antibodies Alexa Fluor-488/647 IgG H&L (1:200, Abcam) were used to label the location of primary antibodies. Samples were then counter stained with DAPI (1:1000, Jackson ImmunoResearch). Samples were imaged using confocal microscopy (FV1000, Olympus), and the volumes of collagen type I and fibronectin production were calculated using the Voxel Counter plugin in ImageJ.

Quantification of Secretory Activity

Enzyme-linked immunosorbent assay kits to evaluate the effect of scaffold degradability on stimulation of hMSC paracrine secretion by different integrin-binding peptides. Specifically, the angiogenic marker VEGF and the osteogenic markers BMP2 and OPG were tested. In these experiments, hMSCs were cultured in culture media supplemented with 5 m*M* β-glycerophosphate and 50 µg/mL ascorbic acid. Media were collected after the desired culture time and protein concentrations were quantified following the commercial kit protocols (R&D Systems). The scaffolds were also lysed by 1X RIPA buffer, and the double stranded DNA content was determined by the Picogreen assay (Invitrogen) to normalize VEGF, BMP-2, and OPG expression.

Bone Healing in Mouse Femoral Defect Model

The bone healing outcomes of degradable MAP hydrogels were evaluated in a mouse femoral defect model, as reported previously.[115] All the animal studies were approved by the Institutional Animal Care and Use Committee of Texas A&M University. Nu/Nu nude mice (2 months old) were purchased from Charles River. A 3 mm defect was created in the femur and stabilized by a 9 mm long medullary pin with a 3 mm collar. 50 μL degradable microgels with both RGDS and c(RRETAWA)-functionalization were injected with PEG-DT and LAP into the femoral defect. An *in situ* crosslinked step was performed by UV irradiation (365 nm, 10 mW/cm^2, 3 min). For cell delivery groups, cell suspensions were injected together with microgels. The mice were kept for 4 weeks before sacrifice. The volume of new bone formation was quantified based on the scans from micro-CT (Bruker).

Statistical Analysis

All experiments were conducted with at least three independent replicates. Results are reported as the mean ± standard deviation. Two-way ANOVA followed by Tukey's multiple comparisons test was used to determine significant differences between groups. Significance is indicated by $^{*}p < 0.05$, $^{**}p < 0.01$, and $^{***}p < 0.0001$, respectively.

Results

MAP Hydrogel Characterization and Degradation

PEG-based MAP hydrogels were synthesized similar to what we previously described.[101] The degradability of the MAP hydrogel scaffolds was tuned by introducing different dithiol crosslinkers during microgel fabrication (Figure III-1b). The size of non-degradable microgels and degradable microgels were 266 ± 89 μm and 192 ± 90 μm, respectively (Figure III-10). Linking the microgels together with a secondary thiol-ene reaction resulted in a microporous internal structure despite the high polydispersity of the microgels (Figure III-1c). The linkages between the microgels were non-degradable PEG-DT to ensure that scaffold integrity was maintained during cell-mediated degradation. To evaluate the degradation rates, an accelerated degradation study was performed by immersing the MAP hydrogels into collagenase B solutions at 37 °C. The results confirmed that MAP hydrogels constructed from microgels with the tryptophan-containing peptide crosslinker (fast-deg group) degraded faster than those with proline-containing peptide crosslinker (slow-deg group; Figure III-1d), which was comparable to previous investigations,[111, 116] whereas MAP hydrogels from microgels with PEG-DT crosslinker (non-deg group) did not degrade.. In addition, the shear storage moduli of the MAP hydrogels were characterized during degradation (Figure III-1e). When they were degraded to the point of ~33% mass loss, the storage modulus was reduced by approximately ~90% in both the slow-deg and fast-deg groups. The modulus was further reduced after ~67% mass loss, and the MAP hydrogel scaffolds could be completely degraded over time.

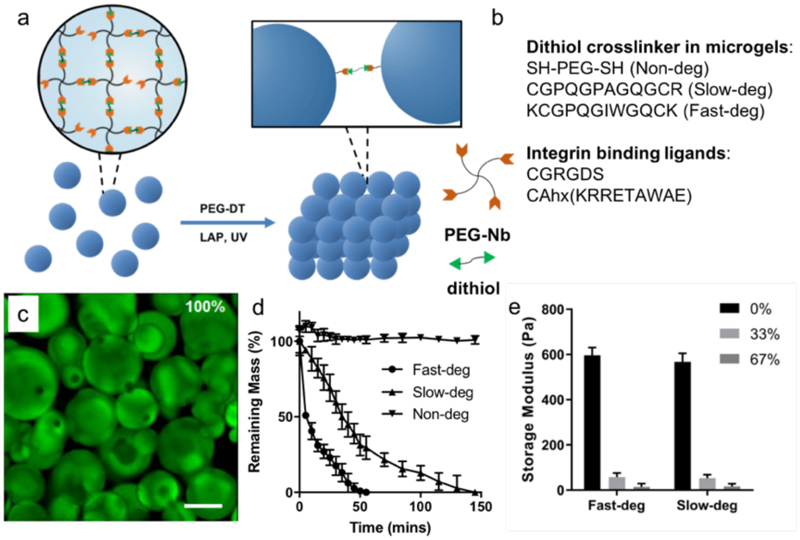

Figure III-1. Design and characterization of MAP hydrogels with varying degradability. a) A schematic of MAP hydrogels assembled from off-stoichiometric PEG microgels via a secondary thiol-ene photopolymerization. b) Peptide sequences designed as crosslinkers and cell-adhesive ligands to achieve varying degradability and integrin binding. c) A representative Z-stack projection image of MAP hydrogels labeled with Alexa Fluor 488-succinimidyl ester illustrating the internal porous structure. Scale bar is 100 µm. d) Degradation curves of non-deg, slow-deg and fast-deg MAP hydrogels in a 0.2 mg/mL collagenase solution at 37 °C. e) Storage modulus of slow-deg and fast deg MAP hydrogels after degradation with 0%, 33%, and 67% mass loss. Reprinted with permission from Xin *et al.*, 2019, *Acta Biomaterialia*, DOI: https://doi.org/10.1016/j.actbio.2019.11.009, Elsevier.

Characterization of hMSC Growth in RDGS and c(RRETAWA) Functionalized MAP Hydrogels

250,000 hMSCs were mixed with the microgels and incorporated into 50 µL MAP hydrogels during annealing via the secondary thiol-ene crosslinking reaction. Thus, they were located in the scaffold pores and were able to attach and spread on the microgel surfaces. We first evaluated hMSC spreading and proliferation in RGDS-functionalized MAP hydrogel scaffolds (Figure III-2). Similar to previous results in the literature, hMSCs were able to spread around the microgels after 2 days due to the permissive environment in the scaffolds.[63, 101] However, the numbers of cells in both the slow-deg and fast-deg scaffolds were higher than in non-deg group after 2 days, indicating that cell-mediated degradation allowed for proliferation. This trend became more obvious after 8 days of culture, as further proliferation and an approximately 4-fold increase in cell number was observed in the fast-deg group. However, there was no significant increase in cell number in both the non-deg and slow-deg groups. In addition, in the slow-deg and fast-deg groups the cells were aggregated and formed a 3D cellular network, whereas they were isolated in the non-deg control group. Acellular spherical regions were no longer visible in the fast-deg 8-day samples, suggesting that cell-mediated degradation altered microgel morphology in this group.

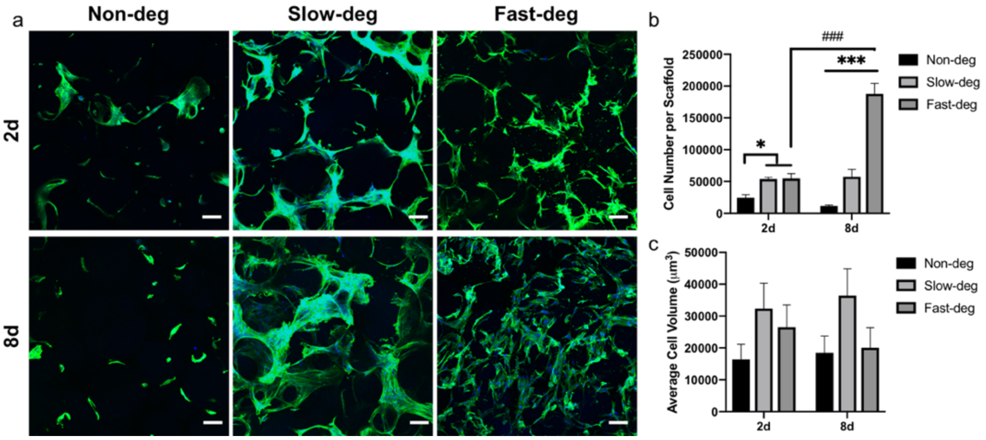

Figure III-2. The effect of degradability on hMSC spreading and proliferation in c(RRETAWA)-functionalized MAP hydrogels. a) Maximum intensity Z-projection of cytoskeleton staining of hMSCs cultured in MAP hydrogels after 2 and 8 days. Green represents F-actin and blue represents nuclei. Scale bars are 100 μm. b) Quantification of cell number. c) Quantification of cell volume. * comparison factor: degradability; # comparison factor: time. * indicates $p < 0.05$, *** and ### indicate $p < 0.0001$, Two-way ANOVA and Tukey's multiple comparisons test. Reprinted with permission from Xin *et al.*, 2019, *Acta Biomaterialia*, DOI: https://doi.org/10.1016/j.actbio.2019.11.009, Elsevier.

We also studied hMSC attachment, spreading, and proliferation in c(RRETAWA)-presenting MAP hydrogel scaffolds (Figure III-3). Abundant surface expression of α5 integrins by hMSCs has previously been reported,[117] and we evaluated the integrin binding specificity of c(RRETAWA) with an integrin blocking experiment (Figure III-11). Importantly, when α5 integrins were blocked with an antibody, the number of cells in c(RRETAWA)-functionalized MAP hydrogels decreased by approximately 50%, whereas hMSCs were still able to attach normally within RGDS MAP hydrogels. These results are similar to those reported by Gandavarapu *et al.*,[109] although our decrease in attachment to c(RRETAWA) after α5 blocking was not as dramatic. This difference is likely due to the greater difficulty of removing unattached cells from MAP hydrogels compared to 2D hydrogel slabs. Next, we characterized cell spreading in c(RRETAWA) functionalized MAP hydrogels, which was observed to be reduced compared to RGDS-presenting MAP hydrogels in non-deg and fast-deg groups after 2 days (Figure III-12), likely because c(RRETAWA) binds only α5β1 integrins. Nevertheless, the hMSC spreading and proliferation trends with increasing degradability in c(RRETAWA) MAP hydrogels were similar to what was shown in RGDS scaffolds. While there were no significant differences between groups in cell number and volume after 2 days, the fast-deg scaffolds showed significantly higher cell number and volume after 8 days compared to non-deg and slow-deg groups. Interestingly, cells again only proliferated drastically from 2 to 8 days in the fast-deg scaffolds, similar to the results in the RGDS scaffolds. This result indicates that cell-mediated degradation is critical regardless of the integrin-binding peptide used.

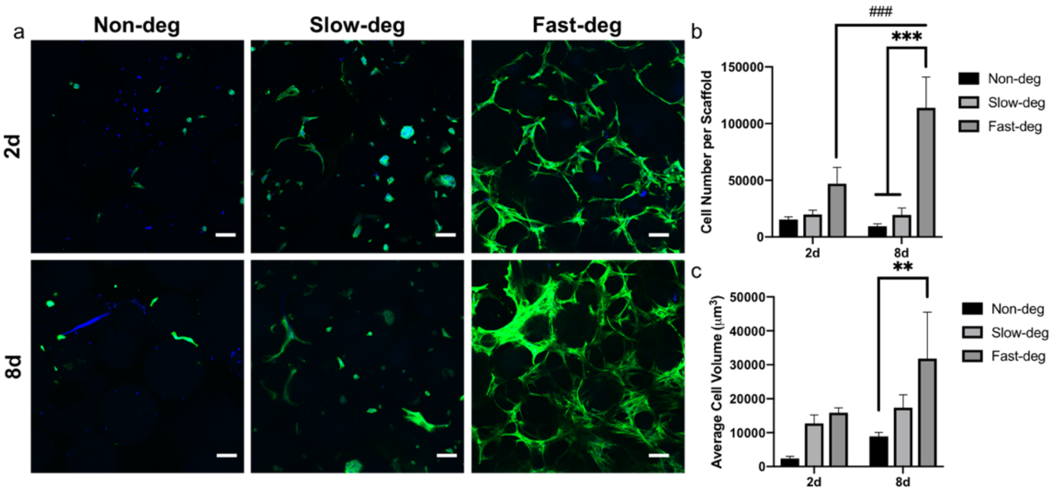

Figure III-3. The effect of degradability on hMSC spreading and proliferation in c(RRETAWA)-functionalized MAP hydrogels. a) Maximum intensity Z-projection of cytoskeleton staining of hMSCs cultured in MAP hydrogels after 2 and 8 days. Green represents F-actin and blue represents nuclei. Scale bars are 100 μm. b) Quantification of cell number. c) Quantification of cell volume. * comparison factor: degradability; # comparison factor: time. ** indicates $p < 0.01$, *** and ### indicate $p < 0.0001$, Two-way ANOVA and Tukey's multiple comparisons test. Reprinted with permission from Xin *et al.*, 2019, *Acta Biomaterialia*, DOI: https://doi.org/10.1016/j.actbio.2019.11.009, Elsevier.

Cell-mediated Matrix Remodeling in MAP Hydrogels

We further investigated the impact of degradability in RGDS-functionalized MAP hydrogels. First, to examine the extent of cell-mediated degradation in fast-deg MAP hydrogel scaffolds, we characterized bulk properties after cell culture and compared them to the non-deg control group (Figure III-4). The diameter and porosity of the scaffolds did not change significantly after 8 days of culture in either the fast-deg or non-deg groups (Figure III-4a and b), indicating cell-mediated degradation only occurred in a small portion of the materials. Furthermore, the storage moduli of the fast-deg scaffolds only dropped about ~30% after 8 days (Figure III-4c). Considering ~33% mass loss could result in ~90% drop of modulus (Figure III-1e), these results further confirmed that cell-mediated degradation of the MAP hydrogels was relatively limited after 8 days. Thus, these scaffolds could continue to play a supportive role to cells after long-term cell culture.

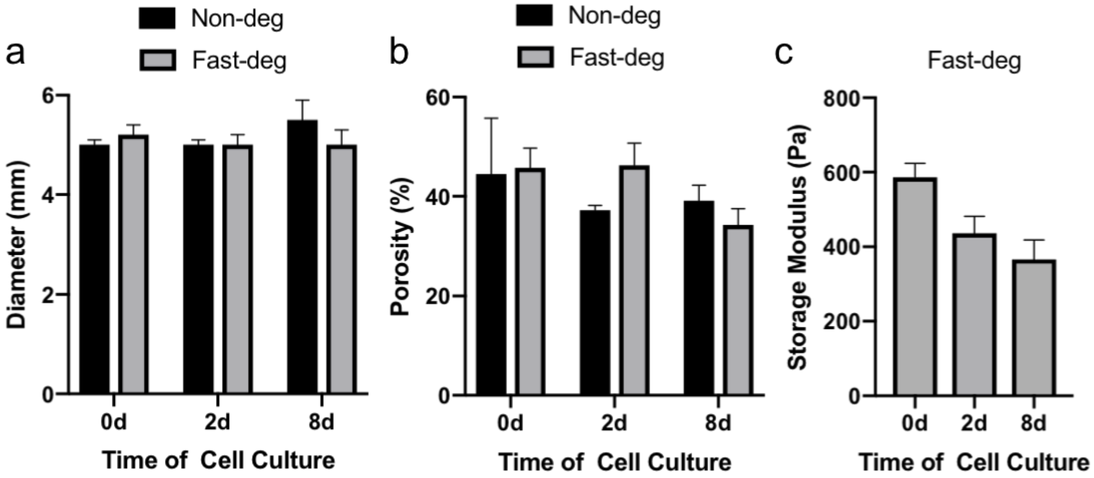

Figure III-4. Bulk properties of MAP hydrogels before and after cell-mediated degradation. a) Diameter and b) porosity of MAP hydrogels over cell culture. c) Storage modulus of fast-deg MAP scaffolds over cell culture. Reprinted with permission from Xin *et al.*, 2019, *Acta Biomaterialia*, DOI: https://doi.org/10.1016/j.actbio.2019.11.009, Elsevier.

Next, we investigated the surface morphology of the microgels after cell-mediated degradation using ESEM (Figure III-5). The microgel surfaces were smooth in the scaffolds prior to cell culture. Interestingly, fiber-like structures connecting microgels could be visualized, owing to the PEG-DT linkages between surface norbornene groups formed during the annealing process. After 8 days of cell culture, the MAP hydrogels were decellularized by washing in detergent. Non-deg scaffolds after cell culture maintained a smooth surface, although the linkages became less visible. In contrast, the surfaces of the fast-deg scaffolds appeared wrinkled after cell culture, indicating that cells were creating grooves as they remodeled their microenvironments to facilitate their spreading and proliferation. These results also indicated that cell-mediated matrix remodeling in the MAP scaffolds was limited to the microgel surfaces, again indicating that these scaffolds could continue to play a supportive role for cells despite cell-mediated degradation.

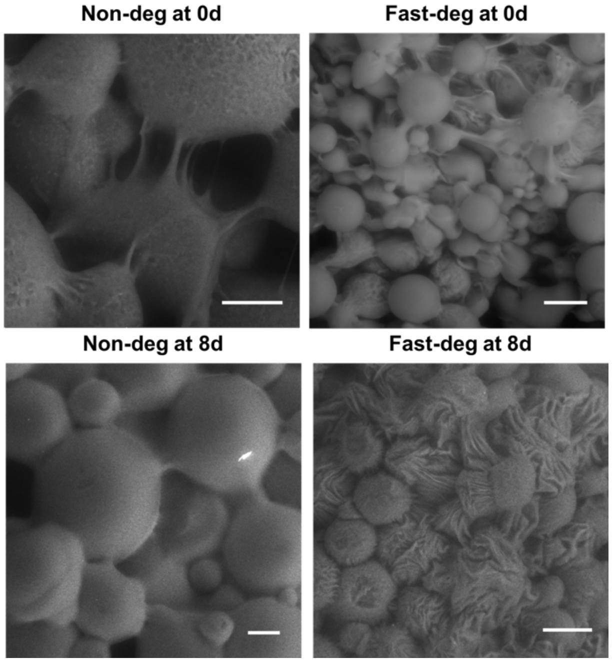

Figure III-5. ESEM images illustrating surface morphology of non-deg and fast-deg before and after cell-mediated matrix remodeling. Scale bars are 100 µm. Reprinted with permission from Xin *et al.*, 2019, *Acta Biomaterialia*, DOI: https://doi.org/10.1016/j.actbio.2019.11.009, Elsevier.

In addition to studying morphological changes to the microgels, we studied the total extracellular proteins secreted by the hMSCs in both non-deg and fast-deg RGDS and c(RRETAWA) functionalized MAP hydrogel scaffolds using a bio-orthogonal methionine analog labeling technique (Figure III-6). The extracellular proteins were identified by subtracting labelled proteins from cell membrane staining and quantified. The results showed that the amount of extracellular proteins synthesized after 2 days were similar for the non-deg and fast-deg groups (Figure III-13). However, after 8 days of culture extracellular protein deposition in the RGDS-presenting fast-deg scaffolds accounted for roughly 5% of the volume of the entire scaffold, and the amount of extracellular protein deposition was significantly higher compared to the non-deg scaffolds. These results correlate well with the hMSC spreading and proliferation data and indicate that, while microporosity alone can permit cellular spreading at early time points, cell-mediated degradation is critical over the longer term. Similar results of extracellular protein deposition as an effect of degradability were observed in c(RRETAWA)-functionalized MAP hydrogels, but the amount of proteins was significantly less compared to RGDS groups. While the majority of the extracellular proteins were ECM proteins, specific ECM proteins, including collagen type I and fibronectin, were also investigated to further reveal that hMSCs produced fibrous ECM within the pores of MAP hydrogels in fast-deg groups.

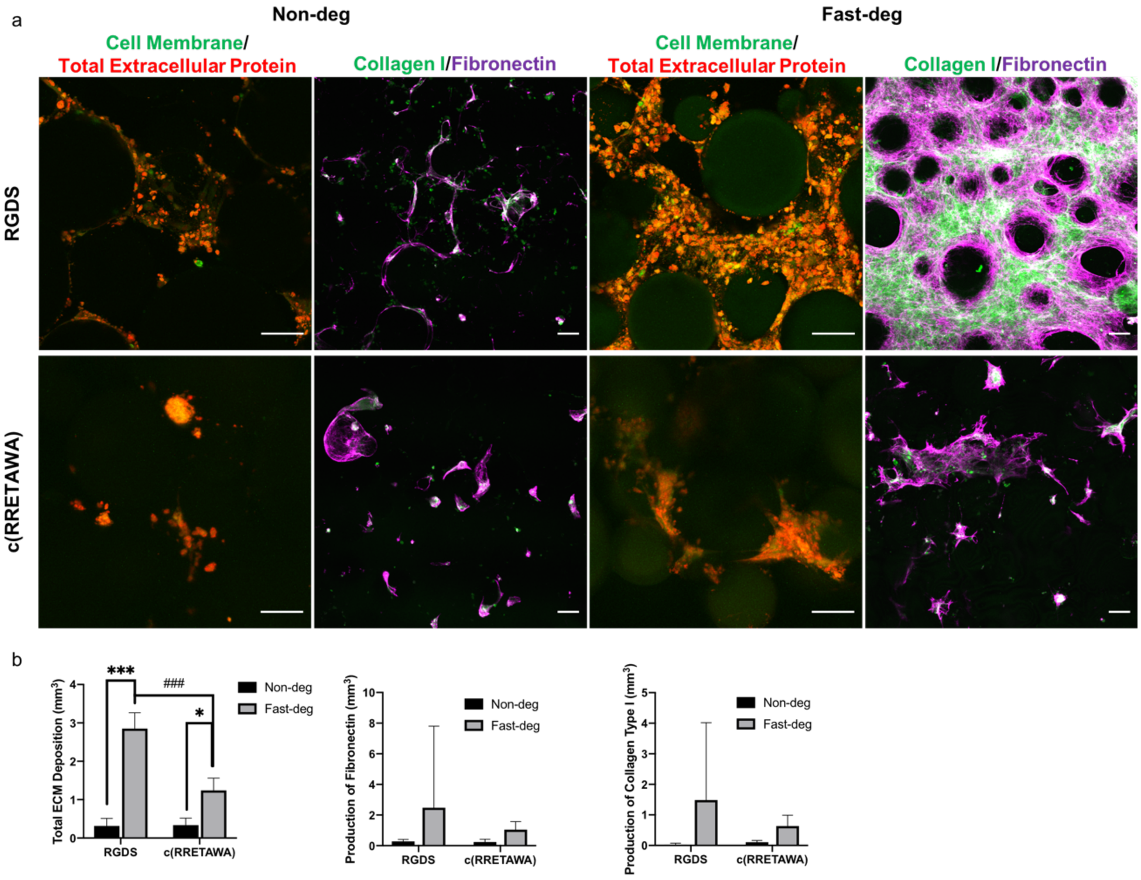

Figure III-6. The total extracellular proteins, collagen type I and fibronectin synthesized by hMSCs in MAP hydrogels with varying degradability and integrin-binding peptides after 8 days of culture. a) Z-projection images from confocal microscopy. Scale bars are 100 µm. b) Quantification of total ECM protein per 50 µL MAP hydrogels. * comparison factor: degradability; # comparison factor: integrin-binding peptide. * indicates $p < 0.05$, *** and ### indicate $p < 0.0001$, Two-way ANOVA by Tukey's multiple comparisons test. Reprinted with permission from Xin *et al.*, 2019, *Acta Biomaterialia*, DOI: https://doi.org/10.1016/j.actbio.2019.11.009, Elsevier.

hMSC Response to RGDS and c(RRETAWA) Functionalized MAP hydrogels

We studied the impact of cell-mediated degradation on the response of hMSCs to different integrin-binding peptides. We first examined the early osteogenic differentiation marker OPG in RGDS and c(RRETAWA) functionalized MAP hydrogel scaffolds. Importantly, the production of OPG normally peaks around 4 to 5 days during osteogenic differentiation in 2D cultures.[118, 119] In fast-deg scaffolds, OPG secretion peaked at 5 days as expected, while it did not peak until 8 days in the non-deg scaffolds (Figure III-7). However, there was no significant difference in OPG secretion level between RGDS and c(RRETAWA) functionalized groups.

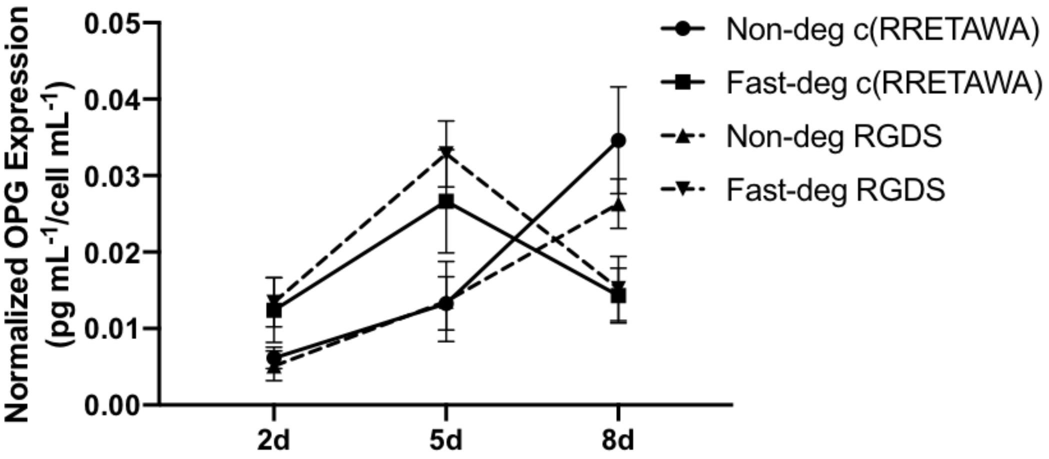

Figure III-7. hMSC expression of OPG in RGDS and c(RRETAWA)-functionalized MAP hydrogels with varying degradability after 2, 5, and 8 days of culture. Three-way ANOVA results: time ($p < 0.0001$), time×degradability ($p < 0.0001$), integrin-binding peptide×degradability ($p < 0.05$). Reprinted with permission from Xin *et al.*, 2019, *Acta Biomaterialia*, DOI: https://doi.org/10.1016/j.actbio.2019.11.009, Elsevier.

We also studied their effects on VEGF and BMP2 secretion at 8 days (Figure III-8). In addition to overall protein production, the data was also analyzed after normalization to dsDNA to account for proliferation and evaluate cellular changes. Overall VEGF expression was upregulated in fast-deg MAP hydrogels and was higher with RGDS. However, this result was attributed to the higher cell number, as there were no significant differences between groups after normalization. In contrast, overall and normalized BMP2 expression was significantly higher in c(RRETAWA) functionalized fast-deg scaffolds than in RGDS functionalized fast-deg scaffolds. This result agrees with prior work reporting that c(RRETAWA) induces hMSC osteogenic differentiation.[109] However, the non-deg scaffolds did not show this difference, highlighting the importance of degradability.

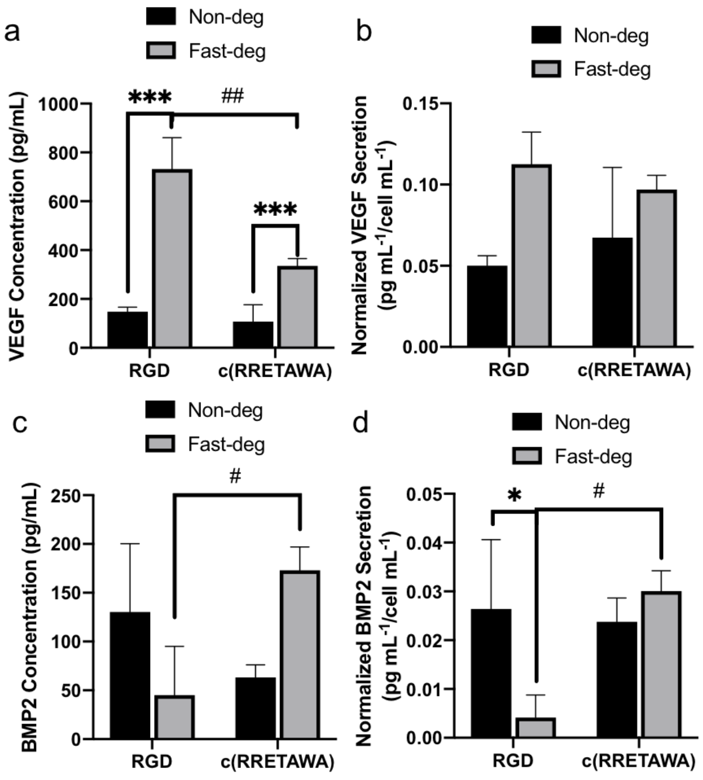

Figure III-8. hMSC secretion of a, b) VEGF and c, d) BMP2 in MAP hydrogels functionalized with RGDS and c(RRETAWA) and with varying degradability after 8 days of culture. Data presented are both before and after normalization. * comparison factor: degradability; # comparison factor: integrin-binding peptide. * and # indicate $p < 0.05$, ## indicates $p < 0.01$, *** indicates $p < 0.0001$, Two-way ANOVA by Tukey's multiple comparisons test. Reprinted with permission from Xin *et al.*, 2019, *Acta Biomaterialia*, DOI: https://doi.org/10.1016/j.actbio.2019.11.009, Elsevier.

In vivo Bone Healing

Figure III-9 presents the micro-CT scans and quantification of new bone formation after implanting degradable MAP hydrogels. Overall, there is no significant difference between all groups. But all these groups showed a significant increase in new bone formation compared to the no treatment control reported previously.[115] These results indicate the cells need more osteogenic stimulus in order to promote bone healing. However, it is promising that materials alone can significantly promote bone healing after 4 weeks, suggesting the cell infiltration from surrounding tissues is enhanced by the interconnected pore structure in MAP hydrogels, which may be further amplified by degradation.

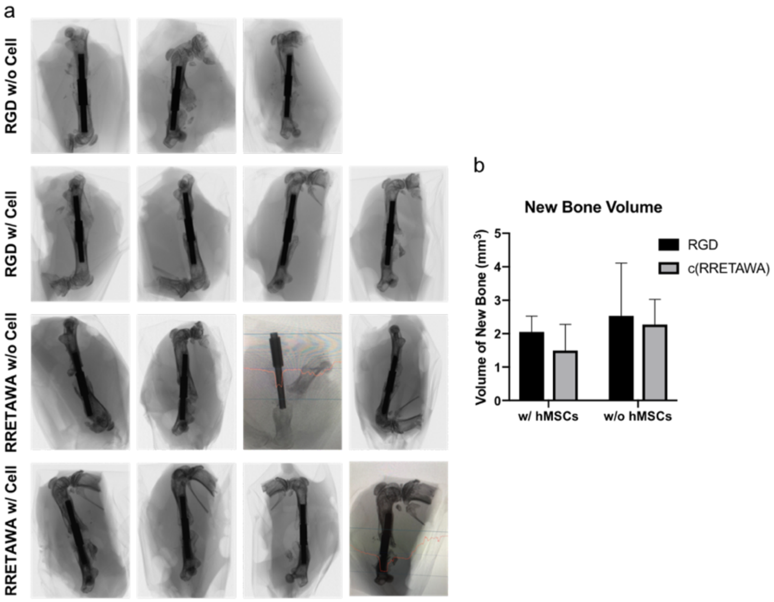

Figure III-9. a) Scanning images illustrating new bone formation from micro-CT. b) Quantification of the new bone volume. Two-way ANOVA by Tukey's multiple comparisons test.

Discussion

MAP hydrogels are an emerging class of biomaterials that is receiving considerable attention for tissue repair and regeneration. The growing interest in MAP hydrogels stems from recent work demonstrating enhanced *in vivo* tissue regeneration compared to conventional nanoporous hydrogels.[63, 76] These materials are also an attractive stem cell delivery platform for tissue engineering.[120] Importantly, cells incorporated into MAP hydrogels during microgel annealing are able to spread and proliferate without requiring degradation of the surrounding matrix, as we previously showed.[101] However, the pore volume initially available to the cells is relatively low. Evidence suggests that larger pore spaces result in improved cell spreading and formation of 3D cellular network.[65, 101] Thus, there is a need for degradable designs that allow for cell-mediated matrix remodeling.

To confer degradability, we fabricated MAP scaffolds from PEG-based microgels that were crosslinked with enzymatically degradable peptides. Two different peptides with varying susceptibility to enzymatic degradability (slow-deg and fast-deg) were used and compared to non-degradable controls (non-deg). MAP hydrogels constructed from these microgels exhibited the expected trends in degradability when immersed in collagenase (Figure III-1). However, even the fast-deg group degraded relatively slowly in experiments with hMSCs and could likely play a supportive role for cells for a long-term period. This result was attributed to cell-mediated degradation only occuring on the microgel surfaces, leading to a low extent of degradation (Figure III-4 and 5).

By culturing hMSCs in these MAP hydrogel scaffolds, we uncovered a crucial role for cell-mediated degradation in improving cell spreading and proliferation. There were negligible differences after 2 days of culture, as the inherent microporosity of the MAP hydrogels permitted initial cell spreading. However, hMSCs cultured in the fast-deg MAP hydrogel scaffolds in particular proliferated significantly from 2 to 8 days using both RGD and c(RRETAWA) integrin binding ligands, and the average cell volume did not drop (Figure III-2 and 3). This result indicates that the pore space between microgels quickly becomes saturated for cell growth and cell-mediated degradation is needed to remodel surrounding matrix. Degradation may also increase the connectivity of the porous network by making larger openings between the pores.

Importantly, the effects of degradability were not limited to cell growth, as two notable changes to the cellular microenvironment were apparent when we compared fast-deg and non-deg MAP hydrogel scaffolds. First, topographical changes were observed, as the ESEM images revealed wrinkle structures on the surfaces of the microgels after cell-mediated degradation (Figure III-5). This change could be important, as Guvendiren *et al.* previously manufactured various patterns of surface wrinkles on poly(2-hydroxyethyl methacrylate) hydrogels and found that hMSCs cultured on lamellar patterned surfaces exhibited enhanced spreading and osteogenic differentiation compared to flat or hexagonal patterns.[121] Second, the hMSCs secreted more extracellular proteins in fast-deg MAP hydrogel scaffolds compared to non-deg scaffolds (Figure III-6). This difference likely impacted hMSC function, as Loebel *et al.* previously reported that cell-secreted nascent proteins act as an adhesive layer between cells and hydrogel matrix and cellular adhesion on the ECM layer is critical for hMSC spreading, mechanosensing, and osteogenic differentiation.[122] Several other works have also demonstrated cell-secreted ECM can play a pivotal role in hMSC differentiation.[113, 123, 124]

While our findings on the effects of degradability are important and likely can be generalized to other MAP hydrogel platforms, we also sought to study the interplay between degradability and microgel functionalization with different integrin-binding peptides on hMSC behavior. We were specifically interested in comparing MAP hydrogels functionalized with RGDS and c(RRETAWA), as the latter has been shown to induce hMSC osteogenic differentiation.[106, 108] While most of the work on c(RRETAWA) has studied the effects of soluble peptide, Gandavarapu *et al.* showed that hMSCs grown on 2D PEG hydrogels functionalized with c(RRETAWA) differentiated down the osteogenic lineage without the addition of other soluble factors.[109] This prior work is particularly relevant to our study here because hMSCs incorporated during microgel annealing are not embedded in a hydrogel network and instead can interact with the 2D microgel surfaces, despite the 3D nature of the MAP hydrogels.

Importantly, we found that microgel degradability was critical for eliciting responses by hMSCs to the different integrin-binding peptides. Cellular OPG secretion, which is an early marker of osteogenic differentiation, peaked earlier in fast-deg MAP hydrogels with both RGDS and c(RRETAWA) functionalization (Figure III-7). The effects of degradability and the integrin-binding peptides were further apparent when analyzing VEGF and BMP-2 secretion. While no differences between the peptides were seen in non-deg control MAP hydrogels, overall VEGF secretion was increased in RGDS scaffolds whereas BMP2 secretion was increased overall and on a per cell basis in response to c(RRETAWA) scaffolds (Figure III-8). While the up-regulated VEGF secretion mainly resulted from the high cell number in RGDS hydrogels, the higher BMP-2 secretion in the c(RRETAWA) group agrees with the osteogenic effects of c(RRETAWA) reported previously.[109] The importance of degradability in elucidating these effects could be related to the changes in surface topography and extracellular protein deposition in the degradable MAP hydrogels, but it could also be attributed to changes in cell-cell interactions, as cell-cell clustering was only observed in the fast-deg group (Figure III-3). Previous work has demonstrated cell-cell interactions in biomaterial scaffolds regulates paracine secretion of hMSCs and promotes regenerative capacity.[98, 125] It is also possible that cell traction during degradation can result in matrix reorganization and clustering of integrin-binding ligands, which has been demonstrated to enhance osteogenic differentiation of hMSCs in dynamic bulk hydrogels previously.[29, 30, 126]

Conclusion

In summary, we demonstrate that cell-mediated degradation in PEG-based MAP hydrogel scaffolds plays an important role in hMSC growth, extracellular protein deposition, and responsiveness to different integrin-binding peptides. Thus, degradability is a critical variable that should be considered in future studies on cell-material interactions in MAP hydrogels. In addition, we found that in enzymatically degradable MAP hydrogels RGDS promoted higher overall VEGF secretion whereas the α5β1 binding peptide c(RRETAWA) promoted higher secretion of BMP-2 overall and on a per cell basis. Future work should aim to test if c(RRETAWA) functionalized MAP hydrogels can improve the efficacy of hMSC delivery for bone tissue engineering. Another particularly interesting possibility would be to leverage the differential effects of c(RRETAWA) and RGDS for bone tissue engineering by combining microgels presenting these two peptides into a single MAP hydrogel. Such an approach would exploit the modularity of MAP hydrogels and their unique ability to be constructed from multiple types of microgel building blocks, which is another important feature of these biomaterials that could potentially lead to superior tissue engineering outcomes.

Supporting Information

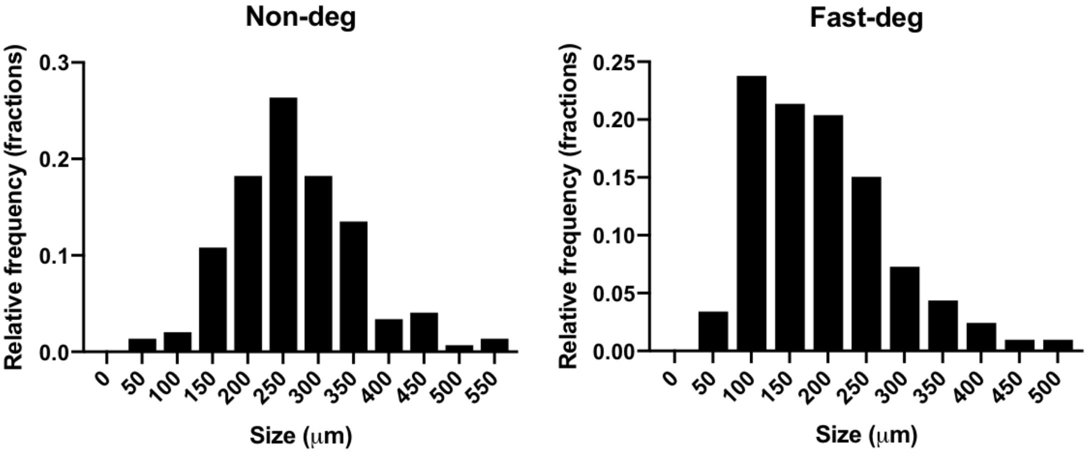

Figure III-10. Size distribution of Non-deg and Fast-deg microgels. Reprinted with permission from Xin *et al.*, 2019, *Acta Biomaterialia*, DOI: https://doi.org/10.1016/j.actbio.2019.11.009, Elsevier.

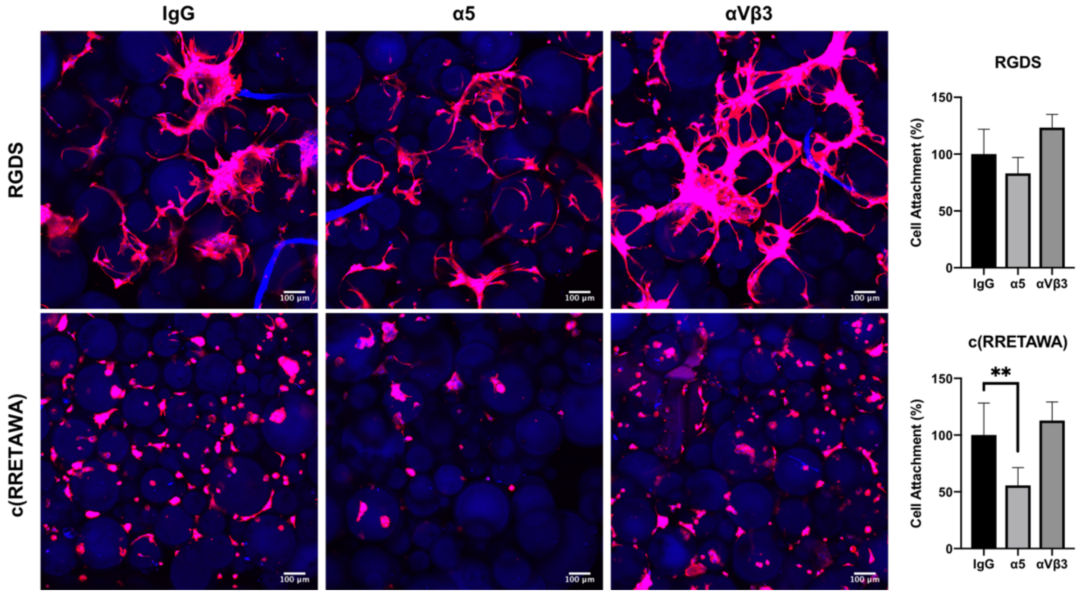

Figure III-11. hMSC attachment within RGDS and c(RRETAWA)-functionalized scaffolds after integrin blocking. Red = F-actin and blue = nuclei (note: background staining of microgels is also seen). Scale bars are 100 μm. Statistical analysis was performed by one-way ANOVA and Tukey post hoc comparisons. ** indicates $p < 0.01$. Reprinted with permission from Xin *et al.*, 2019, *Acta Biomaterialia*, DOI: https://doi.org/10.1016/j.actbio.2019.11.009, Elsevier.

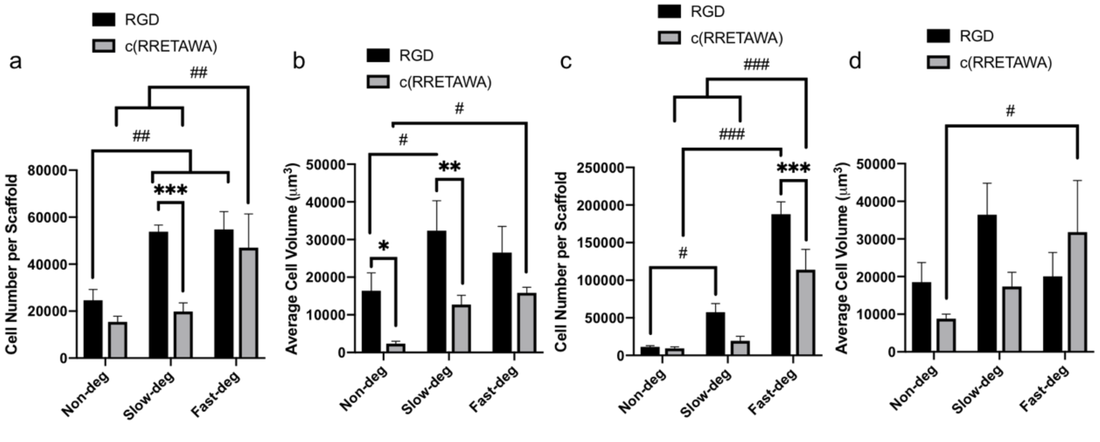

Figure III-12. The effect of peptide functionalization on hMSC spreading and proliferation in MAP hydrogels after a, b) 2d and c, d) 8d. Statistical analysis was performed by two-way ANOVA and post hoc Tukey tests. Comparisons between RGDS and c(RRETAWA) groups are indicated by * signs, where * indicates $p < 0.05$, ** indicates $p < 0.01$, and *** indicates $p < 0.0001$. Comparisons between Non-deg, Slow-deg, and Fast-deg groups are indicated by # signs, where # indicates $p < 0.05$, ## indicates $p < 0.01$, and ### indicates $p < 0.0001$. Reprinted with permission from Xin *et al.*, 2019, *Acta Biomaterialia*, DOI: https://doi.org/10.1016/j.actbio.2019.11.009, Elsevier.

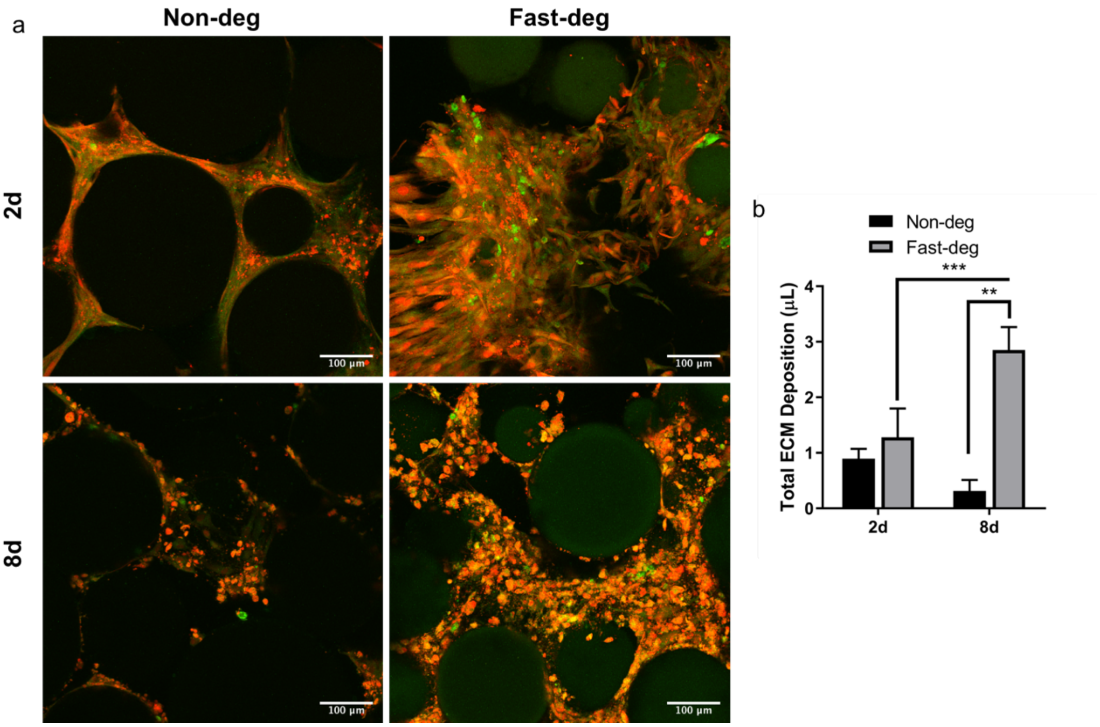

Figure III-13. Total extracellular protein synthesized by hMSCs in MAP hydrogels with varying degradability. a) Z-projection images from confocal microscopy. Green = cell membrane and red = protein. b) Quantification of total ECM protein per 50 µL MAP hydrogels. Scale bars are 100 µm. Statistical analysis was performed by two-way ANOVA with post hoc Tukey tests. ** indicates $p < 0.01$ and *** indicates $p < 0.0001$. Reprinted with permission from Xin *et al.*, 2019, *Acta Biomaterialia*, DOI: https://doi.org/10.1016/j.actbio.2019.11.009, Elsevier.

CHAPTER IV

INJECTABLE MODULAR MICROPOROUS ANNEALED PARTICLE HYDROGELS WITH PHYSICOCHEMICAL GRADIENTS FOR SCREENING OF CELL-MATERIAL INTERACTIONS

Overview

MAP hydrogels are an attractive platform for engineering biomaterials with controlled heterogeneity. Here, we introduce a microfluidic method to create physicochemical gradients within PEG based MAP hydrogels. By combining microfluidic mixing and droplet generator modules, microgels with varying properties were produced by adjusting the relative flow rates between two precursor solutions and collected layer-by-layer in a syringe. Subsequently, the microgels were injected out of the syringe and then annealed with thiol-ene click chemistry. Fluorescence intensity measurements of constructs annealed *in vitro* and after mock implantation into a tissue defect showed that a continuous gradient profile was achieved and maintained after injection, indicating utility for *in situ* hydrogel formation. The effects of physicochemical property gradients on hMSCs were also studied. Microgel stiffness was studied first, and the hMSCs exhibited increased spreading and proliferation as stiffness increased along the gradient. Microgel degradability was also studied, revealing a critical degradability threshold above which the hMSCs spread robustly and below which they were isolated and exhibited reduced spreading. This method of generating spatial gradients in MAP hydrogels could be further used to gain new insights into cell-material interactions, which could be leveraged for tissue engineering applications.

Introduction

The ECM consists of hundreds of proteins and glycoproteins and presents a complex milieu of biochemical and physical cues that guide cellular activities during tissue development and regeneration.[26, 95, 127] Developing biomaterials that mimic the ECM is of great interest in the tissue engineering field in order to better understand cell-material interactions and orchestrate regeneration and repair. Hydrogels are considered to be ECM mimetic and have been widely utilized as injectable biomaterial systems for stem cell delivery.[8, 93, 128, 129] However, while their bulk physicochemical properties can be engineered to regulate cellular responses, most injectable hydrogel platforms are crosslinked in situ directly from homogeneous precursor solutions. Recent advances in 3D printing and photolithography have made it possible to manufacture hydrogels with spatially varying physicochemical properties.[130-132] However, hydrogels manufactured through these techniques lack injectability since chemical crosslinking is required to prevent mixing of the heterogeneous regions and, thus, lock in the spatial patterning.[133, 134]

Recently, assembling individual microgels into 3D tissue engineering scaffolds, termed as microporous annealed particle or MAP hydrogels, has emerged as a promising new approach to fabricating hydrogels for tissue engineering. Injectability is one important feature of MAP hydrogels since the microgels can be injected and secondary crosslinking can take place *in situ*.[63, 76, 110] In addition, MAP hydrogels inherently possess a highly interconnected microporous structure, which permits enhanced cell spreading and proliferation compared to conventional nanoporous hydrogels.[63] This approach is also uniquely suited to form hydrogel scaffolds with heterogeneous properties, as the modular nature of the microgel assembly process allows the incorporation of multiple microgel formulations within a single construct.[100] For example, Mealy et al. recently demonstrated the assembly of two distinct microgels with random distribution through cyclodextrin and adamantane guest–host interactions and achieved multiplexing of molecule release and degradation profiles of the MAP hydrogels.[67] They also showed that the materials could be injected into rat myocardial infarcts due to the microscale size of the microgels and shear-thinning behavior. In addition, Darling et al. described zone patterning of microgels distinguished by different fluorescent labeling and showed that these microgel divisions could be largely maintained after injection into murine models of wound healing and stroke.[135] However, regeneration often involves more complex presentations of microenvironmental cues, such as physicochemical gradients.[136, 137] While the zone patterning approach can in theory be used to manually assemble different batches of microgels with varying physicochemical properties, the resulting gradients would be coarse and discrete in nature. Therefore, an approach to fabricate continuous gradients in MAP hydrogels in a precise and controllable fashion is highly desired.

Producing MAP hydrogels with physicochemical gradients is non-trivial and presents two significant technical challenges. The first challenge is the requirement for a variable precursor solution input to allow the fabrication of microgels with varying properties over time. This requirement eliminates microgel synthesis methods such as electrospraying and emulsification, which produce batches of microgels with homogenous properties.[65, 101] Alternatively, microfluidic techniques, which are often used to produce microgel building blocks for MAP hydrogels,[63, 67, 100, 138] are suitable as they can generate droplets in a simple microfluidic channel one at a time and precursor solutions can be mixed at varying ratios within the microfluidic channel without manual pipetting steps.[139] While microfluidic techniques have previously been used to generate gradients in hydrogel slabs,[140-142] microfluidics has not been previously applied to the production of gradients in MAP hydrogels due to the second technical challenge, which is the requirement to spatially localize the microgels to desired regions after their synthesis.

Herein we report a method to create gradients in MAP hydrogels using a microfluidic droplet generator equipped with a microfluidic mixing module, thiol-ene click chemistry, and layered packing into a collection device. Importantly, the microfluidic system permitted mixing of two distinct precursor solutions at programmed ratios to precisely modulate the composition of the microgels over time, whereas the collection and packing strategy maintained their positions until annealing could be performed. Initial experiments were performed using fluorophore-labelled microgels, and the effects of layer thickness on gradient patterning was studied. Subsequently, the extrusion of the microgels and maintenance of the gradient after annealing via secondary thiol-ene photopolymerization was studied in vitro and in a mock implantation study.

Lastly, MAP hydrogel scaffolds with gradients in microgel stiffness and degradability were produced to study cell-material interactions with hMSCs.

Materials and Methods

Preparation of Microfluidic Device

The microfluidic device was made of polydimethylsiloxane by standard soft lithography.[143-145] Master molds were fabricated on a 4-inch silicon wafer by a photolithographic technique using a negative photoresistor (SU8 2075, MicoChem). Microfluidic devices were molded from master molds by pouring degassed polydimethylsiloxane (Sylgard 184, Dow, elastomer: crosslinker = 10:1) and cured at 85 ˚C for 1 h. polydimethylsiloxane devices were then placed onto a glass slide coated with polydimethylsiloxane (elastomer: crosslinker = 20:1) and bonded together at 85 ˚C overnight. The Y-shaped mixing module allowed mixing of two different gel solutions at different ratios.[146] Microgel droplets were generated at a T-junction where the oil phase broke off the mixed gel solution into droplets. A winding channel was used to create chaotic advection in droplets to accelerate the mixing of gel solutions within droplets.[147] The channel height of the microfluidic device was 150 µm, with the oil phase channel width being 200 µm and the Y-shaped mixing module channel width being 160 µm.

Generation of Microgel through Microfluidics

PEG thiol-ene based gel precursor solutions consisted of four-arm PEG-Nb (synthesized from four-arm PEG-hydroxyl as previously reported)[79], bi-functional thiol crosslinker, LAP (synthesized as previously described)[77] photoinitiator, and CGRGDS (prepared via Fmoc solid phase peptide synthesis). The physicochemical properties of the microfluidically generated microgels were tuned by adjusting the gel composition.

Fluorescent intensity gradients were achieved using non-fluorescent and SAMSA-fluorescein (100 µ*M*, Invitrogen) labelled microgels (note: SAMSA-fluorescein possesses a thiol and is conjugated to the PEG). The stiffness gradient was achieved by using 5 kDa and 20 kDa PEG-norbornene. The degradability gradient was achieved by using PEG-DT (3,400 Da, Laysan Bio.) and KCGPQGIWGQCK (AAPPtec) crosslinkers.

Syringe pumps (Pico-plus, Harvard Apparatus) were used to control volumetric flow rates of all input streams through a LabView program (National Instruments). The total flow rate of the two gel solutions into the microfluidic device was 140 µl/h, and the flow rate of fluorinated oil (Novec 7500, 3M) containing 2% fluorosurfactant (Pico-surf 1, Dolomite) was 350 µl/h. The droplet generation speed was 13,320 droplets/h. The generated droplets were photocrosslinked into microgels downstream in the outlet tubing (25 mW/cm^2, 72 s, 365 nm, Lumen Dynamics Omnicure S2000 Series) and collected into a 1 mL syringe. A hole was punched at the bottom of the syringe to remove excessive oil during microgel collection. 100 µL of microgels having gradients in their physiochemical compositions were collected in the syringe, with another 100 µL of buffer microgels (i.e., no gradient profile) collected at the bottom to fill the dead space during injection. The fluorinated oil was allowed to evaporate from the packed microgels for 2 days at room temperature to achieve stable packing before use.

Annealing into Gradient MAP Scaffolds

The packed microgel gradients were slowly injected into a rectangular shaped silicone mold with a width of 3 mm, which was approximately the same width as the inner diameter of the 1 mL syringe. The injected microgels were stored overnight for complete evaporation and removal of the fluorinated oil. 4 µL 20 wt% PEG-DT and 1.5 µL 100 m*M* LAP were added onto the microgels to anneal (10 mW/cm^2, 3 mins, 365 nm) them into gradient MAP scaffolds. The scaffolds were then allowed to swell in 1X phosphate buffered saline until reaching equilibrium.

Characterization

Mixing of the two gel solutions and microgel droplet formation were observed using an upright microscope (Eclipse LV 100D, Nikon) with a high-speed camera (C11440, Hamamastu). Swollen microgels were imaged using a light microscope, and their sizes were measured using the ImageJ software (NIH). A stereomicroscope (Stemi 508, Zeiss) with 0.5X objective was used to image the entire gradient scaffold in fluorescence field. The fluorescent intensity was quantified using the ImageJ software. The Young's moduli of MAP hydrogels prepared from the hydrogel precursor solutions were measured by atomic force microscopy (Dimension Icon, Bruker) with a SiO_2 colloidal probe (5 µm diameter, spring constants 0.6 N/m; Novascan). The degradation curves of MAP hydrogels prepared from hydrogel solutions were obtained by immersing samples in a 0.2 mg/mL collagenase B (Sigma) solution at 37 °C and weighing the remaining mass every 15 minutes.

Mock Implantation Study

Freshly euthanized C57BL/6 mice were provided by the Animal Resource Sharing Program of the Comparative Medicine Program at Texas A&M University. The mice were used to demonstrate the implantation of microgel gradients into a mouse critical-sized femoral defect model, as previously described.[115] In brief, the skin was incised along the longitudinal axis of the femur and the intermuscular boundary was dissected to expose the femur. A segment was cut from the mouse femur using a fine micro-drill (Braintree Scientific) fitted with a fine diamond-grit coated cutting wheel (Strauss Diamond). The microgel gradients were injected into the bone space and then the microgels were assembled via *in situ* photopolymerization (10 mW/cm^2, 3 mins, 365 nm) with the addition of 4 µL 20 wt% PEG-DT and 1.5 µL 100 m*M* LAP. A stereomicroscope (Stemi 508, Zeiss) with a 0.5X objective was then used to image the gradient MAP scaffolds.

Cell Seeding

hMSCs were acquired from the Institute of Regenerative Medicine at Texas A&M University and cultured in α-Minimal essential medium (Gibco) supplemented with 20% v/v fetal bovine serum (FBS, Atlanta Biologicals), 2 m*M* GlutaMAX (Gibco), 50 U/mL penicillin (Gibco), and 50 µg/mL streptomycin (Gibco) at 5% CO_2 and 37 °C in a humidified environment. hMSCs were used up to Passage 5. hMSC suspensions were mixed with 4 µL 20 wt% PEG-DT and 1.5 µL 100 m*M* LAP, and the mixture was seeded throughout the gradient scaffold during the annealing process. For 100 µL scaffolds, 500,000 cells were seeded. hMSCs were cultured within the stiffness gradient scaffolds for 2 days and the degradability gradient scaffolds for 5 days.

Immunostaining and Imaging

Samples were fixed using 4% formaldehyde for 15 min at room temperature. Cytoskeletal staining was performed using rhodamine phalloidin (1:40, Invitrogen) with counter staining of DAPI (1:1000, Jackson ImmunoResearch). Samples were imaged using a confocal microscope (FV1000, Olympus) with 200 µm Z-stack throughout the scaffolds. The images were analyzed using the ImageJ software. For cell number quantification, the 3D Objects Counter plugin was used to count the number of nuclei based on DAPI staining. The Voxel Counter plugin was used to measure the total cell volume in a z-stack based on phalloidin staining after thresholding. The average cell volume was then calculated by dividing the total cell volume by cell number.

Results and Discussion

Microgel Production via Microfluidics

A microfluidic droplet generator with a mixing module that is capable of altering mixing ratios of precursor solution was used to generate the microgel building blocks for the MAP hydrogels (Figure IV-1a). The Y-shaped microfluidic mixing module had two inlets through which two different gel precursor solutions with different properties were flown at varying flow rate ratios, which were controlled by programming the flow rates of the two solutions over time through two independently controllable syringe pumps. By changing the flow rate ratios, a stream of mixed solutions having different properties could be generated and the total flow rate kept constant. The microgel solutions composed of the two different precursor solutions were flown into a T-junction droplet generator module where the mixed precursor solutions were pinched off by the continuous oil phase to generate discrete water-in-oil emulsion droplets. A winding channel created chaotic advection within the droplets to accelerate the mixing of gel solutions within the droplets.[147] The droplets were then channeled into tubing and photopolymerized downstream, followed by collection of the polymerized microgels layer-by-layer in a syringe, which could then be dispensed as needed.

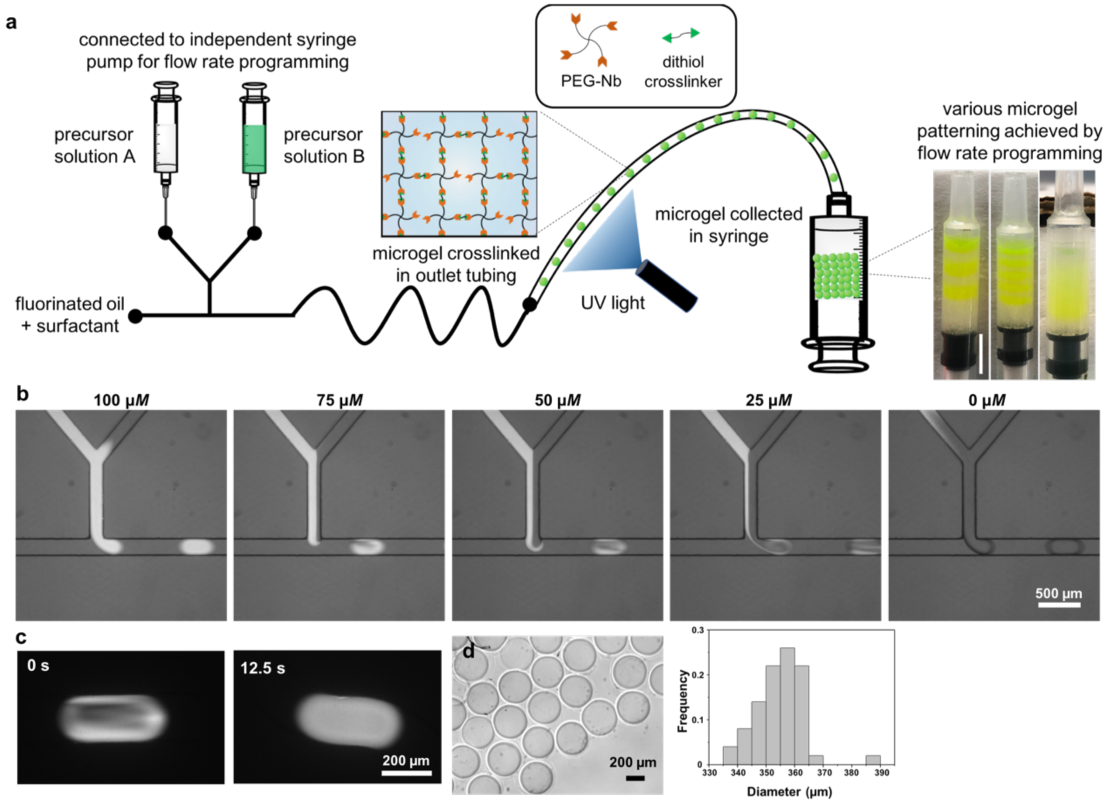

Figure IV-1. Microgel synthesis using a microfluidic device with a Y-shaped mixing module and a T-junction droplet generator module. a) Schematic of the microfluidic device-based microgel production procedure. Right side photograph showing examples of microgel patterning using this method. The scale bar is 5 mm. b) Fluorescent images of non-fluorescent and fluorescent gel solutions merging together with varying ratios in the Y-shaped mixing module. c) Fluorescent images showing that the two gel solutions were mixed completely within 12 seconds after droplet formation. d) Size distribution of microgels synthesized from 5 kDa PEG-norbornene and PEG-DT.

The microgel precursor solutions contained four-arm PEG-Nb, bi-functional thiol crosslinker, photoinitiator, and mono-thiol cell-adhesive peptide ligand. Thus, the microgels were synthesized via thiol-ene click chemistry. This synthetic approach enables facile tuning of the physicochemical properties of the resultant microgels simply by adjusting the specific composition of the precursor solution, which was exploited for various gradient designs (Table IV-1). Additional advantages of thiol-norbornene click chemistry are its oxygen insensitivity, which is important because oxygen inhibition can be a challenge in microfluidics,[148] fast reaction kinetics to achieve crosslinking in the outlet tubing,[149] and the step-growth nature of the reaction. The latter feature was leveraged to ensure that the microgels would contain unreacted norbornene groups and could be annealed with a bis-thiol linker and a secondary thiol-ene photopolymerization after gel particle generation, similar to our previous work.[101] Compared to other microgel assembly chemistries, the use of thiol-ene photopolymerization for annealing here is important because the reaction can be spatiotemporally controlled to prevent premature assembly of the packed microgels and, thus, maintain their injectability.[150] Thiol-ene chemistry also provides cytocompatible conditions for cell incorporation.[11]

We first characterized the droplet generation from the mixture of two precursor solutions by using FITC-containing (FITC gel, 100 μ*M*) and fluorophore-free precursor solutions (blank gel) (Figure IV-1b). By keeping the total flow rate of those solutions constant, varying the relative flow rates of these two gel solutions resulted in different FITC concentrations in the droplets, and the flow rates were programmed so that alternating layers of packed microgels (alternating FITC-containing and non-fluorescent microgel layers) were generated within the collection syringe (Figure IV-1a, right image). Complete mixing of the two solutions within the droplets was achieved within 12.5 seconds due to accelerated diffusion in the winding channel (Figure IV-1c), which was critical to achieving uniform physicochemical properties within a single microgel droplet. Crosslinked microgels were monodispersed with an average diameter of 355 ± 9 μm (CV = 2.5 %) (Figure IV-1d). If different microgel sizes are desired for specific applications, the dimensions of the microchannel can be simply modified to obtain different microgel sizes as needed.

Fluorinated oil with non-ionic surfactant was used as the continuous oil phase. This aspect is notable since the oil must be removed after microgel preparation for biomedical applications, but microgel washing often requires rigorous agitation, which would disturb the microgel packing and patterning. However, fluorinated oil is a desirable choice in this application due to its high volatility, as it can be removed without washing steps. Previous work utilized the volatility of fluorinated oil to achieve hexagonal packing of microfluidic hydrogel particles.[151] Here, we show that this oil can be completely removed by evaporation at room temperature (Figure IV-7) and, thus, the patterned microgel array was not disturbed during the oil removal process. In addition, fluorinated oil and non-ionic surfactant systems have exhibited the best biocompatibility to date in droplet microfluidics.[152, 153] Therefore, this system also provides opportunities to form cell-laden microgel arrays, which could be leveraged for patterning of different cell types in other future applications.

Microgel Patterning and Gradient Profiles

To characterize the resolution of microgel packing and the resulting microgel gradient profiles, further testing was conducted by altering the FITC concentration in the microgels over time. As crosslinked microgels came out from the outlet tubing, they were packed layer-by-layer into a 1 mL syringe pre-filled with fluorinated oil. Since fluorinated oil has a higher density than aqueous gel phase, microgels would float and spread to occupy the oil surface. As more gel droplets come into this collection syringe, the next layer will form on top of the first layer. To characterize the accuracy of microgel packing, we first investigated the packing of microgels by creating alternating layers of fluorescent and non-fluorescent microgels by switching the precursor solution between 100 % FITC gel and 100 % blank gel. Here, microgels having a diameter of 355 µm were generated at a rate of 3.7 droplets/s (total flow rate of two precursor solutions: 140 µl/h , carrier oil flow rate: 350 µl/h). The packed layer thickness, which is defined by the number of microgels per layer and controllable by the duration of microgel collection time for the given microgel generation speed, was varied to be 1, 3, 6, and 12 microgels per layer. Considering the syringe inner area of 17.94 mm^2, this means that generating a monolayer of microgels would take 80 s. Distinguishable layers of microgels were identified in the 3, 6, and 12 microgels per layer groups, with the layer thickness approximately matching the expected values based on the microgel size and generation time (Figure IV-2). However, we did not observe distinguishable layers in the 1 microgel per layer group, which was attributed to microgel spreading and the nature of spherical packing. It is notable that the switching of precursor solution input can be completed almost instantaneously and, thus, will not affect the gradient composition.

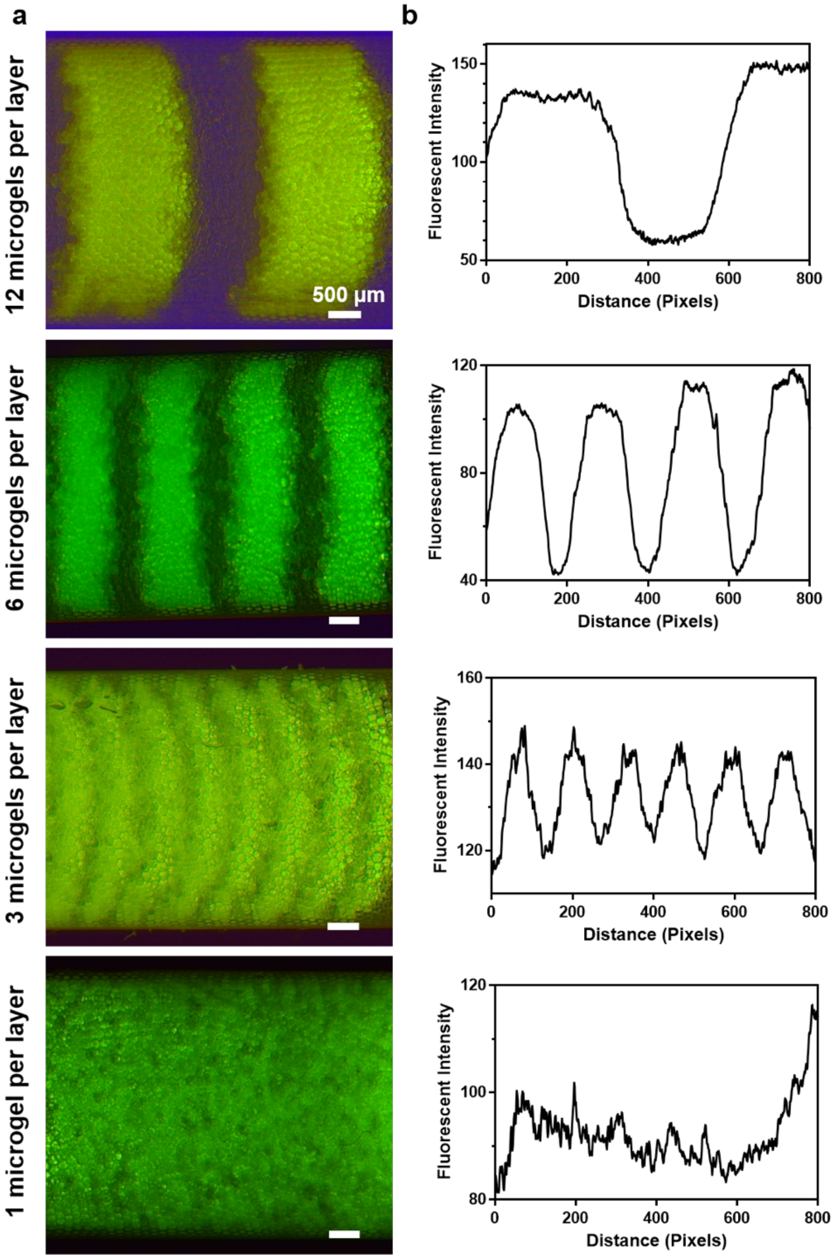

Figure IV-2. Layer-by-layer packed microgels in a syringe with alternating fluorescent and non-fluorescent microgel layers. a) Fluorescent images of packed microgels with 1, 3, 6, and 12 microgels per layer. b) Fluorescent profiles of packed microgels with 1, 3, 6, and 12 microgels per layer.

Whereas the aforementioned results were for binary patterns, creating physicochemical gradients requires that the flow rate of one gel solution undergo step increases while that of the other gel solution undergoes step decreases (Figure IV-8). The duration of each step was then determined to adjust the thickness of each gradient layer. We then studied the fluorescent gradient profiles of packed microgels with 1, 3, 6, and 12 microgels per layer (Figure IV-3). Continuous gradient profiles were observed when the layer thickness was 1, 3 or 6 microgels, which also correlated well to the standard curve of FITC gel precursor solutions (Figure IV-9). Importantly, the microgel spreading at layer boundaries shown in the alternating layer packing smooths the gradient and facilitates the generation of a precise fluorescent microgel gradient with minimum layer thickness. However, a step gradient profile was shown in the 12 microgels per layer group. All groups had a similar range of fluorescence intensity, indicating the accuracy of microgel packing. Overall, these results indicate that our microfluidic method can generate continuous gradients as desired and, thus, provide a foundation for producing physicochemical property gradients by simply altering the precursor solutions during the microgel generation process.

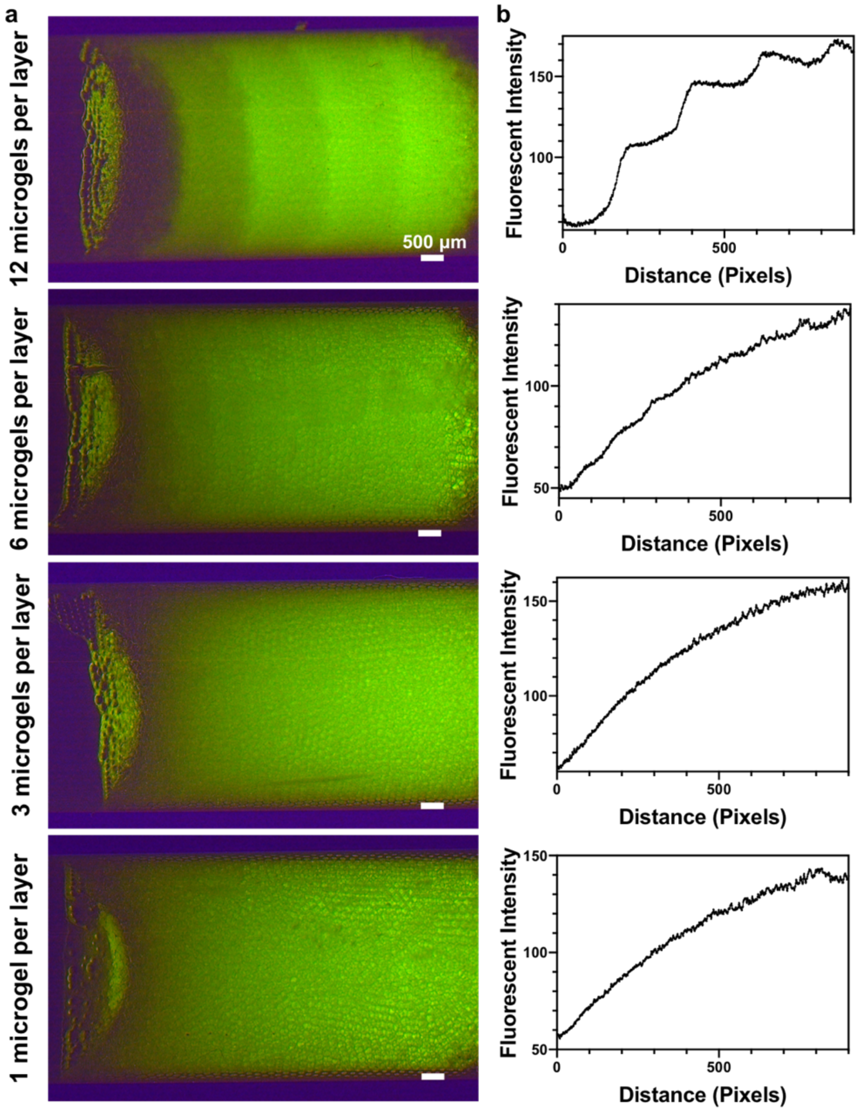

Figure IV-3. Packed microgels in a syringe with fluorescent gradient. a) Fluorescent images of microgel gradients with 1, 3, 6, and 12 microgels per layer. b) Fluorescent profiles of microgel gradients with 1, 3, 6, and 12 microgels per layer.

Annealing and Mock Implantation of Gradient MAP Hydrogel Scaffolds

Next, we tested if gradients could be maintained after the microgels are injected out of the syringe and annealed into MAP hydrogels. Prior to injection, the surrounding oil in the syringe was allowed to evaporate to facilitate stable packing of microgels.

Next, the packed microgels in the syringe were injected into a rectangular silicone mold (Figure IV-4). After injection, fluorescence microscopy revealed that the continuous fluorescent intensity profile was maintained (Figure IV-4b), suggesting excellent injectability of microgel gradients and limited movement of the microgels during the injection process. PEG-DT linker and photoinitiator were then added on top of the gradient to anneal the microgels via thiol-ene click chemistry.

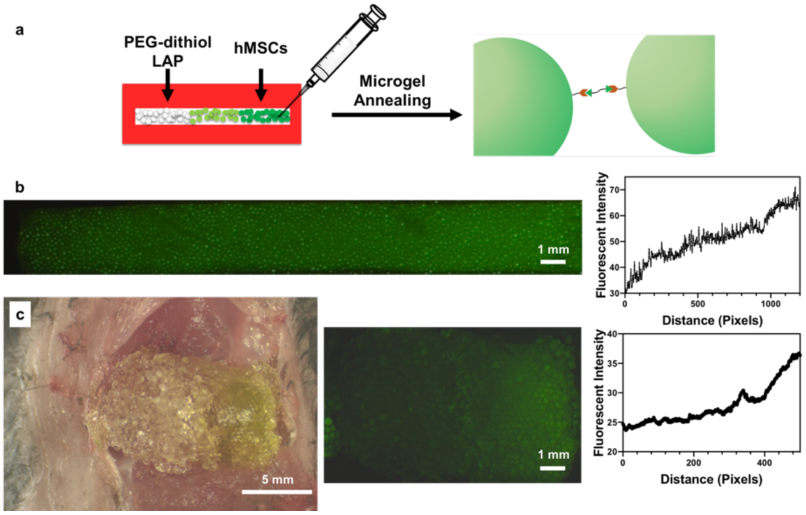

Figure IV-4. Extrusion of the microgel gradients. a) Schematic illustrating microgel extrusion into a 3 mm rectangular mold and microgel annealing into scaffolds. b) Fluorescent image of an extruded gradient MAP scaffold with 6 microgels per layer and quantification of fluorescent intensity throughout the scaffolds. c) Image showing gradient MAP scaffolds injected into a mouse femoral defect.

Importantly, we show that these gradient MAP hydrogels can be implanted into a tissue defect, using mock implantation into a mouse femoral defect as an example (Figure IV-4c). The packed microgels were injected from the syringe into the femoral defect and the fluorescent intensity gradient was mostly maintained within the implanted microgels. The annealing process was performed *in situ* after implantation with UV irradiation (10 mM/cm^2 for 3 mins). This example demonstrates the possibility of applying gradient or patterned MAP scaffolds into tissue defects. Future applications include MAP hydrogels with stiffness gradients that can permit durotaxis to promote rapid migration of endogenous cells into the defect center to accelerate tissue healing. Alternatively, a combination of microgels with varying surface ligands could be used to facilitate osteogenesis and angiogenesis for more rapid bone regeneration.

Insight on Cell-material Interactions from Gradient MAP Hydrogels

Cell-material interactions were also investigated using the 6 microgels per layer gradient MAP hydrogels by seeding hMSCs during the annealing process. MAP hydrogels with stiffness gradients from Young's modulus of 9.8 to 29.2 kPa were achieved by using hydrogel macromers with varying molecular weights (from 5 kDa to 20 kDa PEG-norbornene) in the two gel precursor solution inlets (Figure IV-5). After 2 days of culture, confocal fluorescence microscopy images showed the hMSCs exhibited greater spreading and proliferation with increasing stiffness throughout the scaffold (Figure IV-5c and d). Moreover, the increases were continuous, which is similar to what is seen in 2D cultures.[92] Importantly, this result corroborates our prior finding that hMSC behavior in MAP hydrogels follows trends observed in 2D rather than conventional 3D hydrogel cultures,[101] which we attribute to the more permissive microporous cellular microenvironment. Future work could leverage similar gradients to better understand the effects of microgel stiffness on cell migration and mechanotransduction in MAP hydrogels.

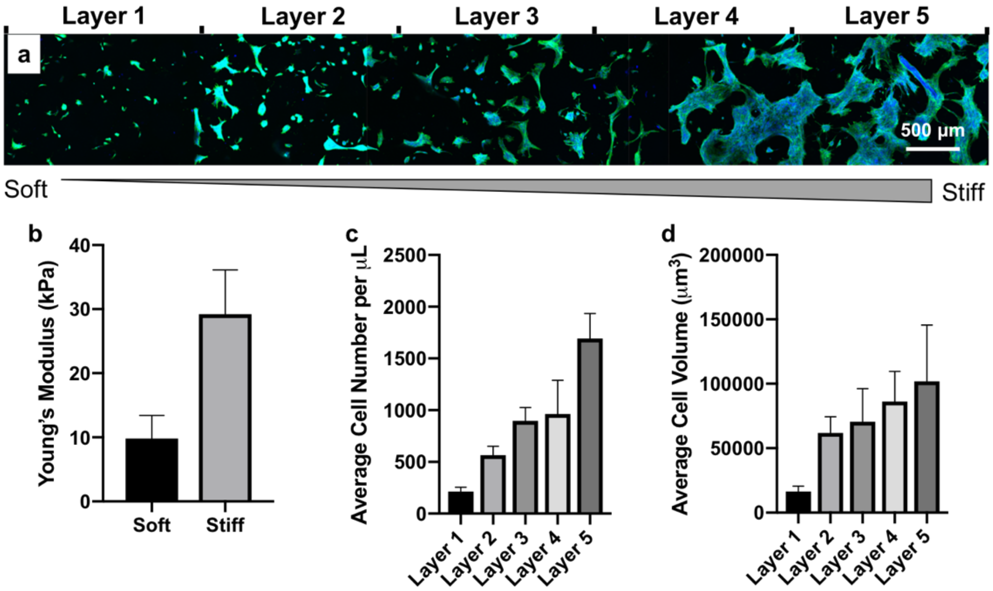

Figure IV-5. hMSC proliferation and spreading in MAP scaffolds having a stiffness gradient. a) Z-projection image of hMSCs cultured within the stiffness gradient scaffolds. Green represents F-actin and blue represents nuclei. b) Young's moduli of the MAP scaffolds from the two precursor solutions. Quantification of c) average cell number per µL and d) average cell volume in each region.

Next, MAP hydrogels with a degradability gradient from 100% to 0% degradability were produced by using matrix metalloproteinase degradable KCGPQGIWGQCK and non-degradable PEG-DT crosslinkers in the two gel precursor solution inlets (Figure IV-6). However, instead of continuous spreading and proliferation trends throughout the scaffold, there was a critical reverse gelation point in the degradability gradient scaffolds. Above this point (i.e., left side of the image in Figure IV-6a), hMSCs spread robustly and formed a cellular network around the microgels, whereas cells were isolated into individual divisions with less spreading below this point (i.e., right side of the image in Figure IV-6a). It appears that the ratio of degradable linker needs to be higher than the critical reverse gelation point for cells to fully degrade the surrounding gel and spread better. Interestingly, the fact that the cells either spread better or not suggests that there may not be a benefit to using microgels with 100% degradable crosslinker.

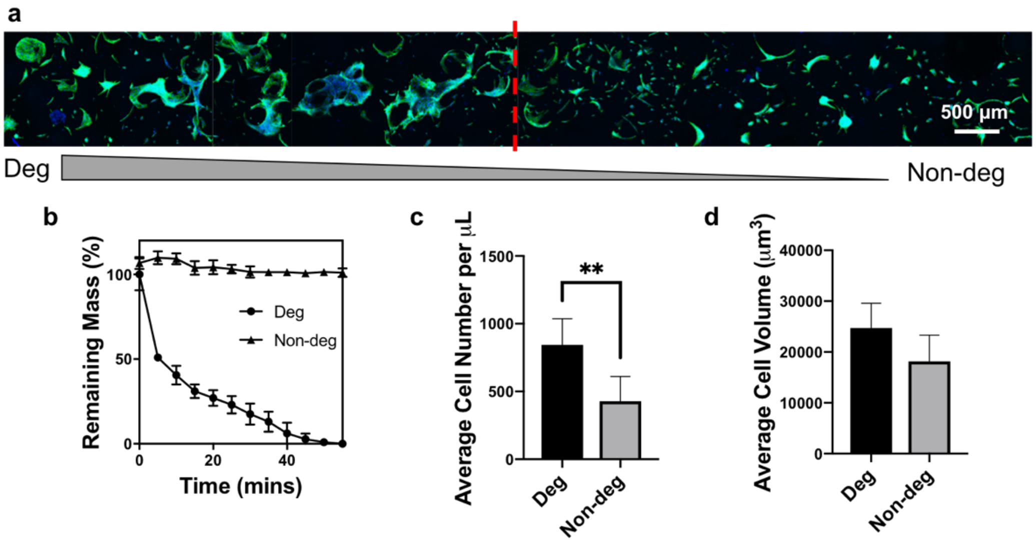

Figure IV-6. hMSC proliferation and spreading in MAP scaffolds with a degradability gradient. a) Z-projection image of hMSCs cultured within the degradability gradient scaffolds. Green represents F-actin and blue represents nuclei. b) Degradation curves of the MAP scaffolds prepared from the two precursor solutions. Quantification of c) average cell number per µL and d) average cell volume in degradable and non-degradable regions. **$p < 0.01$, one-way ANOVA.

Overall, the effects of various physicochemical properties on cellular responses in MAP hydrogels is of high interest for the design of these materials, with key parameters being microgel size, stiffness, linker concentration, and RGD concentration.[65, 101] However, these studies have all been carried out in MAP hydrogels with discrete parameters. In contrast, the gradient MAP hydrogels developed here can present continuous physicochemical values to provide more information on cell-material interactions compared to testing discrete values, for example cells exhibit differential spreading trends in the degradability and stiffness gradients here, making it a powerful platform to screen cell-material interactions.

Conclusion

We developed a microfluidic approach combining a microfluidic mixer module and a droplet generator module to create gradient MAP hydrogel scaffolds with changing physiochemical profiles within the scaffolds. This approach was successfully utilized to create MAP hydrogels with continuous physicochemical gradient. The injectability and suitability for implantation of gradient MAP hydrogels were demonstrated by mock implantation in which the scaffolds were directly injected into a mouse femoral defect. In addition, the ability to create gradients in MAP hydrogels can be leveraged to gain unique insights into cell-material interactions, which was demonstrated by showing that hMSCs exhibited differential spreading trends in the degradability and stiffness gradient scaffolds. In summary, the modular and high-accuracy nature of the MAP hydrogel generation method developed here has the potential to be utilized broadly in tissue engineering and regenerative medicine. Future work could include generation of gradient MAP scaffolds in a more complex manner with this microfluidic method, such as two-way gradients, to screen the interplay of two physicochemical cues on cell-material interactions for example.

Supporting Information

Table IV-1. Components of two microgel precursor solutions for fluorescent intensity, stiffness, and degradability gradients.

Components	Fluorescent Intensity		Stiffness		Degradability	
	A	B	A	B	A	B
Macromer	PEG-Nb 5kDa 18.2 m*M*	PEG-Nb 5kDa 18.2 m*M*	PEG-Nb 5kDa 18.2 m*M*	PEG-Nb 20kDa 4.9 m*M*	PEG-Nb 5kDa 18.2 m*M*	PEG-Nb 5kDa 18.2 m*M*
Crosslinker	PEG-DT 26.9 m*M*	PEG-DT 26.9 m*M*	PEG-DT 26.9 m*M*	PEG-DT 6.8 m*M*	PEG-DT 26.9 m*M*	peptide[a] 26.9 m*M*
LAP	2 m*M*	2 m*M*	2 m*M*	2 m*M*	2 m*M*	2 m*M*
CGRGDS	1 m*M*	1 m*M*	1 m*M*	1 m*M*	1 m*M*	1 m*M*
SAMSA-FITC	100 μ*M*	-	-	-	-	-

[a]Peptide sequence was KCGPQGIWGQCK

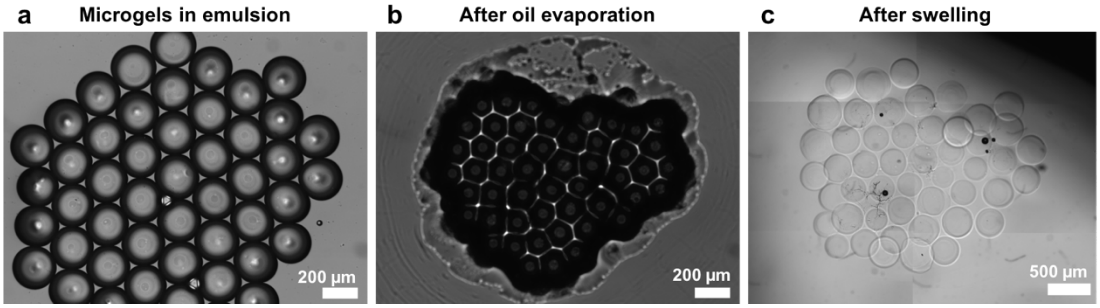

Figure IV-7. Microscopic images showing complete removal of the fluorinated oil after oil evaporation and microgel reswelling.

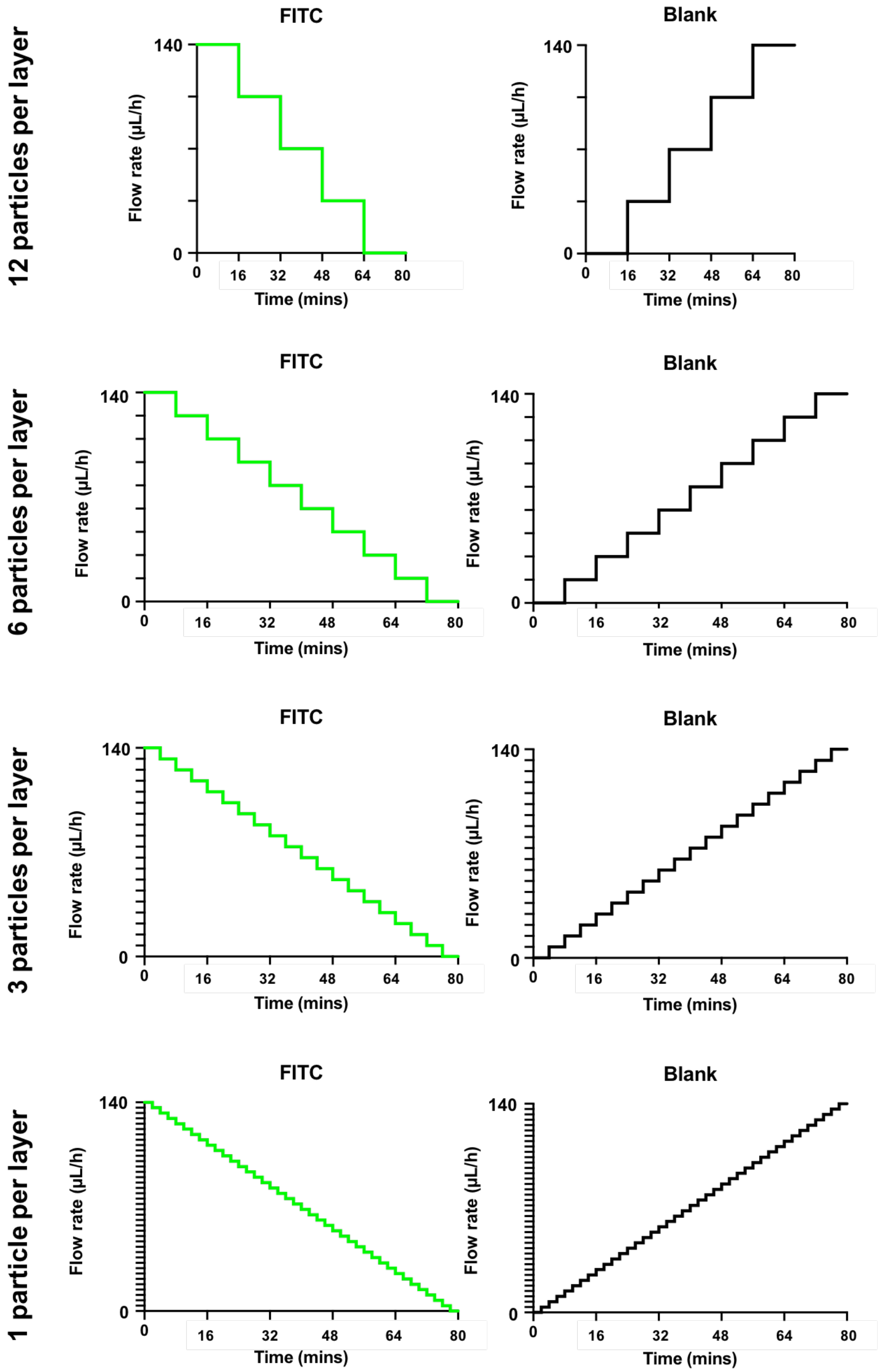

Figure IV-8. Flow rate profiles of the two precursor solutions for fluorescent intensity gradients with varying layer thickness.

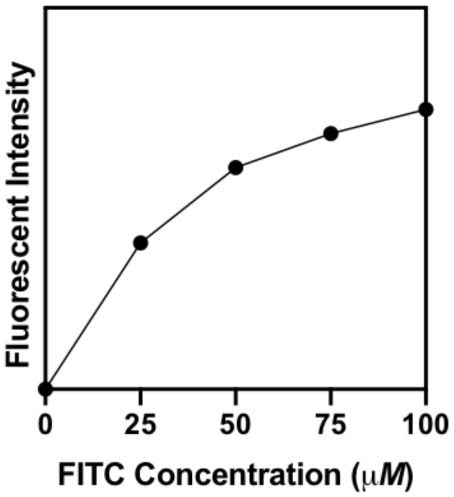

Figure IV-9. Standard curve of SAMSA-FITC fluorescent intensity from 0-100 µ*M*.

CHAPTER V

PEG MICROGELS AS BIOMATERIAL INKS FOR 3D BIOPRINTING OF MICROPOROUS ANNEALED PARTICLE HYDROGELS*

Overview

3D bioprinting is important in the development of complex tissue structures for tissue engineering and regenerative medicine. However, the materials used for bioprinting, referred to as bioinks, must have a balance between a high viscosity for rapid solidification after extrusion and low shear force for cytocompatibility, which is difficult to achieve. Here, a novel bioink consisting of PEG microgels prepared via off-stoichiometry thiol-ene click chemistry is introduced. Importantly, the microgel bioink is easily extruded, exhibits excellent stability after printing due to interparticle adhesion forces. The modularity of the bioink is also an advantage, as the PEG microgels have highly tunable physicochemical properties. The low force required for extrusion and cytocompatibility of the thiol-ene annealing reaction also permit cell incorporation during printing with high viability. Printed constructs can be annealed into MAP hydrogels with a second thiol-ene click reaction to confer long-term stability and allow cell spreading and proliferation in the interstitial spaces between the microgels. Overall, these results indicate that our microgel bioink is a promising and versatile platform that could be leveraged for bioprinting and regenerative manufacturing.

---

*Reproduced with permission from "Clickable PEG hydrogel microspheres as building blocks for 3D bioprinting" by Xin *et al.*, 2019, *Biomaterials Science*, 7 (3), 1179-1187, Copyright 2019 by The Royal Society of Chemistry.

Introduction

3D bioprinting has received great attention for manufacturing scaffolds with biofunctional components, such as therapeutic cells and growth factors, for tissue engineering.[154, 155] This method allows printing of customized, patient-specific medical devices for the development of precision biomaterials and personalized medicine.[156] There are many reported 3D bioprinting strategies, including inkjet, stereolithography, and extrusion.[157-159] In general, the materials used in 3D bioprinting, which are referred to as bioinks, are polymer precursor solutions that can crosslink into a hydrogel network via UV polymerization, ionic exchange, or thermal gelation.[160-163] In extrusion bioprinting specifically, which is widely used due to its low cost and ease of adoption,[164] a good bioink needs to be extruded smoothly (printability), solidify rapidly to avoid collapse (stability), and have good biocompatibility.[165] Most extrusion-based bioinks are viscous solutions in order to maintain structural integrity after extrusion, but these materials can require high shear force during printing, which can negatively impact cell viability.[166, 167]

Non-viscous precursor solutions, such as PEG and hyaluronic acid, are attractive base materials for bioinks because they can be encoded with cell-instructive cues for tissue engineering applications.[93, 168, 169] However, their lack of stability after extrusion is a challenge. One approach to improve the stability of non-viscous materials for extrusion bioprinting is nanoparticle reinforcement,[161, 170] but these additives can potentially affect the cell response. Alternatively, photopolymerization at the needle tip during extrusion has been shown to improve the stability of PEG, hyaluronic acid, and gelatin bioinks without compromising cell viability.[133] Elegant strategies that leverage reversible crosslinking have also been reported. For example, Yin *et al.* used a low concentration of thermo-crosslinked methacrylated gelatin to maintain high cell viability and an additional irreversible UV crosslinking step to enhance the mechanical strength.[171] More recently, Lou *et al.* exploited the dynamic nature of hydrazone crosslinking and demonstrated that incorporating a biocompatible catalyst affords low viscosity during extrusion but results in stable constructs after the catalyst diffuses out of the material after printing.[172] Despite these efforts, the ability to print multi-layered structures (> 10 mm tall) using non-viscous bioinks remains limited.

An alternative strategy that could circumvent the need to increase bioink viscosity is to use hydrogel microparticles (*i.e.*, microgels). Hinton *et al*. demonstrated that complex structures can be produced from non-viscous bioinks by printing into a bath of gelatin microgels, which provides a temporary support.[173] Strategies using microgels themselves as the bioink can also be envisioned. Several papers have reported that the jamming properties of microgels make them injectable into *in vivo* tissue cavities, indicating that they can be extruded with low shear forces, and further annealed into MAP hydrogels.[63, 67, 76, 99, 174] We recently applied thiol-ene click chemistry to this paradigm for hydrogel synthesis.[101] Specifically, we showed that thiol-ene click chemistry could be leveraged to produce PEG microgels bearing unreacted norbornene groups, which could subsequently be annealed with a PEG-di-thiol linker via a second thiol-ene click reaction. We also demonstrated cell incorporation with high viability after annealing and showed that hMSCs could spread, proliferate, and activate mechanosignaling pathways in response to the physicochemical properties of the PEG microgels. Based on these results, we believe that our clickable PEG microgels could be useful as a bioink for 3D printing.

The objective of this study was to evaluate the utility of clickable PEG microgels for 3D bioprinting. To this end, we used an electrospraying apparatus to produce batches of PEG hydrogel microspheres with varying size and physicochemical properties. We then optimized printing parameters for the microgel bioink to achieve consistent extrusion and printing of 3D structures. Because the PEG microgels contained unreacted norbornene groups, bis-thiol crosslinker and photoinitiator solutions were added onto the printed structure, and printed constructs were annealed to provide long-term stability. Controlled microgel patterning of the printed structure was also explored as a benefit of this bottom-up strategy, and 3D anatomically sized shapes were printed to further demonstrate the utility of our microgel bioink. Finally, hMSCs were incorporated in the microgel bioink during bioprinting to evaluate cytocompatibility of the process.

Materials and Methods

Materials

Four-arm PEG-Nb macromers were synthesized from PEG-hydroxyl precursors (JenKem Technology, 5, 10, and 20 kDa) by esterification with 5-norbornene-2-carboxylic acid (Alfa Aesar) and diisopropyl carbodiimide (Alfa Aesar), as previously described by Jivan *et al.*.[79] The percent functionalization of PEG-Nb was greater than 95% determined by 1H NMR spectroscopy analysis. PEG-DT (3,400 Da) crosslinker was purchased from Laysan Bio. LAP was synthesized following the methods of Fairbanks *et al.* without modification and verified by 1H NMR spectroscopy and electrospray ionization mass spectrometry prior to use.[77] The cell adhesive peptide CGRGDS was prepared via microwave-assisted solid phase peptide synthesis and standard Fmoc methods. Peptide identity was verified using matrix-assisted laser desorption-ionization time-of-flight mass spectrometry.

Microgel Electrospraying

PEG microgel electrospraying setup was similar to the previously reported approach.[80] Based on the gel table (Table V-1), PEG-Nb and PEG-DT were mixed off-stoichiometrically so that 25% excess norbornene groups were available for further photocrosslinking of microgels. The mixed precursor solutions were electrosprayed into a bath of light mineral oil with Span 80 (0.5 wt%) and photopolymerized into microgels with UV irradiation (60 mW/cm^2, 365 nm). The UV light was kept on for 2 minutes after all precursor solutions were sprayed. The microgels were rinsed with 1X phosphate buffered saline three times and centrifuged at 4,400 rpm for 5 minutes to remove the mineral oil. The microgels were stored in PBS at 4 °C and allowed to reach equilibrium swelling before use.

Microgel Characterization

The morphology of the microgels was observed by confocal microscopy (FV1000, Olympus). For visualization, they were labeled with Alexa Fluor 488 N-hydroxysuccinimide ester dye through amide linkage to CGRGDS peptide for 2 h at 4 ºC. The size of microgels was measured from fluorescent images using ImageJ software, and 50-100 microgels were examined for each group. Microgel pellets were also cryo-sectioned into 25 µm slices, and the Young's Modulus of the microgels was tested by atomic force microscopy (Dimension Icon, Bruker) with a SiO_2 colloidal probe (5 µm diameter, spring constants 0.6 N/m; Novascan).

3D Printing of Microgels

Printed shapes were designed in Solidworks and exported as STL files. STL files were loaded into Slic3r Prusa Edition 1.31.6 to customize printing options and converted into G-code printer instructions. Repetier-Host was used to interface with the 3D printer. The layer height was set to 500 µm, layer width was set at 600 µm, and the print speed was kept at 10 mm/s, or 0.27 mL/min. Pelleted microgel bioink was loaded into a 3 mL syringe and inserted into an extrusion tube. It was then extrusion printed through an I3 RepRap printer. Two nozzle tip sizes, 840 and 600 µm, were studied for microgel extrusion. Because the adhesive forces between the microgels could cause tearing as the print head moved, we manually added one drop of aqueous solutions onto printed structures every 10 layers. A 3 cm diameter honeycomb and a hollow 2 cm tall x outer diameter 10 mm and inner diameter 8 mm cylinder was printed from the microgel bioink. The microgel bioink was labeled with fluorescein N-hydroxysuccinimide ester to visualize printed structures. An ear shape was printed with length of 4 cm, width of 2.7

cm, and height of 0.7 cm. A nose shape was printed with length of 3.5 cm, width of 2.3 cm, and height of 1.4 cm. The infill density of ear and nose printing is 60%.

Thiol-ene Click Annealing of Printed Structures

PEG-DT and LAP solutions were pipetted onto printed structures, which were then photopolymerized under UV irradiation (60 mW/cm^2, 365 nm, 3 min) to link the microgels together. The storage modulus of printed microgel disks was measured before and after photopolymerization on a rheometer (Physica MCR 301, Anton Paar) under a time sweep at 1% strain and 1 rad/s. The weight and diameter of microgel disks were also measured at different time points to compare the swelling properties with bulk hydrogels.

hMSC Culture and Printing

hMSCs (P1) were purchased from the Institute for Regenerative Medicine at Texas A&M University and expanded in low-glucose Dulbecco's modified Eagle's medium with 10% fetal bovine serum, 50 U/ml penicillin, 50 µg/ml streptomycin and 1 ng/ml fibroblast growth factor (Sigma) at 37 ºC and 5% CO_2 in a humidified environment. hMSCs were used up to passage 5. In the experiments characterizing the effects of microgel properties on cell-material interactions, hMSCs (5×10^5 cells per well) were cultured with microgels in 24-well ultra-low binding plates (Costar) and allowed good mixture with gentle shaking at 20 rpm for first 2h. Cell-culture plates were then removed from shaker and cultured for another 22h. Samples were fixed using 4%

formaldehyde for 15 min at room temperature. The amount of vinculin was assessed as an indicative of focal adhesion by immunohistochemistry utilizing antibodies against anti-vinculin (1:1000, EMD Millipore). Goat anti-mouse fluorescein (1:100, Jackson ImmunoResearch) was used as fluorescent secondary antibody to visualize the location of the primary antibody. Cytoskeletal staining was performed using rhodamine phalloidin (1:40, Invitrogen) with counter staining of DAPI (1:1000, Biolegend). Quantification of vinculin amount was performed on images captured at 20X magnification using Image-J software. The Threshold and Analyze Particles functions were used to determine total vinculin amount per cell in maximum intensity Z-projection images. At least 50 cells were measured per group. Student's t-test was used to determine significant differences between two groups. Significance is indicated by * corresponding to $p < 0.01$.

For the printing experiment, an hMSC suspension (5×10^6 cells/mL) was mixed with microgels for 30 mins before adding into extrusion tube. The extrusion printing method was similar as described above and a 4-layer honeycomb shape was printed. hMSC viability in the printed structure was assessed at 1, 5, and 10 days using Live/dead kit (L3224, Invitrogen) and confocal microscope (FV1000, Olympus). Quantification of viability was performed using Image-J software, and at least 200 cells were calculated for each group.

Results and Discussion

Production of Microgel Bioinks by Electrospraying

In order for microgel printing to be feasible, the microgel fabrication method should be amenable to producing large batches of microgels with tunable properties. To address this challenge, we utilized electrospraying to prepare PEG microgels, as we were able to employ large flow rates up to 12 mL/h, which was more suitable for producing large-scale batches needed for bioprinting compared to other microgel synthesis methods, such as microfluidics.[63, 80, 175] In addition, we chose thiol-ene click chemistry to crosslink the PEG microgels, as this strategy enables us to easily tune the physicochemical properties of the microgels, control the stoichiometry, and also offers fast reaction kinetics.[77, 149, 176] This allows for immediate gelation after electrospraying to stabilize the droplets, unlike other click reactions, such as thiol-Micheal addition and strain-promoted azide-alkyne crosslinking. During electrospraying, off-stoichiometric non-viscous PEG precursor solutions were sprayed into small droplets from a blunted needle submerged in mineral oil and photocrosslinked immediately upon UV irradiation (Figure V-1a). This approach resulted in norbornene bearing PEG microgels, which is important because it enables us to use a second thiol-ene reaction to anneal and strengthen a 3D printed microgel structure.

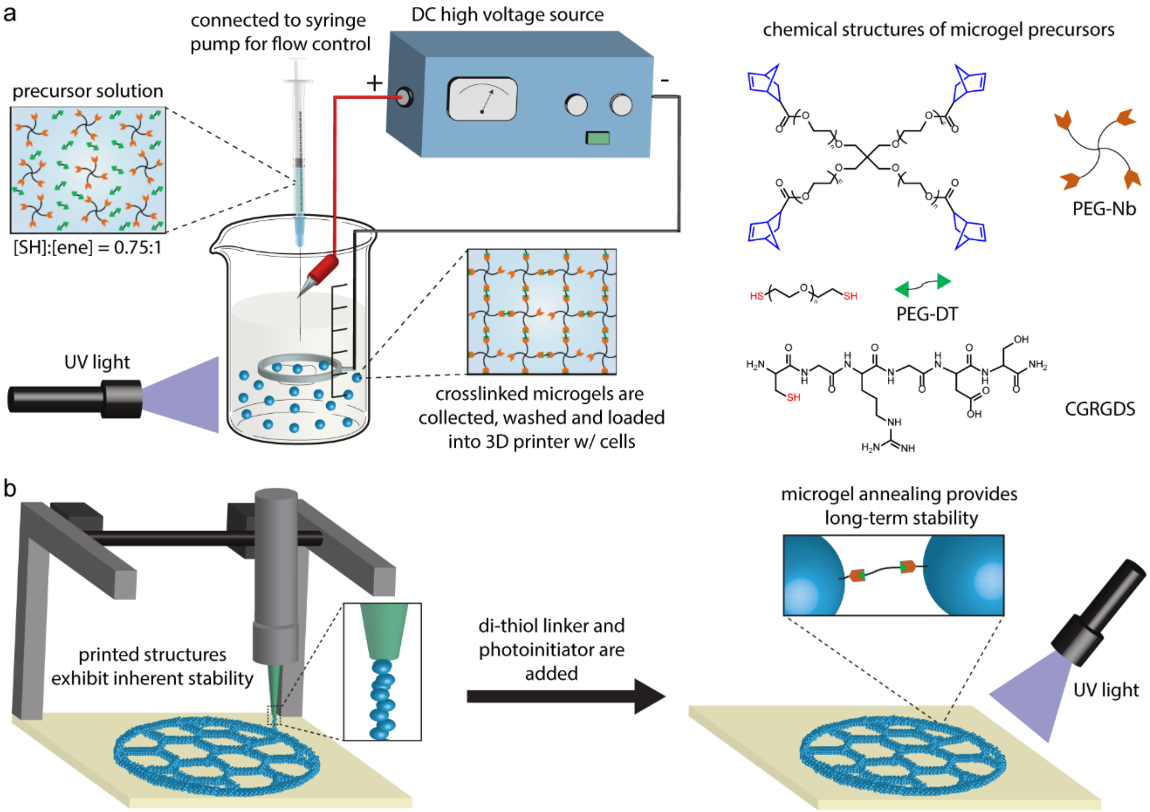

Figure V-1. Overview of clickable PEG microgel bioink production and use in 3D printing. a) Chemical structures and schematic of the submerged electrospraying setup for synthesizing PEG microgels via thiol-ene click chemistry. b) Schematic of PEG microgel 3D printing procedure. Printed structures exhibit inherent stability due to the cohesive forces between PEG microgels. Long-term stability is achieved by annealing the microgels with a second thiol-ene reaction that crosslinks the microgels. Reprinted with permission from Xin *et al.*, 2019, *Biomaterials Science*, 7 (3), 1179-1187, The Royal Society of Chemistry.

The average sizes of electrosprayed microgels from varying electrospraying parameters and properties of precursor solutions were characterized by microscopy and image analysis software (Figure V-2). Voltage, flow rate, tip-to-grounded ring distance, and needle gauge were studied, as well as molecular weight of PEG-Nb (resulting in various viscosity). 5, 10, and 20 kDa PEG-Nb were used to prepare microgels and termed PEG5, PEG10, and PEG20, respectively. As we tune the stiffness of microgels by adjusting molecular weight of PEG-Nb, it is important to have comprehensive size characterization data so that we can choose appropriate parameters for manufacturing desirable sized microgels with varying stiffness. Figure V-2a demonstrates an overall decreasing size trend with increasing voltage. The applied electric field could affect the shape of the induced Taylor cone and liquid jetting. Low voltage did not help to form a sharp Taylor cone and the resulting microgels were much larger. In addition, Figure V-2b-c presents an increasing size trend with increasing flow rate while decreasing needle gauge. Both conditions would also influence the formation of the Taylor cone and, thus, the size of resulting microgels. However, the tip-to-grounded ring distance did not affect the average size of microgels (Figure V-2d), which indicated that the submerged oil environment provided a stable and consistent electric field independent of distance. Figure V-2e shows that the average size of microgels increased when using larger molecular weight PEG-Nb. As indicated in the gel table (Table V-1), PEG20 precursor solutions contained less crosslinker and, thus, had a lower viscosity compared to PEG5 and PEG10. Therefore, formation of the Taylor cone was hindered under the same voltage conditions, because of the high fluidity resulting in larger average microgel sizes. Fluorescence microscopy imaging of Alexa Fluor 488-labeled microgels further verified the difference in size distribution resulting from varying conditions. It is notable that all groups show a wide size distribution with roughly 30% standard deviation. However, this does not impair their utility in 3D printing as the main purpose of using these microgels is to provide structural integrity of printed constructs.

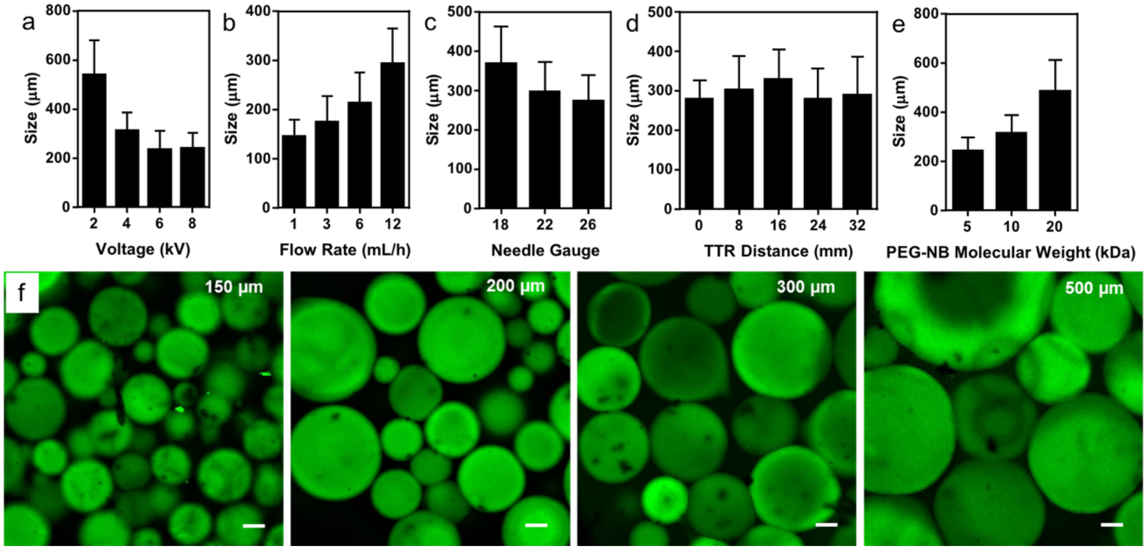

Figure V-2. Electrosprayed PEG microgel bioink size is controlled by varying electrospraying parameters and PEG molecular weight. Size distributions of microgels fabricated by varying a) voltage, b) flow rate, c) needle gauge, d) tip-to-ring distance, and e) molecular weight of PEG-Nb. The fixed parameters were 4 kV voltage, 12 mL/h flow rate, 22 needle gauge, and 16 mm TTR distance. f) Representative fluorescence images of microgels with different sizes (approximate average size is noted). Microgels were labeled by Alexa Fluor 488-succinimidyl ester dye. Scale bars are 50 μm. Reprinted with permission from Xin *et al.*, 2019, *Biomaterials Science*, 7 (3), 1179-1187, The Royal Society of Chemistry.

Before proceeding to printing experiments, we cultured hMSCs on PEG microgels with varying biophysical and biochemical properties to evaluate the effects of bioink properties on cell-material interactions (Figure V-3). hMSCs were allowed to interact with microgels in a low-binding plate. Microgels were prepared with and without RGD cell-adhesive peptide and with varying stiffness by adjusting the molecular weight of PEG-Nb. The results showed hMSCs could attach and spread on RGD-presenting microgels, whereas they tended to aggregate into cell clusters and did not interact with microgels lacking RGD (Figure V-3a and V-8). Furthermore, the Young's modulus of microgels were characterized by nanoindentation with atomic force microscopy (Figure V-3b). hMSCs tended to spread more on the surface of stiffer microgels compared to softer microgels (Figure V-3c). In addition, hMSCs exhibited larger amount of vinculin staining when seeded onto stiffer microgels, which was an indicative of higher focal adhesion formation (Figure V-3d and V-9). Collectively, these results indicated that the physicochemical properties of the microgels can be tuned to modulate cell behavior, which could be potentially leveraged during 3D bioprinting.

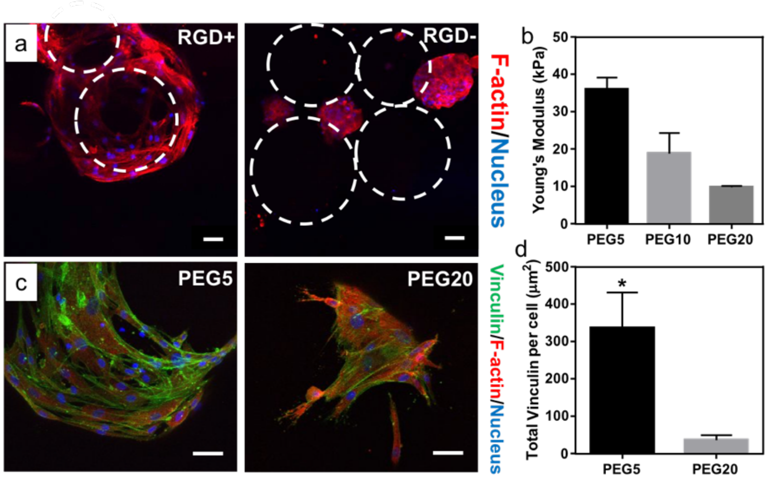

Figure V-3. hMSCs show varied responses on microgels with tunable properties. a) Fluorescence microscopy images showing hMSC adhesion on microgels with and without the RGD peptide. b) Mechanical properties of microgels prepared with varying molecular weight of PEG-Nb and measured by AFM. c) hMSC spreading morphology and d) vinculin quantification on microgels with varying modulus. Scale bars are 50 μm. Significance is indicated by * corresponding to $p < 0.01$. Reprinted with permission from Xin *et al.*, 2019, *Biomaterials Science*, 7 (3), 1179-1187, The Royal Society of Chemistry.

Printability of Microgel Bioinks

To evaluate microgel printability, we loaded a batch of electrosprayed microgels into a 3 mL syringe, which was then installed onto an extrusion-based 3D printer, as shown in Figure V-1b. The motor-driven 3D printer used here is a low-cost setup that can precisely extrude microgels based on volume. The printability of the microgel bioink was studied and optimized from 1D filament extrusion, followed by 2D honeycomb printing, and lastly 3D cylinder printing (Figure V-4). Since the microgel size would alter the required printing parameters, such as nozzle size and extrusion rate, we utilized only 200 µm sized PEG5 microgels from the set of electrospraying parameters characterized above to demonstrate the general approach of microgel printing.

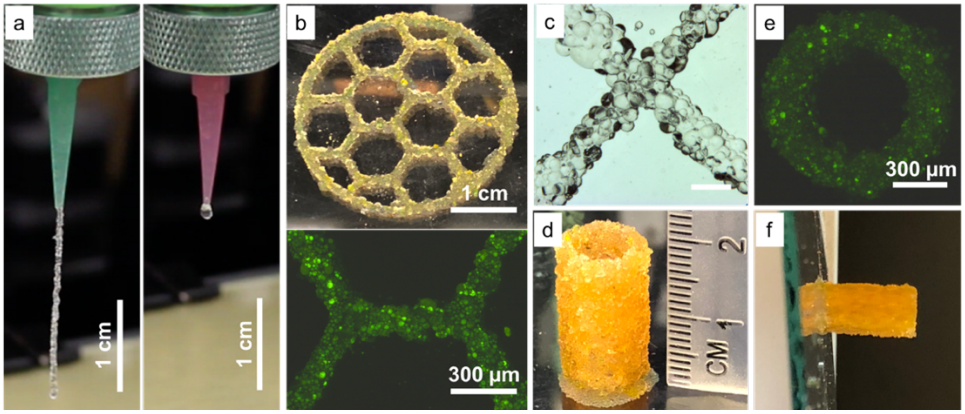

Figure V-4. Optimized printing parameters achieve consistent microgel bioink extrusion and cohesive constructs with mechanical stability. a) A vertical filament of microgel bioink extruded using varying nozzle sizes. The inner diameters of the green and pink nozzles were 840 and 600 µm, respectively. b) Three-layer honeycomb printing with a fluorescent zoom-in image. c) Stereomicroscopy image showing an intersection point of two microgel filaments. Scale bar is 600 µm. d) Cylindrical shape printing with 1 cm outer diameter and 0.8 inner diameter illustrating microgel printing can achieve 20 mm in height. e) Fluorescent image showing top view of the printed cylinder. f) Printed cylinder on a tilted glass (85º) without falling demonstrating outstanding stability of microgel printing. Reprinted with permission from Xin *et al.*, 2019, *Biomaterials Science*, 7 (3), 1179-1187, The Royal Society of Chemistry.

First, a microgel extrusion study was performed to form a vertical line hanging from two different sized nozzles (Figure V-4a). The inner diameters of the large and small nozzles were 840 and 600 μm, respectively. The microgels formed a continuous line and extruded consistently from the large nozzle. The extruded filament from the large nozzle was also consistently 3 cm long before dropping due to gravity. In contrast, when the smaller nozzle was used, the extrusion was uneven and some microgels became stuck during extrusion. Thus, we concluded that the nozzle size needs to be at least 4-fold larger than the average size of the microgels to achieve consistent extrusion.

Second, 2D honeycomb-shape printing was performed to test whether the extrusion would be continuous when the nozzle was moving during printing (Figure V-4b). An intact three-layer honeycomb structure was successfully printed when microgels were extruded. A quantification of width variability on the entire honeycomb construct has been performed by analyzing 50 different locations and the average width is 779 μm with a standard deviation of 140.7 μm. This is due to the large size of microgels and the extruded filaments could have slightly inconsistent width. In addition, a magnified view of an intersection point between two lines is provided to demonstrate that microgel printing produces filaments with clean overlap on each other (Figure V-4c).

Next, we tested the Z-axis structural integrity and stability of microgel structures by printing a 1 cm diameter cylindrical shape (Figure V-4d and V-10, a high aspect ratio structure). The images showed that microgel printing was able to achieve a cylindrical shape with a clean ring structure from the top view (Figure V-4d and e). Remarkably, the microgel printed structure exhibited excellent stability and could support a height of 2 cm (40 layers) without collapsing, which was at least twice as high as previously reported literature on printing of non-viscous materials without using supporting gels.[133, 177] Moreover, the printed cylinder did not fall when we titled the glass surface it was printed on by 90˚ (Figure V-4f), demonstrating outstanding stability and strong adhesion between microgels. While Highley et al. recently demonstrated high printing fidelity of monodispersed microgel ink with smaller size,[174] our polydispersed microgel ink exhibit excellent 3D stability due to the inherent cohesive forces, which is needed to print anatomically sized tissues and organs. This trade-off will be further studied in future to optimize the parameters of microgel ink for various applications.

While multi-layer structures could be fabricated due to the natural cohesiveness of the microgels, the clickable nature of the microgels enables annealing to confer long-term stability to the construct. To this end, we added a mixture of PEG-DT linker and photoinitiator to the constructs during printing and then applied UV irradiation to anneal the microgels via their unreacted norbornene groups (see Section 2.1). Storage modulus measurements via rheology on printed disk-shaped microgel structures showed a 1.6-fold increase in modulus after UV annealing (Figure V-5a), which verified that the printed microgel structure was strengthened and connected as an intact construct. Importantly, the crosslinked constructs also exhibited excellent geometric stability after annealing due to their non-swelling nature, since the microgels were allowed to swell at equilibrium before printing (Figure V-5b-c). This feature could be important for the development of geometrically constrained structures, such as tubular channels.[112] Future work will investigate this possibility, as well as the possibility of using smaller sized and more monodispersed microgels to print constructs with refined structures.

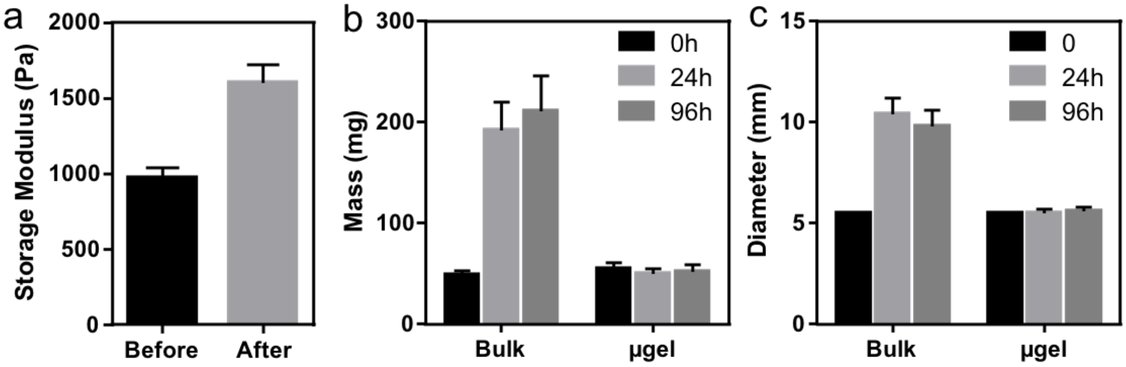

Figure V-5. Crosslinked constructs from microgel bioinks exhibit enhanced mechanical properties and non-swelling properties. a) Storage modulus of printed microgel disks before and after photopolymerization. The swelling properties were compared between bulk hydrogel and microgel printed disks as measured in b) mass and c) diameter. Reprinted with permission from Xin *et al.*, 2019, *Biomaterials Science*, 7 (3), 1179-1187, The Royal Society of Chemistry.

3D Printing Complex and Cell-laden Structures

We also explored using our microgel bioink to print geometrically complex and anatomically relevant 3D structures. Figure V-6a shows an anatomically sized 3D printed ear from our microgel bioink, which exhibited high fidelity and stability even without secondary crosslinking. The helix of the printed ear demonstrates the overhang structure in the ear, further illustrating the outstanding stability from the cohesive forces between microgels. Figures V-6b and V-11 present an anatomically sized 3D printed nose from our microgel bioink. The clean curve on the surface of the nose and the precise shape of nostril further verify the high printability of our microgel bioink and its utility for producing anatomically relevant tissue structures. A comparison of overall dimensions and special features for both ear and nose printing has been performed in Figure V-6c. Both printed structures are roughly 5% larger in any dimension than the designed shape, which meets the successful criteria of 3D printing. The reason for this 5% error is possibly due to the slightly high infill density, which is intended to ensure a consistent flow of microgel bioink during printing. Although we did not explore it here, additional complexity could be easily achieved by leveraging the modularity of the microgels. Distinct formulations of microgels with different stiffness or presenting different chemical ligands could be combined in a multi-layered construct either randomly or with spatial control to recapitulate native tissue structures and direct cellular behavior within the materials.

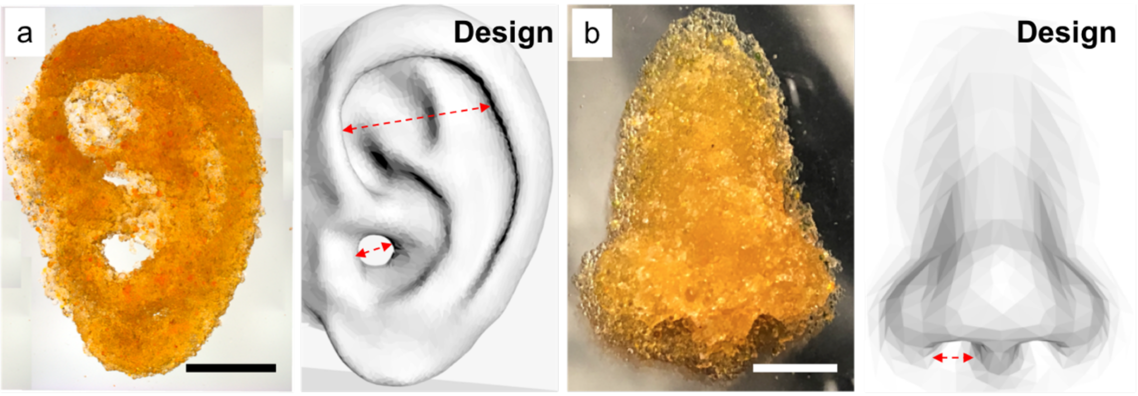

c	Ear			Nose	
	Dimension (cm, L × W × H)	Helix (cm)	Canal (cm)	Dimension (cm, L × W × H)	Nostril (cm)
Designed Value	4 × 2.7 × 0.7	1.31	0.41	3.5 × 2.3 × 1.4	0.42
Actual Value	4.15 × 2.85 × 0.719	1.35	0.46	3.5 × 2.49 × 1.48	0.42

Figure V-6. Complex and anatomically relevant 3D structures can be produced with the PEG microgel bioink. a) A 3D printed ear shape from microgel bioink showing mechanical stability and high fidelity. b) A 3D printed nose shape from microgel bioink showing mechanical stability. The microgels were labeled with fluorescein and appear orange color. The scale bars are 1 cm. c) Table of comparisons of overall dimensions and special features for both ear and nose printing. Special features were measured as labelled double arrow line. Reprinted with permission from Xin *et al.*, 2019, *Biomaterials Science*, 7 (3), 1179-1187, The Royal Society of Chemistry.

Finally, to test cytocompatibility, we incorporated hMSCs with our microgel bioink to print a multi-layered honeycomb structure. For this experiment, hMSCs were incubated with PEG5 microgels for 30 minutes, after which they were transferred to the extrusion syringe for printing. A four-layer honeycomb shape was chosen as a fiber-assembled structure for hMSC-incorporated printing, which potentially leads to uneven continuous matrix-like structure after secondary crosslinking for tissue engineering applications. The viability of hMSCs in the printed honeycomb shape were evaluated by

Live/Dead staining and fluorescence microscopy (Figure V-7). Figure V-7a shows a representative image of hMSCs growing in a corner of one hexagon after 5 days, and the cells exhibit excellent spreading and viability. Quantitative analysis of the Live/Dead staining indicated that the hMSC viability exceeded 88% at 1 hour, 80% at 1 day and 90% at 5 and 10 days (Figure V-7b), which is identical with our previous data on cell incorporation in microgel-based scaffolds,30 indicating that cell viability was not compromised by harmful shear forces during microgel extrusion. In addition, while microgel bioink could be degradable by incorporating enzymatically-degradable peptide crosslinker, the hMSCs continued to proliferate during culture in non-degradable microgel printed structures due to the microporosity (Figure V-7c). These results verified that our microgel bioink exhibits good cytocompatibility and is suitable for 3D bioprinting.

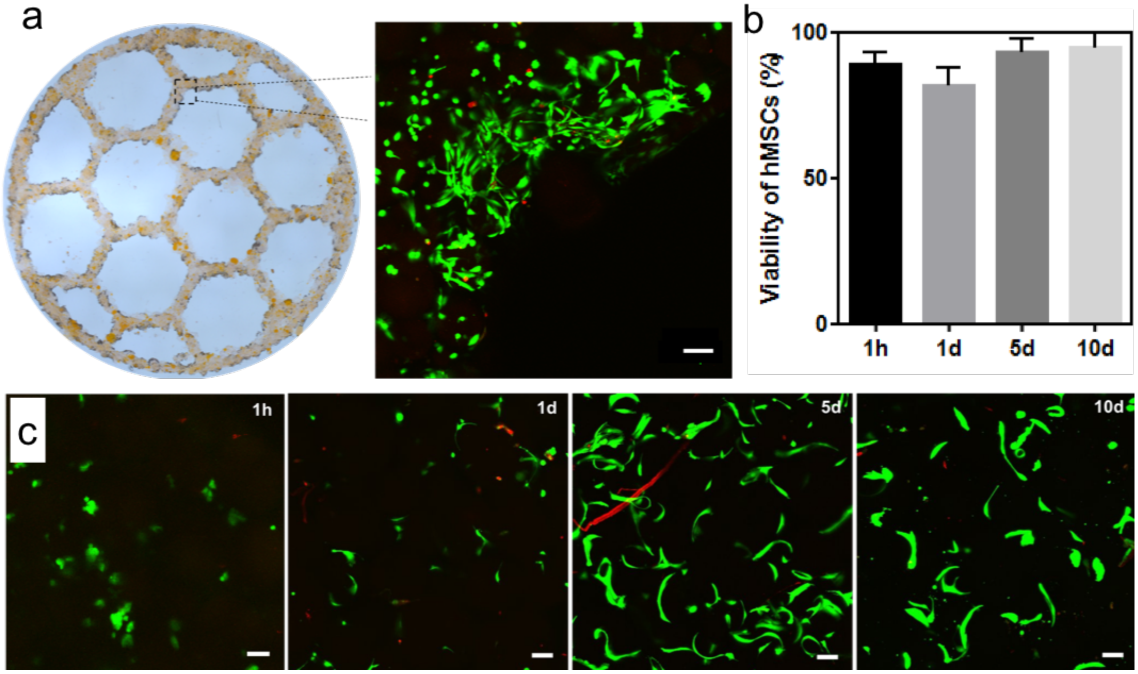

Figure V-7. Microgel bioink printing and annealing are cytocompatible. a) Z-projection image of Live/dead stained hMSCs growing at a corner of hexagon in a bioprinted honeycomb shape 5 days after printing. The Z-stack depth is 500 µm (scale bar = 100 µm). b) Quantitative data of hMSC viability after microgel bioprinting. c) Z-projection images of Live/dead stained hMSCs cultured in microgel printed disks at 1 hour, 1, 5, and 10 days. The Z-stack depths are 200 µm (scale bars = 50 µm). Reprinted with permission from Xin *et al.*, 2019, *Biomaterials Science*, 7 (3), 1179-1187, The Royal Society of Chemistry.

Conclusion

We report here a novel PEG microgel-based bioink for 3D printing. The microgels, which are produced by electrospraying and off-stoichiometric thiol-ene click chemistry, can be easily extruded and quickly stabilize after extrusion due to inherent cohesive forces between the microgels, thereby permitting the formation of complex and anatomically relevant 3D structures. Moreover, owing to the presence of unreacted norbornene groups, they can be annealed via a second thiol-ene click reaction to impart long-term stability, and the entire process is cytocompatible. Based on these results, clickable microgel bioinks could be a promising platform for large-scale artificial tissue or scaffold fabrication. Toward this goal, future studies should determine optimal printing parameters for other clickable PEG microgel formulations beyond what was studied here. The ability to guide cell patterning within microgel printed structures for specific applications and tissue types should also be explored.

Supporting Information

Table V-1. Concentrations (m*M*) of each component in PEG thiol-ene (0.75:1) precursor solutions for microgel preparation.

	PEG5	PEG10	PEG20
PEG-Nb	18.248	9.542	4.883
PEG-DT	26.872	13.813	6.824
LAP	2	2	2
CGRGDS	1	1	1

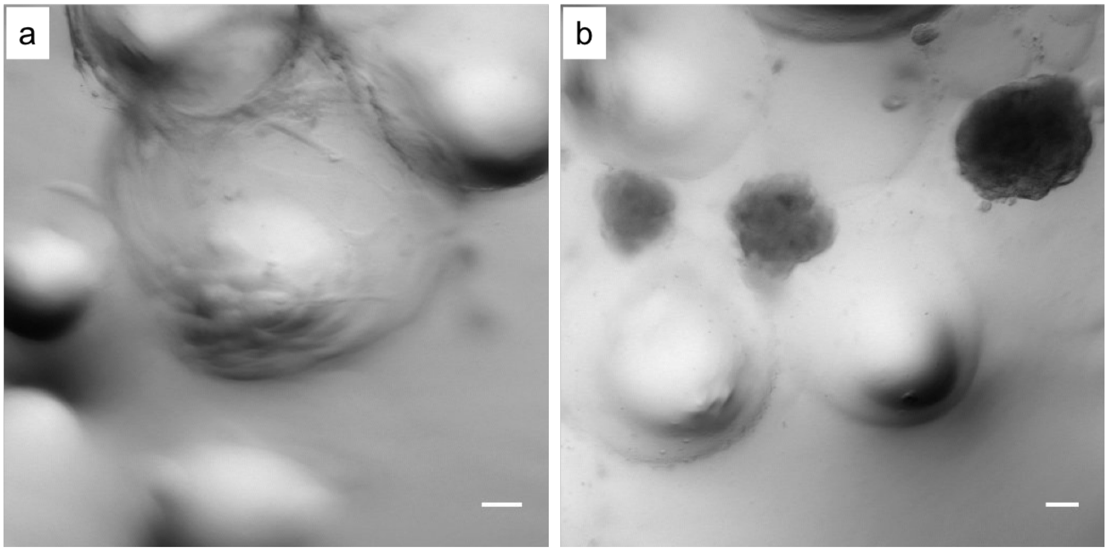

Figure V-8. Bright field views for Figure 3a showing the positions of microgels. Scale bars are 50 µm. Reprinted with permission from Xin *et al.*, 2019, *Biomaterials Science*, 7 (3), 1179-1187, The Royal Society of Chemistry.

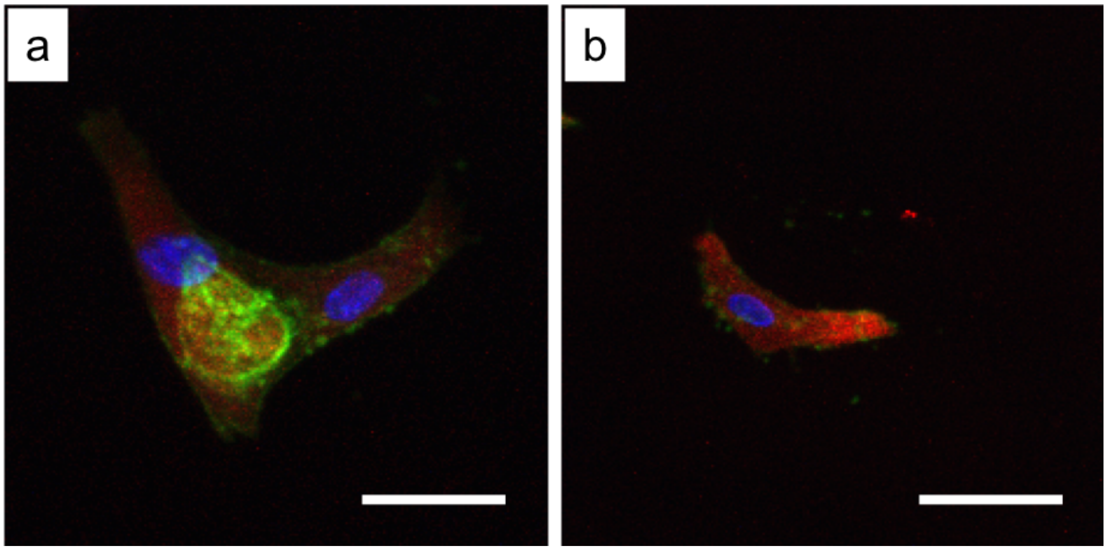

Figure V-9. Representative 20X Z-projection images of hMSCs grown on a) PEG5 and b) PEG20 microgels. Green = vinculin, red = F-actin, and blue = nucleus. Scale bars are 50µm. Reprinted with permission from Xin *et al.*, 2019, *Biomaterials Science*, 7 (3), 1179-1187, The Royal Society of Chemistry.

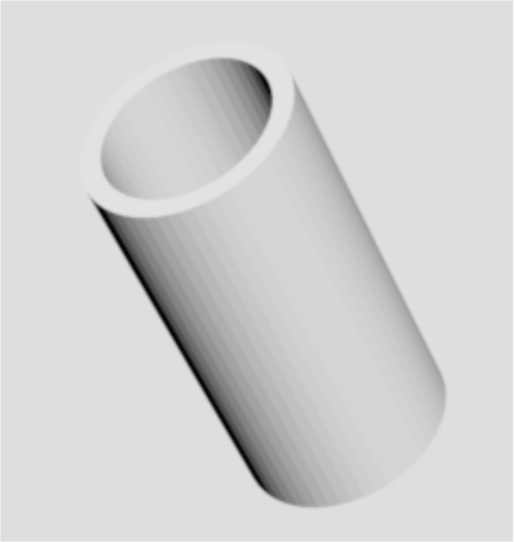

Figure V-10. Design image in STL files for cylinder shown in Figure V-4d. Reprinted with permission from Xin *et al.*, 2019, *Biomaterials Science*, 7 (3), 1179-1187, The Royal Society of Chemistry.

Figure V-11. Additional image of nose print from a side view. Reprinted with permission from Xin *et al.*, 2019, *Biomaterials Science*, 7 (3), 1179-1187, The Royal Society of Chemistry.

CHAPTER VI

CONCLUSIONS AND FUTURE RECOMMENDATION

Conclusions

Thiol-ene based microporous annealed particle (MAP) hydrogels were successfully prepared by first generating norbornene-bearing poly(ethylene glycol) (PEG) microgels and then assembling them with the addition of a bis-thiol linker. When human mesenchymal stem cells (hMSCs) were embedded in the pore space of MAP hydrogels, they showed superior spreading compared to cells encapsulated in conventional nanoporous bulk hydrogels. But low linker concentration between microgels was the key for enhanced cell spreading. These results indicate that these MAP hydrogels are a suitable platform for 3D cell culture.

The fact that embedded cells interact with the internal microgel surface renders some features of 2D culture in these 3D scaffolds. Thus, well-established knowledge of cell-material interactions in 2D cultures can be utilized to instruct cell behaviors in MAP hydrogels. The impact of stiffness, degradability, and functionalization with specific integrin-binding peptides was investigated. First, hMSC spreading was regulated by activating mechanotransduction signaling as response to microgel stiffness, which was similar to the results in 2D cultures. Next, long-term proliferation and extracellular protein deposition were significantly enhanced in degradable MAP scaffolds. Evidences also suggested cell-mediated microenvironment remodeling occurred on microgel surface during degradation. Last, the paracrine secretion of hMSCs was mediated by integrin-binding ligand, as cells cultured in c(RRETAWA)-functionalized MAP hydrogels, which specifically binds to α5β1 integrins, increased secretion of the osteogenic proteins bone morphogenetic protein-2 and osteoprotegerin compared to cells within RGD-functionalized group. But these paracrine activities also depended critically on the susceptibility of the MAP hydrogels to degradation. These findings suggest MAP hydrogels are promising cell-instructive scaffolds for therapeutic cell delivery.

The therapeutic outcomes of degradable MAP hydrogels were then evaluated in mouse femoral defect model. Although the incorporated cells did not improve the bone healing compared to cell-free groups, MAP hydrogel groups showed on average 3-fold increase in new bone volume compared to no treatment control. This suggests the interconnect pore structure can induce the infiltration of endogenous cells. From these studies, we established MAP hydrogels are a promising platform for tissue regeneration, but further work is needed to improve their utility for therapeutic cell delivery.

The modularity of MAP hydrogels was also leveraged to generate physicochemical gradients. A novel droplet microfluidic method was developed by incorporating a mixer module. By programming the relative flow rates in the mixer module over time, microgels with varying formulations were generated and packed layer-by-layer to produce microgel gradients. These gradients were successfully maintained after injection and assembly. Cell culture results suggested gradient MAP hydrogels gave more insights on cell-material interactions by having a range of continuous parameters. This platform can be promising for screening cell-material interactions.

The ability of microgel building blocks to construct MAP hydrogels with various shapes was demonstrated by 3D printing. Microgels were easily extruded and exhibit outstanding stability in Z-direction after extrusion due to inherent cohesive forces between the microgels. These microgels supported 2 cm height of printed constructs, making it possible to print most anatomically relevant structures, such as ear and nose. The printed constructs were further strengthened into MAP hydrogels via microgel assembly. The entire process was cytocompatible, and hMSCs spread well within these printed structures.

Future Recommendation

Biomaterial scientists develop dynamic and microporous hydrogels to overcome the physical confinement of cells in conventional nanoporous hydrogels from two different perspectives. The rationale for dynamic hydrogels is to recapitulate the dynamic remodeling feature in native ECM. Microporous hydrogels, which is the focus of this dissertation work, allow the independent tuning of physicochemical properties from degradability or viscoelastic properties and, thus, are more suitable as cell-instructive scaffolds. However, we think both should be considered when designing hydrogels for therapeutic cell delivery. Integrating both dynamic and microporous features into one system is a potential road for the future. The work in Chapter III has demonstrated the crucial role of substrate degradability in microporous hydrogels on cell behaviors, which suggests this may be the right direction to improve the efficacy of hydrogel-based cell delivery. But more questions need to be answered, such as the detailed mechanism on how cells contract microgels in MAP hydrogels and whether these tractions will influence cell fate and activities. In addition, it is important to recapitulate the structural features in native ECM when designing a new generation of MAP hydrogels. Microgel building blocks can be different geometries other than spheres, which may better mimic native ECM. The pore structures can also be optimized by altering microgel shape to maintain high interconnectivity and exclude large, unnecessary voids. These changes can potentially lead to improved cell culture outcomes.

Since the *in vivo* results in Chapter III did not show a significant effect of incorporating hMSCs, the osteogenic potential of the cells within MAP hydrogels needs to be further improved. This can be possibly achieved by providing the cells osteogenic stimulus before transplantation. Alternatively, the modulus of the MAP hydrogels can be further increased. Current Young's modulus of the formulation used in the *in vivo* study is less than 10 kPa, which is lower than reported values that induce osteogenesis. The modulus can be improved by increasing crosslinking density in microgels.

However, it is promising that MAP hydrogels alone can induce such significant new bone growth, indicating the infiltration of endogenous cells from surrounding tissue can be enhanced by MAP hydrogels due to the interconnected pore structures. If the materials alone can work, it simplifies the procedure by omitting the hMSCs. Therefore, future work should also focus on new material design within MAP hydrogels that can further promote cell infiltration. The gradient MAP hydrogels developed in Chapter IV can be potentially used here, as certain physicochemical gradients may stimulate cell migration towards the degeneration sites. The microgel size in these gradient MAP hydrogels needs to be further optimized, and the effects of each physicochemical gradients on cell infiltration need to be characterized.

Another potential use of gradient MAP hydrogels is in the regeneration of tissues that naturally exhibit a gradient in features, such as osteochondral defects.[132, 178] Due to the high modularity, osteogenic and chondrogenic microgels can be designed on the two sides of MAP hydrogels. As the results in Chapter IV showed a continuous gradient profile could be achieved in gradient MAP hydrogels, the physicochemical properties of microgels that induce osteogenesis and chondrogenesis can gradually change throughout the hydrogels, which has the potential to facilitate cartilage and bone integration. This is superior to bilayered or lower resolution gradient scaffolds, which often cause uneven cell differentiation around the distinct boundary and failed regeneration. A gradient of porosity can also be achieved by continuously changing the size of microgels within MAP hydrogels, which may also be useful for osteochondral regeneration.[179] However, the bulk mechanical properties of the current MAP hydrogels need to be significantly improved for this application, which can be achieved by increasing the crosslinking density of microgels and linker concentrations between microgels.

Last but not least, we think hydrogel microspheres are a very good candidate as bioinks for 3D printing. The current microgels presented in Chapter V have large diameter (> 200 μm) with high polydispersity, which results in low printing fidelity and crude edges of printed structures. However, this issue can be solved by using small (< 20 μm), monodispersed microgels. These small microgels are still possible to be optimized for good stability. In addition, small microgels can incorporate therapeutic cells for bioprinting. The small size permits extrusion without generating high shear force to keep cells viable. It is also possible to generate heterogeneous patterning of varying cell types via microgel 3D printing.

REFERENCES

1. A.S. Hoffman, *Hydrogels for biomedical applications.* Advanced Drug Delivery Reviews, 2002. **54**(1): 3-12.
2. O. Wichterle and D. Lim, *Hydrophilic gels for biological use.* Nature, 1960. **185**(4706): 117-118.
3. F. Lim and A.M. Sun, *Microencapsulated islets as bioartificial endocrine pancreas.* Science, 1980. **210**(4472): 908-910.
4. C.M. Wang, R.R. Varshney, and D.A. Wang, *Therapeutic cell delivery and fate control in hydrogels and hydrogel hybrids.* Advanced Drug Delivery Reviews, 2010. **62**(7-8): 699-710.
5. C. Loebel and J.A. Burdick, *Engineering stem and stromal cell therapies for musculoskeletal tissue repair.* Cell Stem Cell, 2018. **22**(3): 325-339.
6. A. Trounson and C. McDonald, *Stem cell therapies in clinical trials: progress and challenges.* Cell Stem Cell, 2015. **17**(1): 11-22.
7. J.A. Burdick, R.L. Mauck, and S. Gerecht, *To serve and protect: hydrogels to improve stem cell-based therapies.* Cell Stem Cell, 2016. **18**(1): 13-15.
8. B.G. Ballios, *et al.*, *A hydrogel-based stem cell delivery system to treat retinal degenerative diseases.* Biomaterials, 2010. **31**(9): 2555-2564.
9. M. Liu, *et al.*, *Injectable hydrogels for cartilage and bone tissue engineering.* Bone Research, 2017. **5**: 17014.

10. C.T.W.P. Foo, *et al.*, *Two-component protein-engineered physical hydrogels for cell encapsulation.* Proceedings of the National Academy of Sciences, 2009. **106**(52): 22067-22072.

11. C.C. Lin, A. Raza, and H. Shih, *PEG hydrogels formed by thiol-ene photo-click chemistry and their effect on the formation and recovery of insulin-secreting cell spheroids.* Biomaterials, 2011. **32**(36): 9685-9695.

12. C.A. DeForest, B.D. Polizzotti, and K.S. Anseth, *Sequential click reactions for synthesizing and patterning three-dimensional cell microenvironments.* Nature Materials, 2009. **8**(8): 659-664.

13. D.L. Alge, *et al.*, *Synthetically tractable click hydrogels for three-dimensional cell culture formed using tetrazine–norbornene chemistry.* Biomacromolecules, 2013. **14**(4): 949-953.

14. M. Guvendiren and J.A. Burdick, *Engineering synthetic hydrogel microenvironments to instruct stem cells.* Current Opinion in Biotechnology, 2013. **24**(5): 841-846.

15. D. Seliktar, *Designing cell-compatible hydrogels for biomedical applications.* Science, 2012. **336**(6085): 1124-1128.

16. T. Segura, P.H. Chung, and L.D. Shea, *DNA delivery from hyaluronic acid-collagen hydrogels via a substrate-mediated approach.* Biomaterials, 2005. **26**(13): 1575-1584.

17. A.F. Godier-Furnémont, *et al.*, *Composite scaffold provides a cell delivery platform for cardiovascular repair.* Proceedings of the National Academy of Sciences, 2011. **108**(19): 7974-7979.

18. S.P. Massia and J.A. Hubbell, *Covalent surface immobilization of Arg-Gly-Asp- and Tyr-Ile-Gly-Ser-Arg-containing peptides to obtain well-defined cell-adhesive substrates.* Analytical Biochemistry, 1990. **187**(2): 292-301.

19. D.L. Hern and J.A. Hubbell, *Incorporation of adhesion peptides into nonadhesive hydrogels useful for tissue resurfacing.* Journal of Biomedical Materials Research, 1998. **39**(2): 266-276.

20. J.W. Haycock, *3D cell culture: a review of current approaches and techniques.* Methods in Molecular Biology, 2011. **695**: 1-15.

21. J.A. Burdick and K.S. Anseth, *Photoencapsulation of osteoblasts in injectable RGD-modified PEG hydrogels for bone tissue engineering.* Biomaterials, 2002. **23**(22): 4315-4323.

22. M.B. Evangelista, *et al.*, *Upregulation of bone cell differentiation through immobilization within a synthetic extracellular matrix.* Biomaterials, 2007. **28**(25): 3644-3655.

23. Y. Lei, *et al.*, *The spreading, migration and proliferation of mouse mesenchymal stem cells cultured inside hyaluronic acid hydrogels.* Biomaterials, 2011. **32**(1): 39-47.

24. S.R. Caliari, *et al.*, *Dimensionality and spreading influence MSC YAP/TAZ signaling in hydrogel environments.* Biomaterials, 2016. **103**: 314-323.

25. T. Canal and N.A. Peppas, *Correlation between mesh size and equilibrium degree of swelling of polymeric networks.* Journal of Biomedical Materials Research, 1989. **23**(10): 1183-1193.

26. W.P. Daley, S.B. Peters, and M. Larsen, *Extracellular matrix dynamics in development and regenerative medicine.* Journal of Cell Science, 2008. **121**(3): 255-264.

27. O. Chaudhuri, *et al.*, *Substrate stress relaxation regulates cell spreading.* Nature Communications, 2015. **6**: 6365.

28. K. Ghosh, *et al.*, *Cell adaptation to a physiologically relevant ECM mimic with different viscoelastic properties.* Biomaterials, 2007. **28**(4): 671-679.

29. N. Huebsch, *et al.*, *Harnessing traction-mediated manipulation of the cell/matrix interface to control stem-cell fate.* Nature Materials, 2010. **9**(6): 518-526.

30. O. Chaudhuri, *et al.*, *Hydrogels with tunable stress relaxation regulate stem cell fate and activity.* Nature Materials, 2016. **15**(3): 326-334.

31. L. Cai, R.E. Dewi, and S.C. Heilshorn, *Injectable hydrogels with in situ double network formation enhance retention of transplanted stem cells.* Advanced Functional Materials, 2015. **25**(9): 1344-1351.

32. C. Loebel, *et al.*, *Tailoring supramolecular guest–host hydrogel viscoelasticity with covalent fibrinogen double networks.* Journal of Materials Chemistry B, 2019. **7**(10): 1753-1760.

33. J. Lou, *et al.*, *Stress relaxing hyaluronic acid-collagen hydrogels promote cell spreading, fiber remodeling, and focal adhesion formation in 3D cell culture.* Biomaterials, 2018. **154**: 213-222.

34. K.H. Vining, A. Stafford, and D.J. Mooney, *Sequential modes of crosslinking tune viscoelasticity of cell-instructive hydrogels.* Biomaterials, 2019. **188**: 187-197.

35. S.J. Bryant and K.S. Anseth, *Controlling the spatial distribution of ECM components in degradable PEG hydrogels for tissue engineering cartilage.* Journal of Biomedical Materials Research Part A, 2003. **64**(1): 70-79.

36. C.A. DeForest and K.S. Anseth, *Cytocompatible click-based hydrogels with dynamically tunable properties through orthogonal photoconjugation and photocleavage reactions.* Nature Chemistry, 2011. **3**(12): 925-931.

37. A.M. Kloxin, *et al.*, *Photodegradable hydrogels for dynamic tuning of physical and chemical properties.* Science, 2009. **324**(5923): 59-63.

38. M. Lutolf, *et al.*, *Synthetic matrix metalloproteinase-sensitive hydrogels for the conduction of tissue regeneration: engineering cell-invasion characteristics.* Proceedings of the National Academy of Sciences, 2003. **100**(9): 5413-5418.

39. J.A. Benton, B.D. Fairbanks, and K.S. Anseth, *Characterization of valvular interstitial cell function in three dimensional matrix metalloproteinase degradable PEG hydrogels.* Biomaterials, 2009. **30**(34): 6593-6603.

40. S. Khetan, *et al.*, *Degradation-mediated cellular traction directs stem cell fate in covalently crosslinked three-dimensional hydrogels.* Nature Materials, 2013. **12**(5): 458-465.

41. A.M. Rosales and K.S. Anseth, *The design of reversible hydrogels to capture extracellular matrix dynamics.* Nature Reviews Materials, 2016. **1**(2): 15012.

42. H. Wang and S.C. Heilshorn, *Adaptable hydrogel networks with reversible linkages for tissue engineering.* Advanced Materials, 2015. **27**(25): 3717-3736.

43. D.D. McKinnon, *et al.*, *Biophysically defined and cytocompatible covalently adaptable networks as viscoelastic 3D cell culture systems.* Advanced Materials, 2014. **26**(6): 865-872.

44. B.M. Richardson, *et al.*, *Hydrazone covalent adaptable networks modulate extracellular matrix deposition for cartilage tissue engineering.* Acta Biomaterialia, 2019. **83**: 71-82.

45. S. Tang, *et al.*, *Adaptable fast relaxing boronate-based hydrogels for probing cell-matrix interactions.* Advanced Science, 2018. **5**(9): 1800638.

46. C. Fan and D.A. Wang, *Macroporous hydrogel scaffolds for three-dimensional cell culture and tissue engineering.* Tissue Engineering Part B: Reviews, 2017. **23**(5): 451-461.

47. K.J. De France, F. Xu, and T. Hoare, *Structured macroporous hydrogels: Progress, challenges, and opportunities.* Advanced Healthcare Materials, 2018. **7**(1): 1700927.

48. Y. Gong, *et al.*, *Microcavitary hydrogel-mediating phase transfer cell culture for cartilage tissue engineering.* Tissue Engineering Part A, 2010. **16**(12): 3611-3622.

49. C.M. Hwang, *et al.*, *Fabrication of three-dimensional porous cell-laden hydrogel for tissue engineering.* Biofabrication, 2010. **2**(3): 035003.

50. N. Huebsch, *et al.*, *Matrix elasticity of void-forming hydrogels controls transplanted-stem-cell-mediated bone formation.* Nature Materials, 2015. **14**(12): 1269-1277.

51. E.G. Lima, *et al.*, *Microbubbles as biocompatible porogens for hydrogel scaffolds.* Acta Biomaterialia, 2012. **8**(12): 4334-4341.

52. M.G. Haugh, *et al.*, *Investigating the interplay between substrate stiffness and ligand chemistry in directing mesenchymal stem cell differentiation within 3D macro-porous substrates.* Biomaterials, 2018. **171**: 23-33.

53. A. Ehsanipour, *et al.*, *Injectable, hyaluronic acid-based scaffolds with macroporous architecture for gene delivery.* Cellular and Molecular Bioengineering, 2019. **12**(5): 399-413.

54. D.H. Reneker and A.L. Yarin, *Electrospinning jets and polymer nanofibers.* Polymer, 2008. **49**(10): 2387-2425.

55. J. Bürck, *et al.*, *Resemblance of electrospun collagen nanofibers to their native structure.* Langmuir, 2013. **29**(5): 1562-1572.

56. C. Chen, *et al.*, *Bioinspired hydrogel electrospun fibers for spinal cord regeneration.* Advanced Functional Materials, 2019. **29**(4): 1806899.

57. X. Sun, *et al.*, *Electrospun photocrosslinkable hydrogel fibrous scaffolds for rapid in vivo vascularized skin flap regeneration.* Advanced Functional Materials, 2017. **27**(2): 1604617.

58. X. Zhao, *et al.*, *Cell infiltrative hydrogel fibrous scaffolds for accelerated wound healing.* Acta Biomaterialia, 2017. **49**: 66-77.

59. N.L. Nerurkar, *et al.*, *Nanofibrous biologic laminates replicate the form and function of the annulus fibrosus.* Nature Materials, 2009. **8**(12): 986-992.

60. R.J. Wade, *et al.*, *Protease-degradable electrospun fibrous hydrogels.* Nature Communications, 2015. **6**: 6639.

61. H.G. Sundararaghavan and J.A. Burdick, *Gradients with depth in electrospun fibrous scaffolds for directed cell behavior.* Biomacromolecules, 2011. **12**(6): 2344-2350.

62. E.A. Scott, *et al.*, *Modular scaffolds assembled around living cells using poly(ethylene glycol) microspheres with macroporation via a non-cytotoxic porogen.* Acta Biomaterialia, 2010. **6**(1): 29-38.

63. D.R. Griffin, *et al.*, *Accelerated wound healing by injectable microporous gel scaffolds assembled from annealed building blocks.* Nature Materials, 2015. **14**(7): 737-744.

64. E. Sideris, *et al.*, *Particle hydrogels based on hyaluronic acid building blocks.* ACS Biomaterials Science & Engineering, 2016. **2**(11): 2034-2041.

65. A.S. Caldwell, *et al.*, *Clickable microgel scaffolds as platforms for 3D cell encapsulation.* Advanced Healthcare Materials, 2017. **6**(15): 1700254.

66. A. Sheikhi, *et al.*, *Microfluidic-enabled bottom-up hydrogels from annealable naturally-derived protein microbeads.* Biomaterials, 2019. **192**: 560-568.

67. J.E. Mealy, *et al.*, *Injectable Granular Hydrogels with Multifunctional Properties for Biomedical Applications.* Advanced Materials, 2018. **30**(20): 1705912.

68. Y. Jiang, *et al.*, *Click hydrogels, microgels and nanogels: emerging platforms for drug delivery and tissue engineering.* Biomaterials, 2014. **35**(18): 4969-4985.

69. R. Cruz-Acuna and A.J. Garcia, *Synthetic hydrogels mimicking basement membrane matrices to promote cell-matrix interactions.* Matrix Biology, 2017. **57-58**: 324-333.

70. X. Zhao, *et al.*, *Photocrosslinkable gelatin hydrogel for epidermal tissue engineering.* Advanced Healthcare Materials, 2016. **5**(1): 108-118.

71. M.F. Cutiongco, *et al.*, *Planar and tubular patterning of micro and nano-topographies on poly (vinyl alcohol) hydrogel for improved endothelial cell responses.* Biomaterials, 2016. **84**: 184-195.

72. N. Annabi, *et al.*, *Controlling the porosity and microarchitecture of hydrogels for tissue engineering.* Tissue Engineering Part B: Reviews, 2010. **16**(4): 371-383.

73. Y. Xu, *et al.*, *Porous hydrogel encapsulated photonic barcodes for multiplex microRNA quantification.* Advanced Functional Materials, 2018. **28**(1): 1704458.

74. A. Borisova, *et al.*, *A sustainable freeze-drying route to porous polysaccharides with tailored hierarchical meso- and macroporosity.* Macromolecular Rapid Communications, 2015. **36**(8): 774-779.

75. W. Zhou, *et al.*, *Tuning the mechanical properties of poly (ethylene glycol) microgel-based scaffolds to increase 3D schwann cell proliferation.* Macromolecular bioscience, 2016. **16**(4): 535-544.

76. L.R. Nih, *et al.*, *Injection of microporous annealing particle (MAP) hydrogels in the stroke cavity reduces gliosis and inflammation and promotes NPC migration to the lesion.* Advanced Materials, 2017. **29**(32): 1606471.

77. B.D. Fairbanks, *et al.*, *A versatile synthetic extracellular matrix mimic via thiol-norbornene photopolymerization.* Advanced Materials, 2009. **21**(48): 5005-5010.

78. A.D. Shubin, *et al.*, *Development of poly (ethylene glycol) hydrogels for salivary gland tissue engineering applications.* Tissue Engineering Part A, 2015. **21**(11-12): 1733-1751.

79. F. Jivan, *et al.*, *Sequential thiol-ene and tetrazine click reactions for the polymerization and functionalization of hydrogel microparticles.* Biomacromolecules, 2016. **17**(11): 3516-3523.

80. A.S. Qayyum, *et al.*, *Design of electrohydrodynamic sprayed polyethylene glycol hydrogel microspheres for cell encapsulation.* Biofabrication, 2017. **9**(2): 025019.

81. P.B. Welzel, *et al.*, *Cryogel micromechanics unraveled by atomic force microscopy-based nanoindentation.* Advanced Healthcare Materials, 2014. **3**(11): 1849-1853.

82. S. Dupont, *et al.*, *Role of YAP/TAZ in mechanotransduction.* Nature, 2011. **474**(7350): 179-183.

83. C.M. Magin, D.L. Alge, and K.S. Anseth, *Bio-inspired 3D microenvironments: a new dimension in tissue engineering.* Biomedical Materials, 2016. **11**(2): 022001.

84. J.D. McCall and K.S. Anseth, *Thiol–ene photopolymerizations provide a facile method to encapsulate proteins and maintain their bioactivity.* Biomacromolecules, 2012. **13**(8): 2410-2417.

85. P. Worthington, D.J. Pochan, and S.A. Langhans, *Peptide hydrogels-versatile matrices for 3D cell culture in cancer medicine.* Frontiers in Oncology, 2015. **5**: 92.

86. D. Thomas, T. O'Brien, and A. Pandit, *Toward customized extracellular niche engineering: progress in cell-entrapment technologies.* Advanced Materials, 2018. **30**(1): 1703948.

87. Y. Li, Y. Xiao, and C. Liu, *The horizon of materiobiology: a perspective on material-guided cell behaviors and tissue engineering.* Chemical Reviews, 2017. **117**(5): 4376-4421.

88. S.K. Seidlits, *et al.*, *The effects of hyaluronic acid hydrogels with tunable mechanical properties on neural progenitor cell differentiation.* Biomaterials, 2010. **31**(14): 3930-3940.

89. A.J. Engler, *et al.*, *Matrix elasticity directs stem cell lineage specification.* Cell, 2006. **126**(4): 677-689.

90. J.H. Wen, *et al.*, *Interplay of matrix stiffness and protein tethering in stem cell differentiation.* Nature Materials, 2014. **13**(10): 979-987.

91. C. Yang, *et al.*, *Mechanical memory and dosing influence stem cell fate.* Nature Materials, 2014. **13**(6): 645-652.

92. W.J. Hadden, *et al.*, *Stem cell migration and mechanotransduction on linear stiffness gradient hydrogels.* Proceedings of the National Academy of Sciences, 2017. **114**(22): 5647-5652.

93. C.M. Madl, S.C. Heilshorn, and H.M. Blau, *Bioengineering strategies to accelerate stem cell therapeutics.* Nature, 2018. **557**(7705): 335-342.

94. S. Lee, *et al.*, *Hydrogels with enhanced protein conjugation efficiency reveal stiffness-induced YAP localization in stem cells depends on biochemical cues.* Biomaterials, 2019. **202**: 26-34.

95. A.E. Stanton, X. Tong, and F. Yang, *Extracellular matrix type modulates mechanotransduction of stem cells.* Acta Biomaterialia, 2019. **96**: 310-320.

96. C.M. Kirschner and K.S. Anseth, *In situ control of cell substrate microtopographies using photolabile hydrogels.* Small, 2013. **9**(4): 578-584.

97. A. Thakur, *et al.*, *Injectable shear-thinning nanoengineered hydrogels for stem cell delivery.* Nanoscale, 2016. **8**(24): 12362-12372.

98. T.H. Qazi, *et al.*, *Biomaterials that promote cell-cell interactions enhance the paracrine function of MSCs.* Biomaterials, 2017. **140**: 103-114.

99. L. Riley, L. Schirmer, and T. Segura, *Granular hydrogels: emergent properties of jammed hydrogel microparticles and their applications in tissue repair and regeneration.* Current Opinion in Biotechnology, 2019. **60**: 1-8.

100. J.M. de Rutte, J. Koh, and D. Di Carlo, *Scalable high-throughput production of modular microgels for in situ assembly of microporous tissue scaffolds.* Advanced Functional Materials, 2019. **29**(35): 1900071.

101. S. Xin, O.M. Wyman, and D.L. Alge, *Assembly of PEG microgels into porous cell-instructive 3D scaffolds via thiol-ene click chemistry.* Advanced Healthcare Materials, 2018. **7**(11): 1800160.

102. N.F. Truong, *et al.*, *Microporous annealed particle hydrogel stiffness, void space size, and adhesion properties impact cell proliferation, cell spreading, and gene transfer.* Acta Biomaterialia, 2019. **94**: 160-172.

103. C.D. Reyes and A.J. García, *α2β1 integrin-specific collagen-mimetic surfaces supporting osteoblastic differentiation.* Journal of Biomedical Materials Research Part A, 2004. **69**(4): 591-600.

104. B.G. Keselowsky, D.M. Collard, and A.J. García, *Integrin binding specificity regulates biomaterial surface chemistry effects on cell differentiation.* Proceedings of the National Academy of Sciences, 2005. **102**(17): 5953-5957.

105. E. Koivunen, B. Wang, and E. Ruoslahti, *Isolation of a highly specific ligand for the alpha 5 beta 1 integrin from a phage display library.* The Journal of Cell Biology, 1994. **124**(3): 373-380.

106. O. Fromigué, *et al.*, *Peptide-based activation of alpha5 integrin for promoting osteogenesis.* Journal of cellular biochemistry, 2012. **113**(9): 3029-3038.

107. A.P. Mould, L. Burrows, and M.J. Humphries, *Identification of amino acid residues that form part of the ligand-binding pocket of integrin α5β1.* Journal of Biological Chemistry, 1998. **273**(40): 25664-25672.

108. Z. Saidak, *et al.*, *Wnt/β-catenin signaling mediates osteoblast differentiation triggered by peptide-induced α5β1 integrin priming in mesenchymal skeletal cells.* Journal of Biological Chemistry, 2015. **290**(11): 6903-6912.

109. N.R. Gandavarapu, D.L. Alge, and K.S. Anseth, *Osteogenic differentiation of human mesenchymal stem cells on α5 integrin binding peptide hydrogels is dependent on substrate elasticity.* Biomaterials Science, 2014. **2**(3): 352-361.

110. S. Xin, et al., *Clickable PEG hydrogel microspheres as building blocks for 3D bioprinting.* Biomaterials Science, 2019. **7**(3): 1179-1187.

111. J. Patterson and J.A. Hubbell, *Enhanced proteolytic degradation of molecularly engineered PEG hydrogels in response to MMP-1 and MMP-2.* Biomaterials, 2010. **31**(30): 7836-7845.

112. B. Trappmann, *et al.*, *Matrix degradability controls multicellularity of 3D cell migration.* Nature Communications, 2017. **8**(1): 371.

113. S. Zeitouni, *et al.*, *Human mesenchymal stem cell-derived matrices for enhanced osteoregeneration.* Science Translational Medicine, 2012. **4**(132): 132ra55.

114. C.M. McLeod and R.L. Mauck, *High fidelity visualization of cell-to-cell variation and temporal dynamics in nascent extracellular matrix formation.* Scientific Reports, 2016. **6**: 38852.

115. B.H. Clough, M.R. McCarley, and C.A. Gregory, *A simple critical-sized femoral defect model in mice.* JoVE (Journal of Visualized Experiments), 2015. **97**: e52368.

116. H. Nagase and G.B. Fields, *Human matrix metalloproteinase specificity studies using collagen sequence-based synthetic peptides.* Peptide Science, 1996. **40**(4): 399-416.

117. M.M. Martino, *et al.*, *Controlling integrin specificity and stem cell differentiation in 2D and 3D environments through regulation of fibronectin domain stability.* Biomaterials, 2009. **30**(6): 1089-1097.

118. U. Krause, *et al.*, *Pharmaceutical modulation of canonical Wnt signaling in multipotent stromal cells for improved osteoinductive therapy.* Proceedings of the National Academy of Sciences, 2010. **107**(9): 4147-4152.

119. U. Krause, A. Seckinger, and C.A. Gregory, *Assays of osteogenic differentiation by cultured human mesenchymal stem cells*, in *Mesenchymal Stem Cell Assays and Applications*. 2011, Springer. p. 215-230.

120. J. Koh, *et al.*, *Enhanced in vivo delivery of stem cells using microporous annealed particle scaffolds.* Small, 2019. **15**(39): 1903147.

121. M. Guvendiren and J.A. Burdick, *The control of stem cell morphology and differentiation by hydrogel surface wrinkles.* Biomaterials, 2010. **31**(25): 6511-6518.

122. C. Loebel, R.L. Mauck, and J.A. Burdick, *Local nascent protein deposition and remodelling guide mesenchymal stromal cell mechanosensing and fate in three-dimensional hydrogels.* Nature Materials, 2019. **18**: 883-891.

123. M.L. Decaris and J.K. Leach, *Design of experiments approach to engineer cell-secreted matrices for directing osteogenic differentiation.* Annals of Biomedical Engineering, 2011. **39**(4): 1174-1185.

124. Y. Kang, *et al.*, *Creation of bony microenvironment with CaP and cell-derived ECM to enhance human bone-marrow MSC behavior and delivery of BMP-2.* Biomaterials, 2011. **32**(26): 6119-6130.

125. S.A. Ferreira, *et al.*, *Neighboring cells override 3D hydrogel matrix cues to drive human MSC quiescence.* Biomaterials, 2018. **176**: 13-23.

126. X. Tong and F. Yang, *Sliding hydrogels with mobile molecular ligands and crosslinks as 3D stem cell niche.* Advanced Materials, 2016. **28**(33): 7257-7263.

127. E. Bassat, *et al.*, *The extracellular matrix protein agrin promotes heart regeneration in mice.* Nature, 2017. **547**(7662): 179-184.

128. Y. Dong, *et al.*, *Injectable and tunable gelatin hydrogels enhance stem cell retention and improve cutaneous wound healing.* Advanced Functional Materials, 2017. **27**(24): 1606619.

129. K.H. Hong, Y.M. Kim, and S.C. Song, *Fine-tunable and injectable 3D hydrogel for on-demand stem cell niche.* Advanced Science, 2019. **6**(17): 1900597.

130. S.L. Vega, *et al.*, *Combinatorial hydrogels with biochemical gradients for screening 3D cellular microenvironments.* Nature Communications, 2018. **9**(1): 614.

131. A.K. Gaharwar, *et al.*, *3D biomaterial microarrays for regenerative medicine: current state-of-the-art, emerging directions and future trends.* Advanced Materials, 2016. **28**(4): 771-781.

132. F. Gao, *et al.*, *Direct 3D printing of high strength biohybrid gradient hydrogel scaffolds for efficient repair of osteochondral defect.* Advanced Functional Materials, 2018. **28**(13): 1706644.

133. L. Ouyang, *et al.*, *A generalizable strategy for the 3D bioprinting of hydrogels from nonviscous photo-crosslinkable inks.* Advanced Materials, 2017. **29**(8): 1604983.

134. L. Moroni, *et al.*, *Biofabrication strategies for 3D in vitro models and regenerative medicine.* Nature Reviews Materials, 2018. **3**(5): 21-37.

135. N.J. Darling, *et al.*, *Injectable and spatially patterned microporous annealed particle (MAP) hydrogels for tissue repair applications.* Advanced Science, 2018. **5**(11): 1801046.

136. J. Radhakrishnan, *et al.*, *Gradient nano-engineered in situ forming composite hydrogel for osteochondral regeneration.* Biomaterials, 2018. **162**: 82-98.

137. P. Li, *et al.*, *Morphogen gradient reconstitution reveals Hedgehog pathway design principles.* Science, 2018. **360**(6388): 543-548.

138. D.M. Headen, J.R. García, and A.J. García, *Parallel droplet microfluidics for high throughput cell encapsulation and synthetic microgel generation.* Microsystems & Nanoengineering, 2018. **4**: 17076.

139. F. Lin, *et al.*, *Generation of dynamic temporal and spatial concentration gradients using microfluidic devices.* Lab on a Chip, 2004. **4**(3): 164-167.

140. J.A. Burdick, A. Khademhosseini, and R. Langer, *Fabrication of gradient hydrogels using a microfluidics/photopolymerization process.* Langmuir, 2004. **20**(13): 5153-5156.

141. O. Jeon, *et al.*, *Biochemical and physical signal gradients in hydrogels to control stem cell behavior.* Advanced Materials, 2013. **25**(44): 6366-6372.

142. S. Pedron, E. Becka, and B.A. Harley, *Spatially gradated hydrogel platform as a 3D engineered tumor microenvironment.* Advanced Materials, 2015. **27**(9): 1567-1572.

143. J. Dai, *et al.*, *Determination of antibiotic EC50 using a zero-flow microfluidic chip based growth phenotype assay.* Biotechnology Journal, 2015. **10**(11): 1783-1791.

144. J. Dai, *et al.*, *A large-scale on-chip droplet incubation chamber enables equal microbial culture time.* RSC Advances, 2016. **6**(25): 20516-20519.

145. M.A. Unger, *et al.*, *Monolithic microfabricated valves and pumps by multilayer soft lithography.* Science, 2000. **288**(5463): 113-116.

146. J. Kim, *et al.*, *A programmable microfluidic cell array for combinatorial drug screening.* Lab on a Chip, 2012. **12**(10): 1813-1822.

147. H. Song, J.D. Tice, and R.F. Ismagilov, *A microfluidic system for controlling reaction networks in time.* Angewandte Chemie International Edition, 2003. **42**(7): 768-772.

148. B. Xia, K. Krutkramelis, and J. Oakey, *Oxygen-purged microfluidic device to enhance cell viability in photopolymerized PEG hydrogel microparticles.* Biomacromolecules, 2016. **17**(7): 2459-2465.

149. C.E. Hoyle and C.N. Bowman, *Thiol-ene click chemistry.* Angewandte Chemie International Edition, 2010. **49**(9): 1540-1573.

150. X.H. Qin, *et al.*, *Near-infrared light-sensitive polyvinyl alcohol hydrogel photoresist for spatiotemporal control of cell-instructive 3D microenvironments.* Advanced Materials, 2018. **30**(10): 1705564.

151. H. Du, *et al.*, *Fabrication of hexagonal prismatic granular hydrogel sheets.* Langmuir, 2018. **34**(11): 3459-3466.

152. C.H. Choi, *et al.*, *One-step generation of cell-laden microgels using double emulsion drops with a sacrificial ultra-thin oil shell.* Lab on a Chip, 2016. **16**(9): 1549-1555.

153. O. Wagner, *et al.*, *Biocompatible fluorinated polyglycerols for droplet microfluidics as an alternative to PEG-based copolymer surfactants.* Lab on a Chip, 2016. **16**(1): 65-69.

154. Y.S. Zhang, *et al.*, *3D bioprinting for tissue and organ fabrication.* Annals of Biomedical Engineering, 2017. **45**(1): 148-163.

155. N.J. Castro and D.W. Hutmacher, *Designification of neurotechnological devices through 3D printed functional materials.* Advanced Functional Materials, 2018. **28**(12): 1703905.

156. B.A. Aguado, *et al.*, *Engineering precision biomaterials for personalized medicine.* Science Translational Medicine, 2018. **10**(424): eaam8645.

157. A.K. Miri, *et al.*, *Microfluidics-enabled multimaterial maskless stereolithographic bioprinting.* Advanced Materials, 2018. **30**(27): 1800242.

158. S.F.S. Shirazi, *et al.*, *A review on powder-based additive manufacturing for tissue engineering: selective laser sintering and inkjet 3D printing.* Science and Technology of Advanced Materials, 2015. **16**(3): 033502.

159. S.V. Murphy and A. Atala, *3D bioprinting of tissues and organs.* Nature Biotechnology, 2014. **32**(8): 773-785.

160. S. Bertlein, *et al.*, *Thio-ene clickable gelatin: a platform bioink for multiple 3D biofabrication technologies.* Advanced Materials, 2017. **29**(44): 1703404.

161. D. Chimene, *et al.*, *Nanoengineered ionic-covalent entanglement (NICE) bioinks for 3D bioprinting.* ACS Applied Materials & Interfaces, 2018. **10**(12): 9957-9968.

162. J. Jang, *et al.*, *Biomaterials-based 3D cell printing for next-generation therapeutics and diagnostics.* Biomaterials, 2018. **156**: 88-106.

163. P.S. Gungor-Ozkerim, *et al.*, *Bioinks for 3D bioprinting: an overview.* Biomaterials Science, 2018. **6**(5): 915-946.

164. J.K. Placone and A.J. Engler, *Recent advances in extrusion-based 3D printing for biomedical applications.* Advanced Healthcare Materials, 2018. **7**(8): 1701161.

165. X. Zhai, *et al.*, *3D-bioprinted osteoblast-laden nanocomposite hydrogel constructs with induced microenvironments promote cell viability, differentiation, and osteogenesis both in vitro and in vivo.* Advanced Science, 2018. **5**(3): 1700550.

166. L.L. Wang, *et al.*, *Three-dimensional extrusion bioprinting of single- and double-network hydrogels containing dynamic covalent crosslinks.* Journal of Biomedical Materials Research Part A, 2018. **106**(4): 865-875.

167. S.A. Wilson, *et al.*, *Shear-thinning and thermo-reversible nanoengineered inks for 3D bioprinting.* ACS Applied Materials & Interfaces, 2017. **9**(50): 43449-43458.

168. T.E. Brown and K.S. Anseth, *Spatiotemporal hydrogel biomaterials for regenerative medicine.* Chemical Society Reviews, 2017. **46**(21): 6532-6552.

169. C.M. Madl and S.C. Heilshorn, *Bioorthogonal strategies for engineering extracellular matrices.* Advanced Functional Materials, 2018. **28**(11): 1706046.

170. X. Kuang, *et al.*, *3D printing of highly stretchable, shape-memory, and self-healing elastomer toward novel 4D printing.* ACS Applied Materials & Interfaces, 2018. **10**(8): 7381-7388.

171. J. Yin, et al., *3D bioprinting of low-concentration cell-laden gelatin methacrylate (GelMA) bioinks with a two-step cross-linking strategy.* ACS Applied Materials & Interfaces, 2018. **10**(8): 6849-6857.

172. J. Lou, *et al.*, *Dynamic hyaluronan hydrogels with temporally modulated high injectability and stability using a biocompatible catalyst.* Advanced Materials, 2018. **30**(22): 1705215.

173. T.J. Hinton, *et al.*, *Three-dimensional printing of complex biological structures by freeform reversible embedding of suspended hydrogels.* Science Advances, 2015. **1**(9): e1500758.

174. C.B. Highley, *et al.*, *Jammed microgel inks for 3D printing applications.* Advanced Science, 2019. **6**(1): 1801076.

175. C.J. Young, L.A. Poole-Warren, and P.J. Martens, *Combining submerged electrospray and UV photopolymerization for production of synthetic hydrogel microspheres for cell encapsulation.* Biotechnology and Bioengineering, 2012. **109**(6): 1561-1570.

176. L.A. Sawicki and A.M. Kloxin, *Design of thiol-ene photoclick hydrogels using facile techniques for cell culture applications.* Biomaterials Science, 2014. **2**(11): 1612-1626.

177. W. Liu, *et al.*, *Coaxial extrusion bioprinting of 3D microfibrous constructs with cell-favorable gelatin methacryloyl microenvironments.* Biofabrication, 2018. **10**(2): 024102.

178. J. Yang, *et al.*, *Cell-laden hydrogels for osteochondral and cartilage tissue engineering.* Acta Biomaterialia, 2017. **57**: 1-25.

179. T. Woodfield, *et al.*, *Polymer scaffolds fabricated with pore-size gradients as a model for studying the zonal organization within tissue-engineered cartilage constructs.* Tissue Engineering, 2005. **11**(9-10): 1297-1311.